2012 Joint Research Target (JRT)
Final Report
Prepared and Submitted by 2012 JRT Team*
September 30, 2012

JRT Description:

Conduct experiments and analysis on major fusion facilities leading toward improved understanding of core transport and enhanced capability to predict core temperature and density profiles. In FY 2012, FES will assess the level of agreement between predictions from theoretical and computational transport models and the available experimental measurements of core profiles, fluxes and fluctuations. The research is expected to exploit the diagnostic capabilities of the facilities (Alcator C-Mod, DIII-D, NSTX) along with their abilities to run in both unique and overlapping regimes. The work will emphasize simultaneous comparison of model predictions with experimental energy, particle and impurity transport levels and fluctuations in various regimes, including those regimes with significant excitation of electron modes. Along with new experiments, work will include analysis of relevant previously collected data and collaboration among the research teams. The results achieved will be used to improve confidence in transport models used for extrapolations to planned ITER operation.

Quarter 4 Milestone:

All experiments and analysis completed. Final report prepared and submitted, outlining experimental observations, initial comparisons with code predictions and recommendations for further work..

Completion of 4th Quarter Milestone

With submission of this report, the milestone has been successfully completed. The report summarizes:

[1] Diagnostic upgrades and analysis improvements that support the JRT
[2] Descriptions of new experiments and a brief summary of our findings
[3] New analysis of previous experiments
[4] Plans for further data analysis and recommendations for further work
[5] Scientific publications that are derived from or contributed directly to the JRT

The report is organized as follows:

Section 1: Describes inter-machine comparisons that were facilitated by the JRT focus. Similarities and differences found on the different facilities are outlined and plans for additional analysis of data and supporting simulations are described.

Section 2: Reviews diagnostic development, experiments and results from C-Mod. C-Mod dedicated 13.1 run days to the JRT divided among 10 experimental proposals. These were organized into three general thrust areas that represent distinct experimental approaches to realizing the regimes called for in the JRT description. Initial comparisons with linear and nonlinear simulation have been carried out for these experiments and plans for an extensive campaign of analysis has been outlined.

Section 3: Reviews results from DIII-D including new experiments, detailed comparisons of simulations to previously collected data and connections between the new work and past research. Four experimental days were dedicated to the JRT in 2012. These included studies of L-modes, H-modes and QH-modes.

Section 4: Summarizes new analysis of data collected before the NSTX shutdown. The work focuses on the roles of low and high-k turbulence; collisionality scans and impurity particle transport.

In all cases, analysis is ongoing and will continue to produce new results over the next year or two.

*2012 JRT Team

C-Mod: Mark Chilenski, Luis Delgado-Aparicio, Paul Ennever, Chi Gao, Darin Ernst, Catherine Fiore, Nathan Howard, Martin Greenwald (lead), David Mikkelsen, Miklos Porkolab, Matt, Reinke, John Rice, Choongki Sung, Anne White

DIII-D: Keith Burrell (lead), Edward Doyle , Chris Holland, Jon Kinsey, Alessandro Marinoni, , George McKee, Terry Rhodes, Sterling Smith, Ron Prater, Craig Petty, Lothar Schmitz, Phil Snyder, Gary Staebler, Ron Waltz, Zheng Yan, and Lei Zeng.

NSTX: D. Clayton, W. Guttenfelder, S. Kaye (lead), S. Kubota, F. Poli, Y. Ren, F. Scotti, D. Smith, V. Soukhanovskii, K. Tritz and W. Wang

Section 1: Inter-machine Comparison/Collaboration

As experiments and analysis proceeded, effort was focused on larger thematic issues. These issues are particularly illuminated in similarities and differences in results between facilities. Initial comparisons of results between machines is described in this section – we anticipate substantial additional analysis and a number of jointly authored papers will follow. Topics covered include:

[1] Transport shortfall – especially at larger r/a
[2] L-mode Ip scan
[3] L-mode Power scan, electron vs ion dominated plasmas
[4] I-mode/I-mode/QH mode comparisons
[5] H-mode Collisionality scan

These topics and progress on data analysis, collaboration plans, and publications are discussed below.

1.A Inter-machine Topics [1] and [2] are addressed using old experimental/modeling results from C-Mod [1.1] and new experiments/modeling results from a DIII-D experiment [D3DMP #2012-71-05]. It is well known that confinement improves globally as plasma current is increased. Investigating how well the gyrokinetic model reproduces this overall trend has been explored with engineering I_P scans at both C-Mod and DIII-D. These L-mode plasmas also provide excellent target discharges for studying the transport shortfall. The so-called transport shortfall at larger r/a has been robustly identified in DIII-D experiments. The shortfall manifests in L-mode plasmas, where GYRO and GEM have under-predicted the transport compared to experimental power balance results [1.2-4].

q_95 C-Mod	q_95 DIII-D	Ip DIII-D
3.15		
3.7	3.9	1.4 MA
5.65	5.5	1 MA
	7.3	0.75 MA

Table 1: Plasma currents used in the DIII-D JRT2012 Shortfall Experiment selected to match two q95 values from the C-Mod Ip scan experiments [Howard POP 2012].

Investigation of the transport shortfall was the subject of a new JRT2012 experiment at DIII-D, that took place on August 2nd 2012. The DIII-D JRT 2012 experiment (led by Terry Rhodes, UCLA) explored the transport shortfall in simple L-mode plasmas, with and without sawteeth. See the DIII-D Section of this report for more details of this experiment.

One goal of the experiment was to test a prediction that the transport shortfall should become larger at higher q, and should also extend deeper into the core [1.5]. The first half-day run plan called for an engineering q-scan, in conditions that very closely match the plasma shape and q95 values from past C-Mod JRT 2012 experiments [1.1] that investigate the scaling of impurity particle and energy confinement with plasma current.

For the comparison to C-Mod we concentrated on the sawtoothing period of these discharges since the C-Mod results were from sawtoothing discharges. This new experiment at

DIII-D will allow the C-Mod and DIII-D teams to study the shortfall in detail for the first time using a targeted data set from two tokamaks. Table 1 lists the values of Ip and q that provide a matched data set between DIII-D and C-Mod. Figure 1.1 shows the plasma shape chosen for the DIII-D experiment to closely match the C-Mod shape.
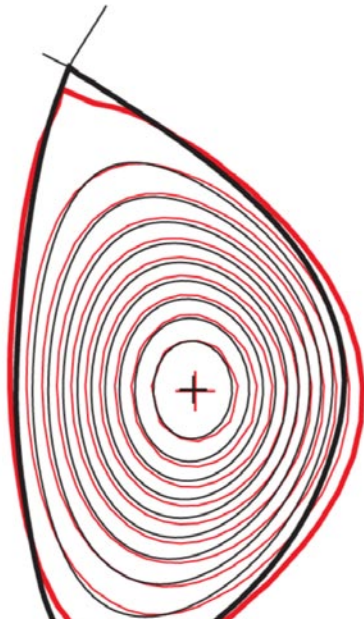

*Figure 1.1 Comparing plasma shapes: C-Mod (red, shot 1101014006) and DIII-D target for JRT 2012 Shortfall Experiment (**black**, shot 144350)*
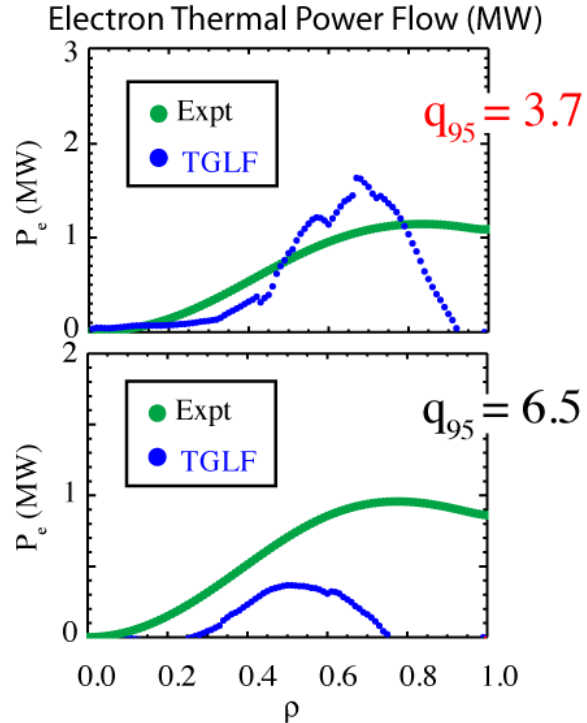
Figure 1.2 Comparing electron thermal power flows from the Joint Collaborative Experiment and TGLF predictions. The shortfall is begins to occur for $\rho\sim0.8$ for $q=3.7$ and is significantly worse at $q=6.5$.

During the experiment Jon Kinsey reported that the TGLF transport under-prediction was more dominant in the electron channel compared to the ion channel. This was very different from the higher density reference shot case and quite interesting. This seemed important enough to prompt us to obtain data at a higher density for the three target q_{95} values. Overall, this gave us scans in q_{95}, density, and rotation (we had an NBI power ramp later in each plasma discharge). The transport underprediction was indeed replicated in this experiment, as can be seen in Fig. 1.2.

Preliminary analysis of the C-Mod experiments and comparison with nonlinear gyrokinetics found a shortfall only in the electron channel and only in relatively low temperature L-modes. In higher temperature, lower collisionality I-modes, the

4

simulations matched the experiments in both channels [1.6]. This results supports the hypothesis that the controlling parameter for the short fall is the gyro-Bohm normalized power – which is higher in the edge of L-mode.

Analysis Plans for Topic [1] and [2]: Profile and fluctuation data analysis from the DIII-D Shortfall Experiment and Ip scan is in progress. Several papers/topics and first authors have been tentatively identified. These collaborative papers will include:

1. Physics of the Ip scan (fluctuation data, power balance, lin. and nonlinear GYRO analysis, TGLF analysis (Rhodes)

2. Physics of the shortfall (scaling with q95, comparison between TGLF and experiment) (Kinsey)

3. Dimensionless q-scan data set, explore shortfall with GYRO and TGLF. (White)

4. Ip scan, comparing experimental trends with global, nonlinear GYRO results across C-Mod and DIII-D (Howard)

1.B Inter-machine Topic [3] is addressed by combining analysis of older experiments at DIII-D [1.7] with the new JRT experiment MP689 at C-Mod. In both tokamaks, a power scan is used to increase electron temperature and temperature gradient and destabilize the TEM. At DIII-D, ECH into a baseline beam-heated plasma was used for the power scan and changes in transport and electron temperature fluctuation levels were monitored. The 2.5 MW of ECH in addition to 2.5 MW of beam power provides an increase in electron temperature at fixed density and roughly constant ion temperature. Comparison with linear and nonlinear GYRO results suggested that the increased electron heat transport and increased electron temperature fluctuations were consistent with stronger TEM drive in the ECH plasmas.

At C-Mod, ICRF is applied to low-density L-mode plasmas, scanning power from 1.0 MW to 4.0 MW. In these cases, the minority heating scenario dominantly heats the electrons, providing an increase in electron temperature at fixed density and roughly constant ion temperature. Preliminary linear and nonlinear GYRO analysis indicates that the C-Mod plasmas show the same response to electron heating as DIII-D: increase in electron heat transport due to increased importance of TEM turbulence. Initial results from the new CECE diagnostic at C-Mod also show increased electron temperature fluctuations, which is consistent with stronger TEM drive in the higher temperature RF plasmas. A C-Mod validation paper on the RF power scan plasmas is planned [1.1], which will provide a good one-to-one connection with the older DIII-D [1.2] results.

1.C Inter-machine Topic [4] is being addressed with experiments and modeling work on I-mode at C-Mod and QH-mode at DIII-D.

One robust result observed when comparing L-mode plasmas to I-mode plasmas, or L-mode plasmas to QH-mode plasmas, is the substantial reduction of *core* turbulence and transport across the transition.

At DIII-D, [1.8-10] turbulence measurements have shown a reduction of core density fluctuations across the L-QH transition. This reduction is observed across low and intermediate wavenumbers with a variety of fluctuation diagnostics. There is a reduction of core electron temperature fluctuations across L-QH transition (low k). This change in

5

turbulence is consistent with increased ExB shear, with growth rates (e.g. ITG) similar during L-mode and I-mode.

Similarly, turbulence measurements at C-Mod across L-I transitions show that there is a reduction of core density fluctuations across L-I transition. This is most clearly observed in the low k density fluctuation data measured with reflectometry over the core plasma region. as shown in Figure 1.3a. Fluctuations are reduced up to 30% in I-mode compared
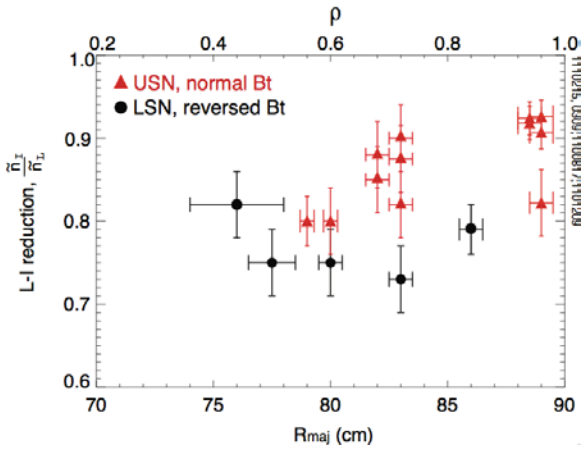

Figure 1.3a Partial profile of relative change in broadband (20 kHz < f< 800 kHz))core density fluctuations in I-mode compared to L-mode, as measured with the O-mode multi-channel baseband fluctuation reflectometer at C-Mod
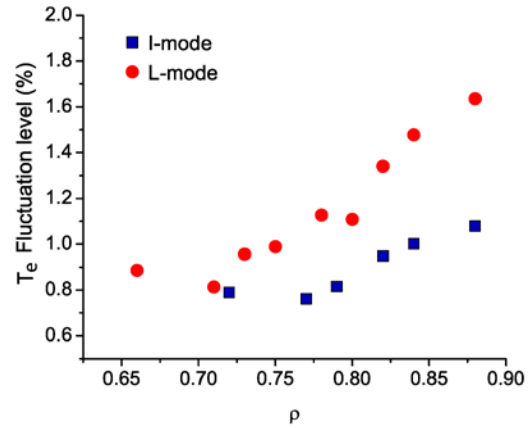
Figure 1.3b Partial profile of normalized electron temperature fluctuations in L-mode (red) and I-mode (black) plasmas showing the reduction during I-mode.

to L-mode deeper in the core, with smaller reductions observed nearer the edge. The figure only shows changes in broadband fluctuation levels (integrated over the entire frequency range 20 kHz < f < 800 kHz). This means the complex changes in *edge/pedestal* fluctuations associated with the far L-modeI-mode edge (rho > 0.95) where the WCM turbulent feature appears are not represented this analysis [see 1.11, 1.12 for more information on the changes in edge turbulence across the L-I transition].

In the outer core plasma, new measurements from C-Mod have shown a reduction of core electron temperature fluctuations across L-I transition (low k), as measured with the new Correlation ECE diagnostic at C-Mod, Figure 1.3b. Note that a strong reduction of temperature fluctuations in QH-mode plasmas was reported at DIII-D [1.8]. Interestingly, the results from C-Mod L-I transitions differ markedly from the DIII-D QH-mode results in terms of how ExB shear changes with respect to changes in the linear growth rates of dirft wave instabilities. At C-Mod, the change in turbulence is consistent with reduced growth rates (ITG dominant in both L-mode and I-mode) in the presence of similar ExB shearing rates. Analysis is in progress to determine what role ExB shear suppression plays in reducing core turbulence in I-Mode. Preliminary power balance results from these I-modes show that electron heat transport drops, but ion heat transport stays the

same, indicating the important role of dominantly ITG-turbulence in driving electron heat transport in L-mode.

A second result from the QH-mode and I-mode experiments is obtained by scanning temperature with ECH and RF heating at DIII-D and C-Mod, respectively.

At DIII-D. QH-mode power balance results in higher density plasmas has shown that there is a clear separation of ion and electron heat transport in higher density steady QH plasmas. Furthermore, it is possible to alter the relative importance of ion/electron transport channels with ECH in steady QH-mode plasmas. In addition, there is a significant change of density fluctuations observed with ECH. An initial 2010 experiment aimed to measure the response of turbulence and transport to the addition of ECH heating into a baseline NBI-heated QH-mode discharge. A variety of different timeslices were analyzed from these discharges, in order to examine variations in paramters such as $T_e(0)/T_i(0)$. One set of comparisons, reported in [1.13] focused upon late-comparisons when both the NBI-only and NBI+ECH cases had settled in relatively static conditions persisting for hundreds of ms. A comparison of the measured density, temperature, and rotation profiles from these discharges is seen in Fig. 1.4.

As seen in Fig. 1.4, the application of ECH heating significantly increase thermal diffusivities in both the ion and electron channels, with noticible reductions in on-axis density peaking and flattening of the ion temperature and toroidal rotation profiles. The
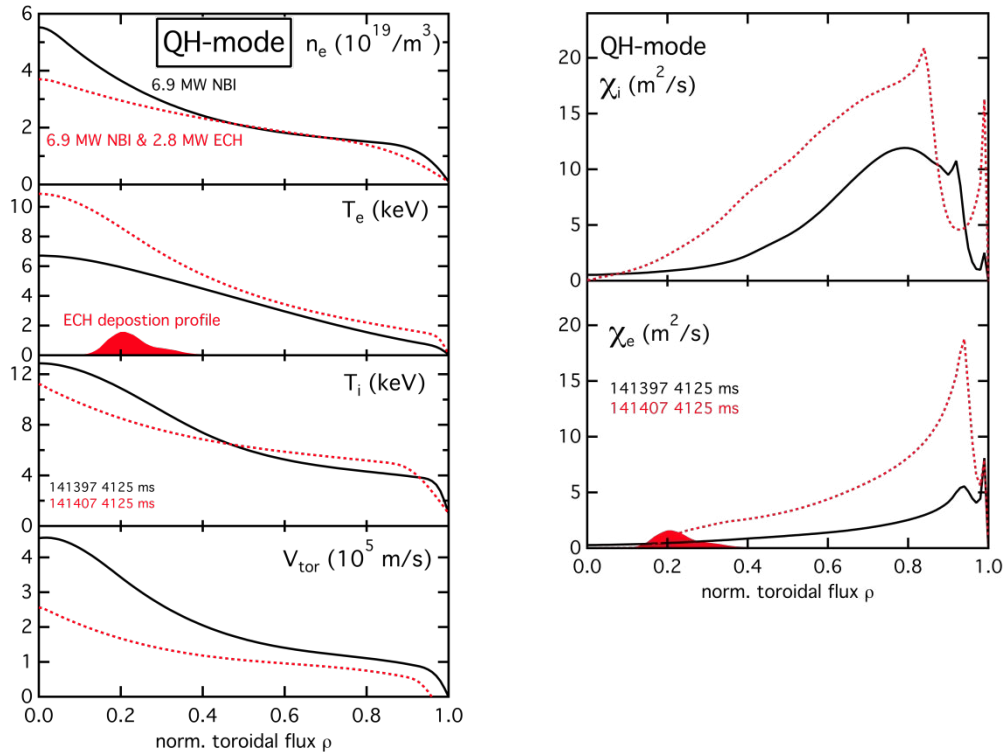

Fig. 1.4: (left) Changes in n_e, T_e, T_i, and V_{tor} with and without 2.8 MW of ECH heating deposited at rho = 0.2 (right) Changes in ion and electron thermal diffusivities.

ECH heating also raised on-axs T_e significantly such that $T_e(0)/T_i(0) \sim 1$. However, only small increases in T_e were observed at larger radii, and were accompanied by similar increases in T_i, such that T_e/T_i remained relatively constant. These findings helped motivate a 2012 experiment using QH-modes with lower density and ECH depostion at larger radii, focused on changing T_e/T_i at those outer radii; those results are discussed below. For these times, only BES measurements were obtained, finding very low density fluctuation amplitudes near the sensitivity threshold of the device.
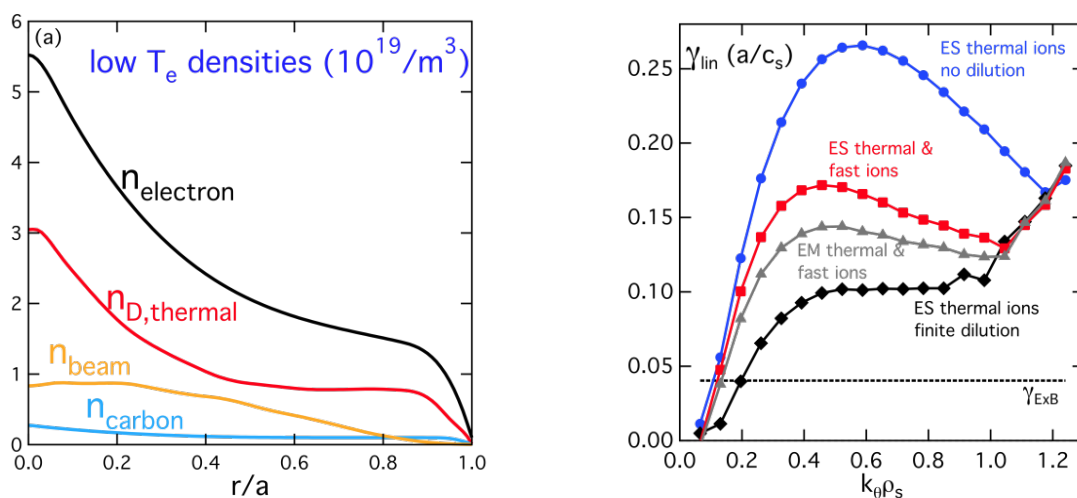

Fig. 1.5 (left) Comparison of electron, thermal D, thermal C, and fast beam ion D density profiles for shot 141397. (right) Comparisons of linear growth rate calculations at rho=0.6 for shot 141397 with different treatments of fast ion and electromagnetic effects.

Linear and nonlinear gyrokinetic analyses of these discharges found that the significant fast beam ion fraction present in these discharges ($n_{fast}/n_e \sim 0.25$ at rho=0.6; see Fig. 1.5) significantly impacted the turbulence. In particular, inclusion of the fast ion effects as purely dilutionary ($\delta n_{fast}/n_{fast} = 0$) was strongly stabilizing relative to the case where they were neglected, but a (perhaps) more realistic treatment of the fast ions as a separate ion species with $T_{fast} \sim 30\text{-}35$ keV did not indicate quite as strong a stabilizing effect (Fig. 1.5). These results were borne out by nonlinear GYRO simulations, which assessed these different treatments on transport predictions. It was found that when the fast ions were included as a separate gyrokinetic species, a clear reduction in transport was obtained, with additional reductions coming from inclusion of finite perpendicular magnetic fluctuations (Fig. 1.6). Interestingly, the magnetic fluctuations were found to increase transport when the fast ion population was neglected. These results were all obtained for local GYRO simulations; to date numerically stable and converged electromagnetic global simulations of these plasmas have not been achieved. However, electrostatic global simulations of these and other H-mode plasmas with similar rho-star values indicate that an additional factor of 2 reduction in transport may result from profile shearing and other nonlocal effects, which would bring the GYRO predictions in line with the power balance results. These results have been published in [1.14].

Motivated by the fast ion effects observed in the modeling of the 2010 QH-mode plasmas, a second QH-mode experiment was conducted in 2012, which aimed to measure the response to ECH heating in plasmas with line averaged densities of ~3-4e13 cm^{-2}, which would have correspondingly lower fast ion fractions. DIII-D discharge 131920 was used as the target condition; NUBEAM modeling of this discharge predicted fast ion fractions of < 10% at rho=0.6 in this shot [1.14].
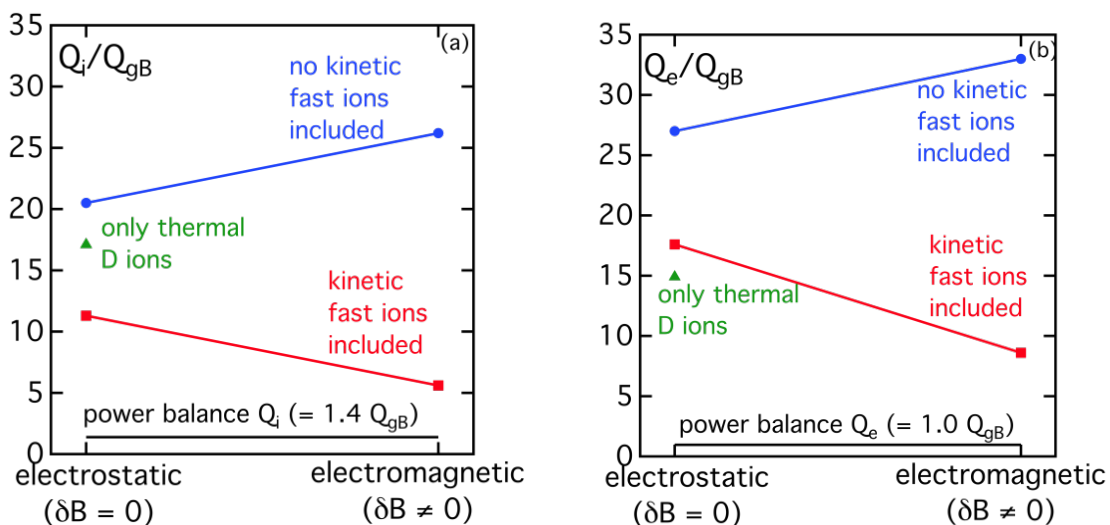

Fig. 1.6. Scaling of local GYRO predictions for (left) ion energy flux Q_i and (right) electron energy flux Q_e, normalized to the gyroBohm value $Q_{gB} = n_eT_ec_s(\rho_s/a)^2$, as a function of fast ion treatment and electromagnetic fluctuation inclusion. Note that assuming adiabatic electrons, or that the fast ions are purely dilutionary ($\delta n_{fast}/n_{fast} = 0$), yields completely shear-suppressed turbulence.

A comparison of the measured profiles for the 131920 reference shot, as well as the measured profiles of the 2012 without (149144, 149150) and with (149157) ECH heating are shown in Fig. 1.7, along with the power balance thermal diffusivities. It is interesting to note the for shot 149144, the collisional exchange term is strong enough to overwhelm the beam heating of the ions (which is ~2 as large as the beam heating of the electrons) to yield a negative χ_i over the outer 25% of the plasma, and very high χ_e values. A similar balance is found for 149150, but smaller in magnitude due to the lower density of 149150 relative to 149144. In shot 149157, the application of ECH heating strongly increases χ_i across the plasma domain, but leads to small decreases in χ_e beyond rho=0.6, relative to shots 149144 and 149150. It should be noted that there was a 25% reduction in line-averaged n_e when the ECH was applied in this experiment, while line-averaged n_e was approximately constant in the 2010 experiment.

In another set of related experiments at DIII-D, QH-mode power balance analysis of lower density plasmas with ECH have shown consistently that changes in transport are linked to a change of ITG/TEM stability. Interestingly, there is little to no change of density fluctuations observed with ECH, but temperature fluctuations increase significantly

Linear (TGLF) stability calculations carried out for the 2010 low density QH-mode experiment predict a transition from an ITG to a TEM-dominated regime for r/a<0.5 and from a mixed-mode regime to the TEM-dominated regime for r/a>0.5 as ECH is applied with deposition at r/a~0.2. Fig. 1.8b shows the linear growth rates of the electron and ion root vs. $k_\theta\rho_s$, for r/a =0.6. The TEM growth rate is clearly enhanced with ECH in particular at low $k_\theta\rho_s$. The sensitivity of the linear growth rate to experimental profiles has been investigated in detail and reported in a journal paper [1.10], together with comprehensive transport and fluctuation analysis. Figure 1.9 shows a mapping of the ITG/TEM boundary versus the normalized ion and electron temperature gradients R/L_{Te}, R/L_{Ti}, and versus T_e/T_i, for r/a=0.6, in shot 140407. The reference QH-mode plasma is very close to the ITG/TEM stability boundary.
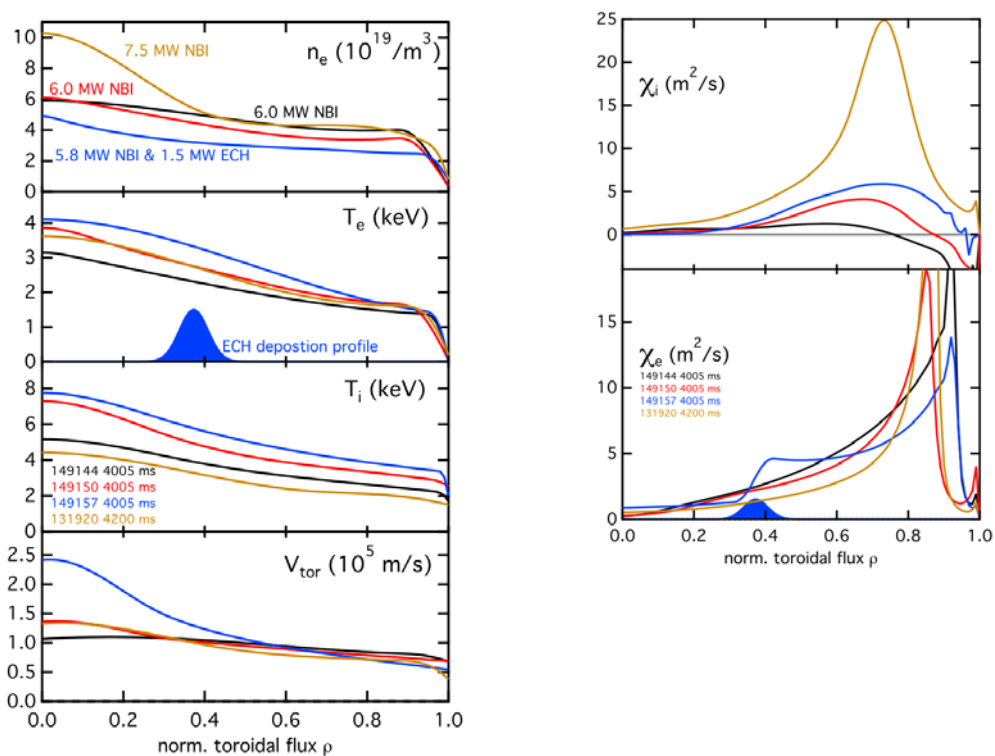

Fig. 1.7. (left) Changes in n_e, T_e, T_i, and V_{tor} with different mixes of NBI and ECH heating. (right) Changes in ion and electron thermal diffusivities.

As ECH is applied, the TEM boundary is crossed due to the increasing T_e/T_i ratio, and the ensuing reduction in R/L_{Ti} (due to increased ion thermal diffusivity as shown in Fig. 1.1 and discussed below). ExB shear outside of r/a=0.4 significantly affects only the growth rates of long poloidal wavelength modes($k_\theta\rho_s \leq 0.3$) but decreases with ECH due to the reduced radial gradient in toroidal rotation. Strong experimental evidence of the TEM transition and/or increased TEM turbulence level is provided by a large increase in the measured electron temperature fluctuations in shot 140407 (Fig. 1.10). Interestingly, there is little to no change of density fluctuations observed with ECH across the low to intermediate wavenumber range, but low-k ($k_\theta\rho_s< 0.6$) temperature fluctuations measured
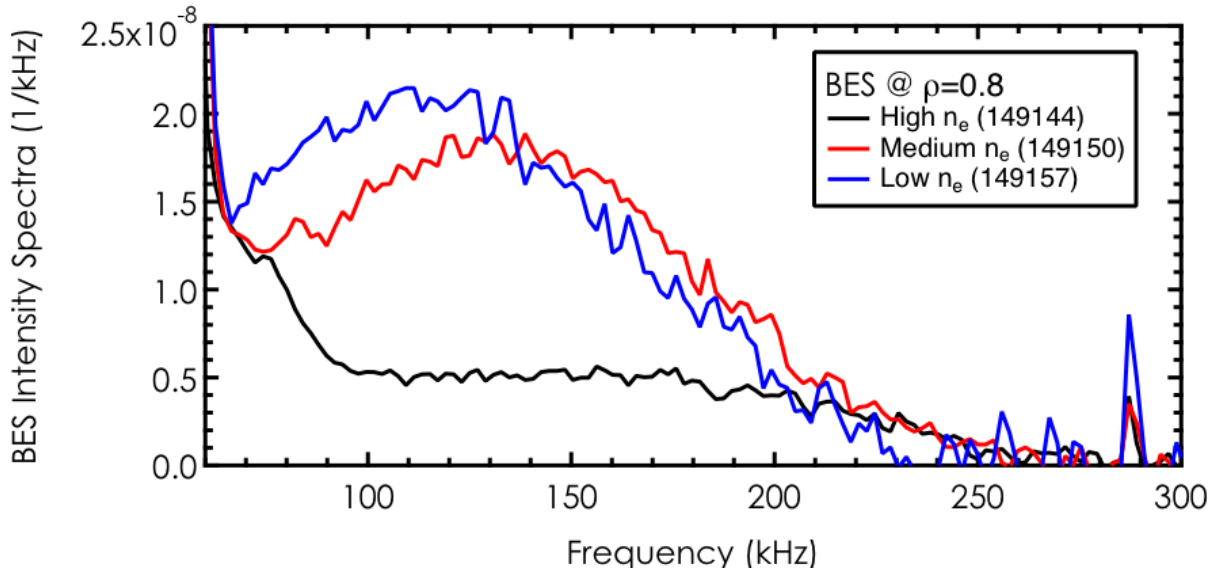
Fig. 1.8. Changes in normalized intensity level δI/I spectra measured by BES for QH-mode discharges from the 2012 experiment

by CECE (Correlation Electron Cyclotron Emission Radiometry) increase significantly. The wavenumber range accessible by CECE is limited by the spatial resolution of the collection optics (~ 3 cm, corresponding to $k_\theta \le 2$ cm^{-1}).

The final experimental result to date from these discharges is the measurement of low-k density fluctuations at rho=0.75 obtained via BES. The BES results shown in Fig. 1.8 correspond to the 2012 experiments cases shown in Fig. 1.7, and do not exhibit a simple correlation with the measured profiles, but do seem well-correlated with the ion thermal diffusivity χ_i. This correlation is likely best understood by noting that the BES system only measures "low-k" fluctuations with $k_\theta \rho_s < 1$ due to its viewing optics, and finite Larmor radius effects require that those scales dominate the ion (but not electron) heat transport. The combination of near-zero low-k turbulence and χ_i, and large χ_e, suggests that shot 149144 may be dominated by intermediate-to-short wavelength TEM/ETG modes, whereas shots 149150 and 149157 likely have more significant levels of low-k ITG modes (which would drive the finite χ_i). Developing an understanding of the full
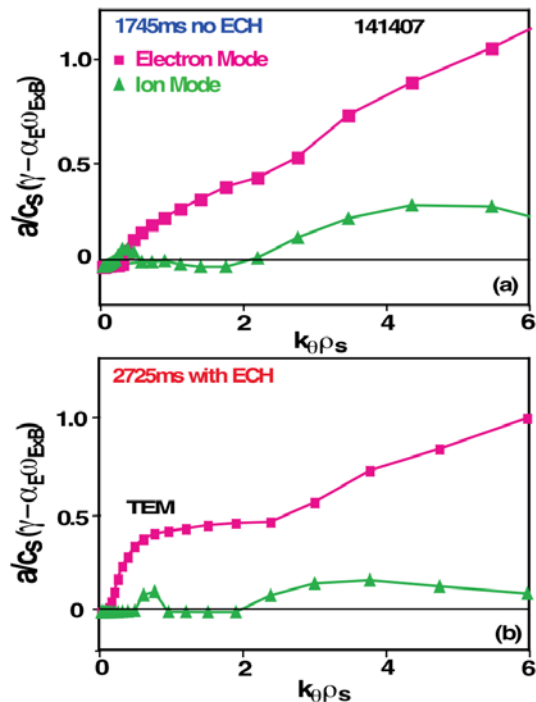

Fig 1.8b Net linear growth rate from TGLF for the low density QH-mode(r/a=0.6); (a) without ECH; (b) with ECH. The ExB shearing rate has been obtained from CER data
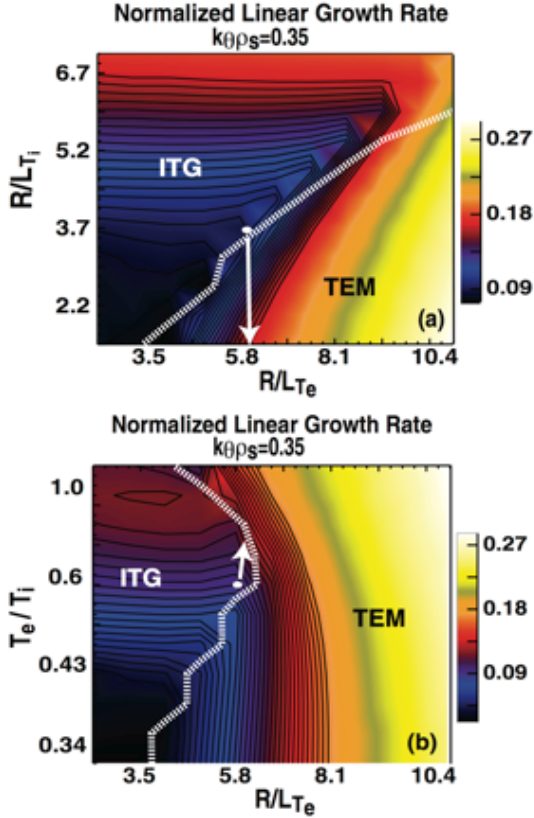
11

Figure 1.9 Maximum linear growth rate from TGLF versus (a) electron and ion temperature gradient; (b) electron temperature gradient and electron-to ion temperature ratio. The arrow indicates the modification of gradients and T_e/T_i when ECH is applied.
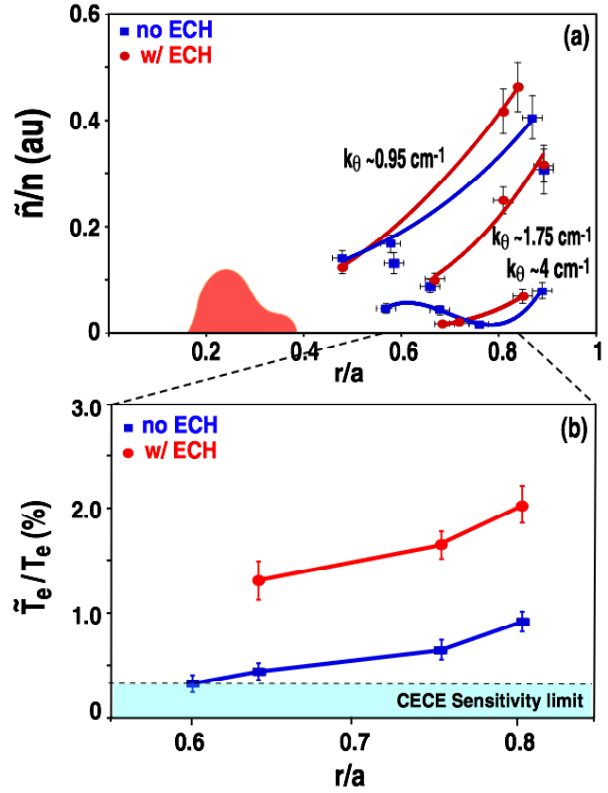
Fig. 1.10 (a) Radial profiles of low-k and intermediate-k normalized density fluctuations for the low density QH-mode plasma with and without ECH at r/a~0.25; (b) radial profile of normalized electron temperature fluctuations.

interplay of plasma equilibrium parameters, heating sources, and turbulent transport is still ongoing. Modeling of these experiments is beginning now, and will be supported by a 2012 ASCR Leadership Computing Challenge award at NERSC.

In addition to increased electron thermal diffusivity ascribed to increased TEM fluctuation levels at radii outside the ECH deposition location, a surprising observation has been the large increment in ion thermal diffusivity observed for 0.25 < r/a < 0.8 with ECH. Due to the low normalized ion temperature gradient with ECH (R/L_{Ti} ~ 2) the plasma is likely stable to ITG modes outside of r/a=0.4, and the increased ion thermal diffusivity most likely originates either from low-k TEM modes or from other modes excited nonlinearly.

In the 2010 QH-mode experiment discussed here and above, only a moderate electron temperature increment was achieved with ECH outside of r/a~0. In order to affect a larger increase in T_e/T_i at large minor radii, and further decrease electron-ion collisional coupling in the outer core plasma, a second QH-mode experiment with off-axis ECH deposition was conducted in 2012. For an ECH deposition location of r/a=0.4, a large increment in T_e/T_i ($0.3 \leq T_e/T_i \leq 0.8$) has been realized in the transport-relevant outer

core plasma (r/a ~0.6), further reducing the collisionality ($0.08 \leq \nu^* \leq 0.16$). Figure 1.11 shows radial profiles of density, electron and ion temperature, and toroidal rotation rate. Density profiles are relatively well matched without and with ECH; and density pump-out due to ECH is only noticeable in the inner core. With ECH, the pedestal electron temperature reaches values of >3 keV, and the electron temperature is increased by more than 1.5 keV across the minor radius. Similar to the previous experiment with more central ECH deposition [Fig. 1.10], the ion temperature gradient is reduced; indicating increased ion radial transport. This reduction is most pronounced for r/a $\leq$0.6. However the reduction in toroidal rotation with ECH, which entended across the entire minor radius in shot 140407, is now limited to r/a <0.6. ExB shear due to toroidal rotation is therefore not substantially changed in the outer plasma in this experiment as ECH is applied. Preliminary transport analysis shows that the electron heat flux increases substantially at and outside of the deposition radius with ECH, while the increment in ion heat flux is moderate (Figure 1.12).

Preliminary linear stability calculations with TGLF indicate that ITG modes are dominant for $0.4 \leq$ r/a $\leq$0.75 before ECH is applied (Fig. 1.13a). With ECH, a transition from an ITG-dominated regime to a TEM regime occurs for r/a > 0.6. Figure 1.13 shows the normalized linear ion and electron mode growth rates for r/a=0.7 for shot 149231. The maximum TEM growth rate decreases slightly with ECH due to a slight reduction in the normalized electron temperature gradient, however the low-k TEM growth rate most relevant to transport increases substantially for $0.2 \leq k_\theta \rho_s \leq 0.6$. With ECH, the ITG growth rate decreases by nearly an order of magnitude. Experimentally, a large increment in electron temperature fluctuations is concomitantly observed with ECH, consistent with the ITG-TEM transition predicted by the linear growth rate
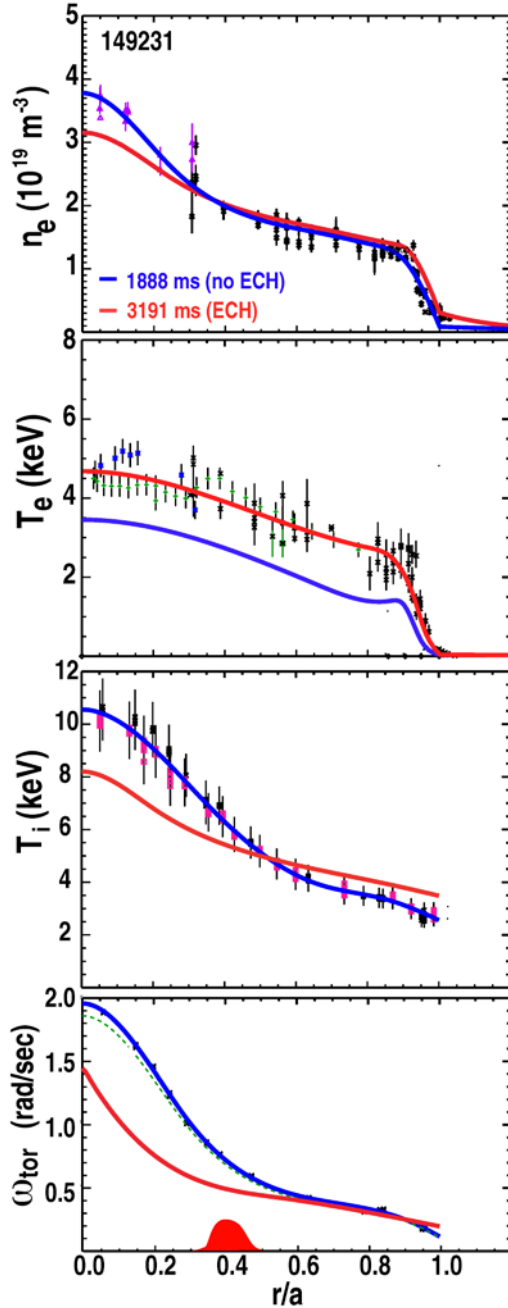

Figure 1.11: Radial profile of (a) electron density; (b) electron temperature; (c) ion temperature; and (d) toroidal rotation rate with and without off-axis ECH (2.4 MW).

analysis. Normalized electron temperature fluctuations increase from a value close to the diagnostic detection limit ($\leq 0.8\%$) to ~ 2 % with ECH, similar to the result obtained in the 2010 QH-mode experiment with more central ECH deposition [Fig. 1.10].
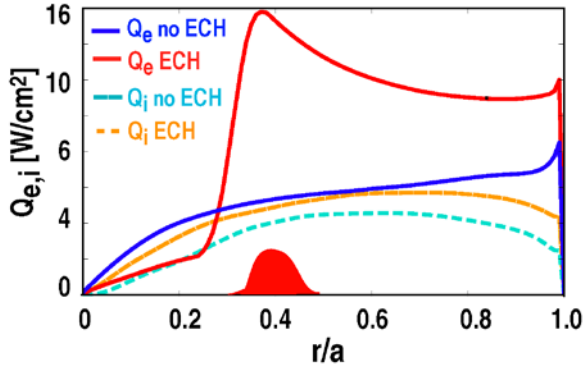

Figure 1.12: Radial profiles of electron and ion heat flux before (1888 ms) and during ECH (3191 ms) in shot 149231.

Analysis of ITG/TEM range density fluctuations is still in progress, and further detailed linear stability analysis is under way. More refined transport analysis and nonlinear gyrokinetic simulations are planned, taking into account energetic ion transport. Initial analysis of DBS fluctuation data indicates that low-k density fluctuation levels are not very substantially changed as ECH is applied. A wavenumber spectrum of density fluctuations in the upper TEM/lower ETG range [Figure 1.14], shows exponential dependence of fluctuation level on poloidal wavenumber with a spectral index of 2.6-3.4. With ECH, intermediate-k fluctuation levels are slightly increased, and the spectral index is reduced. Electron and ion transport are however dominated by low-k fluctuations in the outer core.
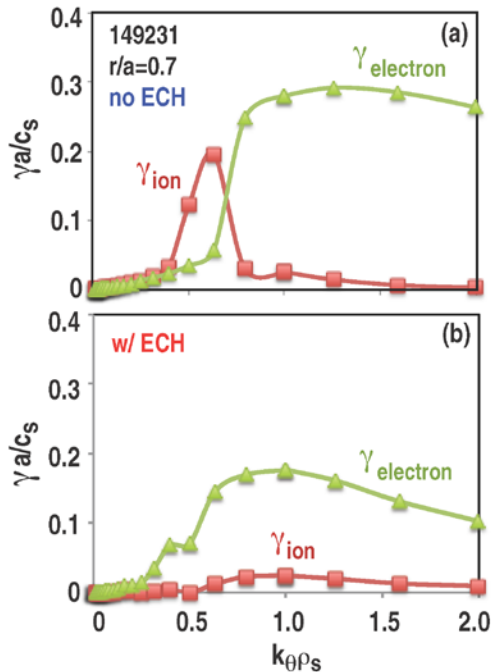

Figure 1.13 Ion and electron mode linear growth rates from TGLF (r/a=0.7); (a) no ECH; (b) with ECH applied.

14

In summary, a transition from an ITG-regime to a TEM-dominated regime occurs in electron-heat dominated, low density QH-mode plasmas with ECH. The electron thermal diffusivity increases by a factor ~2, most likely due to increased low-k TEM turbulence levels outside the ECH deposition radius. Ion thermal transport increases also. The observed synergistic increase in ion transport is attributed to TEM turbulence also as the ITG mode is stable or has marginal growth rate due to the reduced normalized ion temperature gradient in the outer core plasma (r/a>0.6).
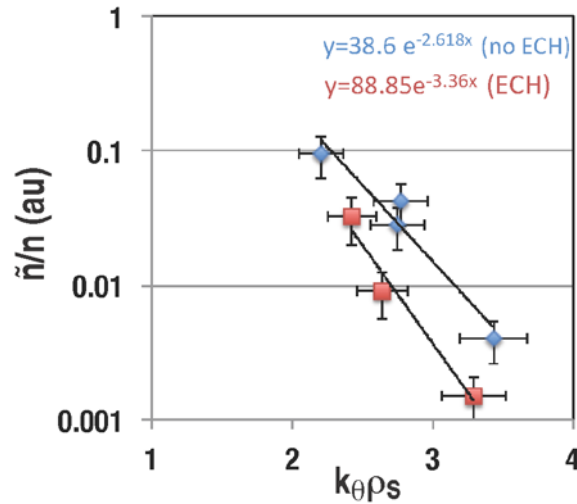

Figure 1.14 Wavenumber spectrum of density fluctuations in the upper TEM/lower ETG range shows exponential dependence of fluctuation level on poloidal wavenumber with a spectral index of 2.6-3.4. With ECH, intermediate-k fluctuation levels are slightly increased, and the spectral index is reduced.

At C-Mod, analysis of I-mode power balance is still in a preliminary stage for the new data and cannot yet be compared to the more extensive analysis just described above for the past DIII-D QH-mode experiments. To support future analysis, two key data sets have been identified. A low density, low current data set will provide a reasonable match to the Schmitz low density QH-mode data set from DIII-D. In this C-Mod data set, linear GYRO analysis indicates that the core of the low density higher Te I-mode is TEM dominant. A low density, high current data set provides a good match to the Holland high density QH-mode DIII-D data set. In these C-Mod I-mode plasmas, linear GYRO analysis indicates that the core of the I-mode remains ITG dominant. Future analysis will focus on analysis of reflectometer, CECE, Fast TCI and PCI fluctuation data to quantify differences in fluctuations between these two types of I-mode at C-Mod. In particular, we seek to determine if there are enhanced Te-tilde fluctuations in the TEM dominant cases, to connect with and compare to the low-density QH-mode plasmas with ECH at DIII-D.

1.D References

[1.1] N. T. Howard, et al. Phys. Plasmas **19**, 056110 (2012)

[1.2] A. E. White, et al. Phys. Plasmas **15**, 056116 (2008)

[1.3] C. Holland, et al. Phys. Plasmas **16**, 052301 (2009)

[1.4] T. L. Rhodes, et al. **51** 063022 (2012)

[1.5] J. Kinsey, Core Transport Session, April 12th 2012. "TGLF modeling and gyro simulations of the L-mode near edge region", http://ttf2012.pppl.gov/images/2012%20Program_v1-6.docx

[1.6] A. E. White, et al., 2012 APS invited talk

[1.7] A. E. White, et al. Phys. Plasmas **17**, 020701 (2010)

[1.8] L. Schmitz, et al. Phys. Rev. Lett. **100**, 035002 (2008)

[1.9] L. Schmitz, et al. *Nucl. Fusion* **49** 09500 (2009)

[1.10] L. Schmitz, et al. Nucl. Fus. **52** 023003 (2012)

[1.11] D. G Whyte, et al. Nucl. Fusion **50** 105005 (2010)

[1.12] A. E. Hubbard, et al. Phys. Plasmas **18**, 056115 (2011)

[1.13] C. Holland et al. Phys. Plasmas **18**, 056113 (2011)

[1.14] C. Holland, et al. Nucl. Fusion **52** 063028 (2012)

Table 1-1 Joint publications derived from or supporting 2012 JRT

Topics	Planned JRT related publications
Transport shortfall – especially at larger r/a	Rhodes - Physics of the Ip scan (fluctuation data, power balance, lin. and nonlinear GYRO analysis, TGLF analysis) Kinsey - Physics of the shortfall (scaling with q_{95}, comparison between TGLF and experiment) White - Dimensionless q-scan data set, explore shortfall with GYRO and TGLF.
L-mode Ip scan	Howard - Ip scan, comparing experimental trends with global, nonlinear GYRO results across C-Mod and DIII-D
L-mode Power scan, electron vs ion dominated plasmas	Howard - C-Mod validation paper on the RF power scan plasmas
I-mode/I-mode/QH mode comparisons	White, Holland, Schmitz "comparisons of I- and QH-mode

Section 2: Summary of C-Mod Research

2.A Experimental Plans: Three basic experimental thrusts were planned to explore the physics covered by the JRT. Each represents a distinct experimental approach to realizing the regimes called for in the JRT description.

Thrust 1.   Strong minority and/or mode conversion heating into moderate density L and I-modes: These experiments feature mainly electron heating with $T_e > T_i$ (T_e up to 7-8 keV) and a strong TEM drive via ∇T_e.

Thrust 2.   Very low density OH/L-mode regimes crossing the boundary between Linear Ohmic Confinement (LOC or Alcator scaling) regimes and the Saturated Ohmic Confinement (SOC) regime.

Thrust 3.   Internal Transport Barriers (ITB) with TEMs driven unstable by ∇n_e and ∇T_e. C-Mod achieves ITBs through application of off-axis ICRF heating.

A set of experimental proposals were prepared for the three experimental thrusts. By the end of FY12 ten of these received experimental time for a total of 13.2 run days. Table 2-1 lists the proposals and run time allocated to each. (Some of these experiments were run very late in the campaign; analysis is expected to continue throughout FY13.) In addition to specifying particular machine operation and discharge conditions, each required:

a) Full profile diagnostic information including (n_e, T_e, T_i, V_ϕ, P_{RAD}, Er…)

b) Fluctuation measurements including Phase Contrast Imaging (PCI) which produces chord integrated fluctuation spectra with k between 2 and 50 cm-1. Correlation reflectometry at frequencies up to 132 GHz and possibly Correlation Electron Cyclotron Emission. (The installation schedule of this last diagnostic was successfully accelerated to enable contributions the 2012 campaign.)

c) Impurity injection and measurement of time evolving impurity brightness profiles in order to extract impurity particle transport coefficients.

d) Long stationary periods in order to get the best possible profiles, fluctuation statistics and to achieve a zero particle flux condition for particle transport studies.

2.B Hardware upgrades and new core turbulence diagnostics at C-Mod

During the C-Mod opening (March-May 2012) we were able to carry out a number of key hardware upgrades for the two new core turbulence diagnostics, CECE and FastTCI. X-ray Imaging Crystal Spectroscopy (XICS) was upgraded to allow better measurements of impurity density and ion temperature at the high electron temperatures required for the JRT experiments. In addition, we took advantage of the Thomson scattering laser upgrade, which provided improved temporal resolution (100Hz) and better signal to noise. These new diagnostics were used to support the remainder of the JRT experimental research.

2.B.1 CECE

The development and deployment of a Correlation ECE (CECE) diagnostics was accelerated to support the JRT. A preliminary set of optics and electronics were installed at the beginning of the FY12 campaign and saw "first light" in December 2011. With those results in hand, a new mirror for the CECE turbulence diagnostic [2.1] was

designed, fabricated and installed in-vessel for the second half of the campaign. This mirror has a shorter focal length than the original mirror. The change results in the ~1 cm minimum of the spot-size occurring near $R_{maj} = 0.85$ m (instead of at $R_{maj} = 0.80$ m). The new mirror complements options for ex-vessel lenses in the optical system. By switching from a 10cm focal length lens in the ex-vessel optics to a 5cm focal length lens, the radial extent of the minimum spot-size region can be increased.

Several changes were made in the CECE electronics as well, in order to optimize the system for fluctuation measurements. First, a high pass filter was added in the IF section before video amplifier. This filter removes DC and low frequency signals, and improves the sensitivity of CECE system. Second, different IF filters, which have 200MHz bandwidth and different center frequencies, were used. To measure in the edge region and the core region simultaneously, a 14GHz filter pair was added. The existing 8GHz filter pair is used to measure in the core. Third, modification of the DC supplies were made to eliminate another source of noise. As will be discussed below, this diagnostic is now making T_e fluctuation measurements and was used on subsequent experiments.

Using the new CECE mirror, the first temperature fluctuation data were obtained in experiments to study changes in intrinsic rotation and momentum generation across the LOC/SOC boundary in Ohmic plasmas. Fluctuation levels of < 1% were measured near r/a = 0.8 with CECE in both SOC and LOC plasmas, but care must be taken to ensure that contributions from coherent noise peaks (still present in the electronics) do not add to the measured fluctuation level. The spectrum appears to broaden and change width dramatically in plasmas where the SOC/LOC boundary is crossed, as shown in Figure 2.1. It is not clear yet if these changes in measured spectral shape are due to Doppler Shifts or to underlying changes in the wavenumber spectrum / mode frequency of the turbulence. Linear gyrokinetic stability will be assessed for these shots to investigate any expected changes in mode frequency (e.g. as would be associated with an ITG to TEM transition).

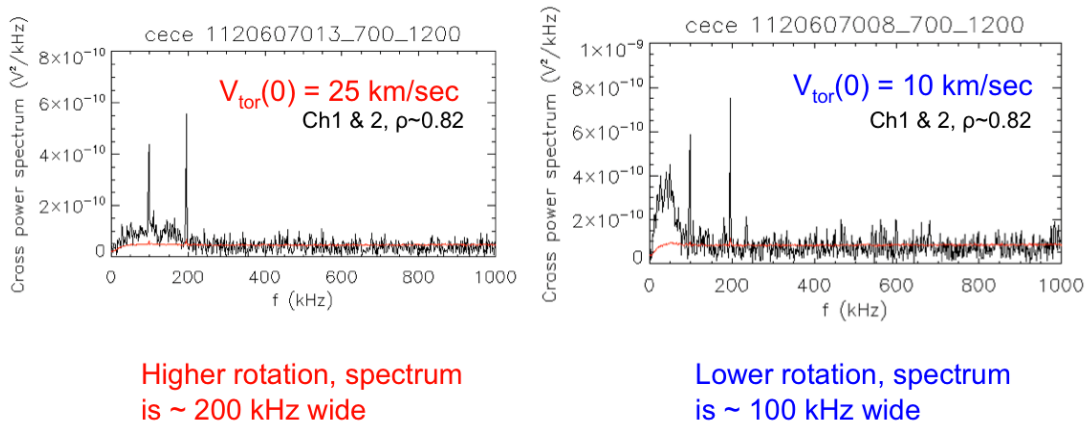*Figure 2.1. First CECE measurements of core (rho ~ 0.8) electron temperature fluctuations show broadening/narrowing of spectrum as density is scanned.*

18

2.B.2 FastTCI

Additional fast electronics were installed on the two-color interferometer [2.2]. This new diagnostic, FastTCI, complements PCI and also measures line integrated density fluctuations. In particular, this diagnostic will allow for the k-spectrum of n-tilde to be measured during Mode Conversion ICRF scenarios. For MC ICRF plasmas, PCI is used to observe and localize the MC wave, making it unavailable for turbulence measurements. Therefore, in these interesting high Te heated plasmas, we have previously been "blind" to the core turbulence. The FastTCI remedies this. This new capability allows us to make four different measurements in each plasma discharge with a single diagnostic: the line-integrated density and fluctuations, and the line-integrated density gradient and fluctuations. This fluctuations that instrument will measure are in the range $k \sim 0.5\text{-}5$ cm^{-1} with a k resolution of ~ 0.6 cm^{-1}. The FastTCI measurement has been calibrated and the noise floor for fluctuation measurements was estimated. Initial data was collected in a variety of plasma conditions with the interferometer operating in both "differential" and "absolute" modes. Analysis software is under development.

2.B.3 X-ray Imaging Crystal Spectroscopy

In Q4 of the JRT, C-Mod experiments were performed primarily using the I-mode confinement regime, resulting in core electron temperatures reaching 5-6 keV. In this range, the He-like argon charge state, normally used to measure the rotation and temperature profile using X-ray imaging crystal spectroscopy (XICS), is only present in the outer 1/3 to 1/4 of the plasma minor radius. The internal optical alignment of the x-ray spectrometer was modified to observe H-like Ar across the entire plasma cross-section while also having a dedicated measurement of H-like Ca in the core. These modifications have enabled the study of core impurity transport in high-performance I-mode plasmas at low-collisionality that were previously inaccessible because of the use of He-like Ar and He-like Ca emission as outlined in [2.3,2.4]. Initial results have demonstrated the improved coverage and the flexibility of the XICS analysis routines [2.5] will enable near-term access to recent Alcator C-Mod data using this modified setup.

2.C Summary of Thrust 1 Experiments and analysis

Strong minority and/or mode conversion heating into moderate density L and I-modes: These experiments feature mainly electron heating with $T_e > T_i$ (T_e up to 7-8 keV) and a strong TEM drive via ∇T_e. Figure 2.2 below shows linear gyrokinetic stability analysis for a particular but typical C-Mod discharge condition (geometry and current profile). The white crosses correspond to experimental data points from an L-mode power scan. The transition from ion dominated to electron dominated modes is clear from the direction of mode rotation and the slope of the growth rate contours. Specific experiments included under this thrust:

- Studies of steady low-density L/I-modes using a lower single-null (LSN) configuration and reversed field. Power was scanned using ICRH. These experiments were optimized for long steady-state periods to collect the best profile and fluctuation data.

- Investigation of core fluctuation modification at the L-I transition. These experiments were optimized for sharp transitions.
- Very low collisionality H-modes.

2.C.1 Validation of gyrokinetic transport models across the ITG/TEM boundary in L-mode and I-mode plasmas (MP 689). The goal of this JRT experiment was to produce high power L-mode and I-mode plasmas at low density, with dominant electron heating, in order to favor dominance of TEM over ITG. We obtained a *complete set* of profile data needed to test and validate nonlinear gyrokinetic codes. Datasets were obtained in steady discharges at high and low ICRH power with Bt = 5.4 T, Ip=0.7 MA, nebar=1×10^{20}/m^3 and at Ip=0.8 MA, nebar=0.8×10^{20}/m^3. Also for this experiment, we collected an excellent set of core turbulence data for the anticipated validation studies. The profile data for the ITG/TEM boundary crossing shots from this experiment are currently being analyzed. Ti and rotation profiles have been completed, and we are in the process of verifying TS and ECE data. Power balance analysis (TRANSP runs) will begin shortly. Nonlinear gyrokinetic simulations using experimental profiles are underway.
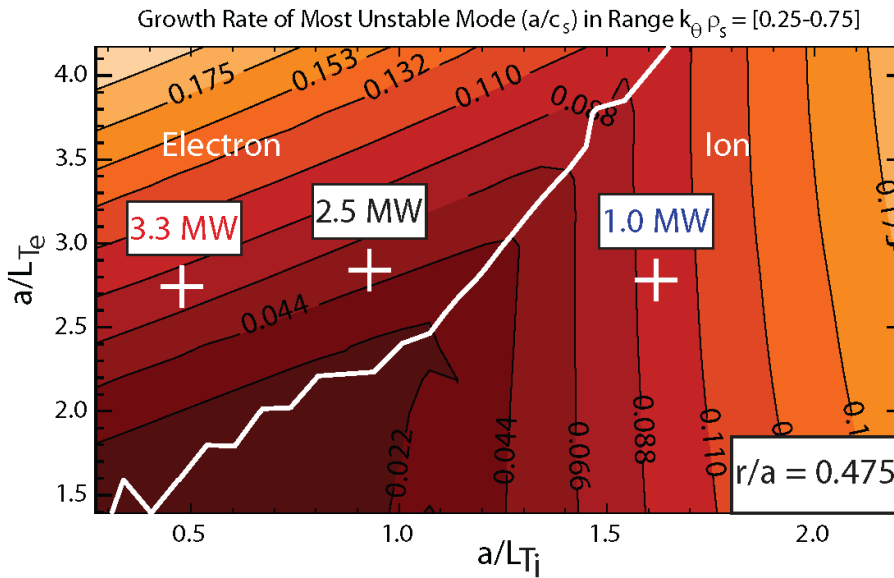

Fig 2.2. Contours of linear growth rate for the most unstable mode, with $k_\theta \rho_s$ between 0.25 and 0.75, are plotted vs the normalized ion and electron temperature gradients. The white line separates modes rotating in the ion diamagnetic direction from those rotating in the electron direction. The orientation of the contours show that the former have a growth rate sensitive to ∇T_i and are thus identified as ITG. The latter are sensitive to ∇T_e and are identified as TEM. The white crosses represent experimental data from a power scan in L-mode.

One novel aspect of this experiment was the use of linear gyrokinetic stability analysis **between-shots** to guide the experiment and to verify (as well as possible, with linear runs) that the target plasmas were indeed either TEM or ITG dominant. A new workflow was developed for generating GYRO input files and running the code on 160 cores of the local cluster. This required new analysis tools for profile fitting and a new approach to cataloging the GYRO input and output data using MDSplus. Shown in Figure 2.3 are the

results of the between-shot GYRO analysis for two of the shots, showing that according to the linear growth rates and real frequencies, the boundary between ITG and TEM was successfully crossed in the power scan in this experiment. This is the first time that linear GYRO has been used to inform the decision making in real-time during a tokamak experiment. Excellent profile and fluctuation data were obtained for this experiment, which will be used to support nonlinear GYRO runs using experimental profiles from selected shots. An interesting observation was rotation reversal correlated with the change in transport regime, connecting to experiments carried out at lower power and described below. These results can be compared directly to past DIII-D experiments in high-power L-modes, where the ITG-TEM boundary was crossed [2.6, 2.7].

In addition to the steady L-mode data, this experiment was also used to gather valuable data sets for core profile and core fluctuation reduction across the L-I transition. The reduction in core turbulence in I-mode appears linked to ExB shear (see Figure 2.4). Comparisons of C-Mod I-mode plasmas with DIII-D QH modes were be carried out as part of this JRT research [2.8, 2.9]. Using stepped and ramped RF power waveforms, we obtained datasets at the L-mode to I-mode transition in several discharges. We operated the high-resolution, spatially resolved soft X-ray diagnostic (HIREX_SR) with high time resolution (~5msec) for a number of shots in order to resolve the evolution of Ti during the sawtooth cycle, which will be important for detailed transport analysis.
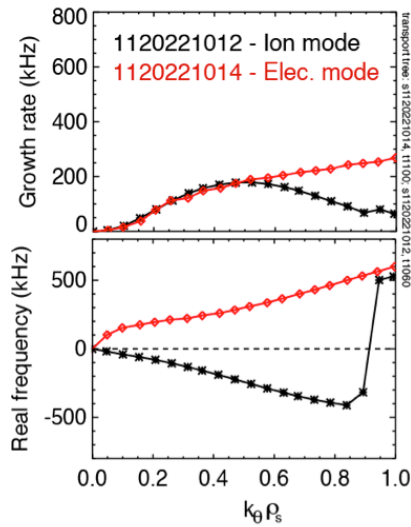

Figure 2.3 In-between-shot linear stability analysis performed with initial value GYRO during JRT 2012 experiment at C-Mod (MP 689). The red curves were from a shot with higher input power.
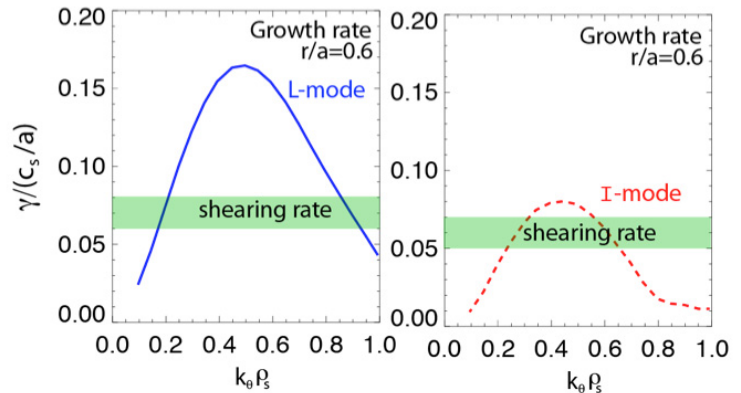
Figure 2.4. Reduction in core turbulence, which accompanies the L-I transition appears to be caused by the drop in ITG growth rate relative to the ExB shear from intrinsic rotation.

Follow up experiments repeated the basic scenario, but included Laser Blow-Off and impurity transport measurements. The additional run time was required to accommodate a modification of the high-resolution X-ray spectroscopy diagnostics used for measuring

Ca^{18+} profiles. (At the time it was not possible to obtain these impurity profiles and measurements of Ti and V simultaneously in high Te plasmas. A further modification of the instrument now allows this.) The new CECE and FTCI fluctuation diagnostics were also available for these experiments[2.10]. The goal of the experiment was to repeat as closely as possible several key discharges from run 1120221, which we are currently using to validate gyrokinetic models of transport. In this second day experiment, we gathered key fluctuation/transport data that we did not obtain on day 1: LBO, CECE, and fast TCI. These data support AE White's invited APS talk and POP paper.

The experiment consisted of an RF power scan, followed by a density scan, so that we can cross the ITG/TEM boundary with peaked rotation profiles and also we can probe changes in rotation from peaked to hollow profiles as density is scanned. We also filled in an intermediate power step with LBO data (1120706021) as well to support a new validation paper.
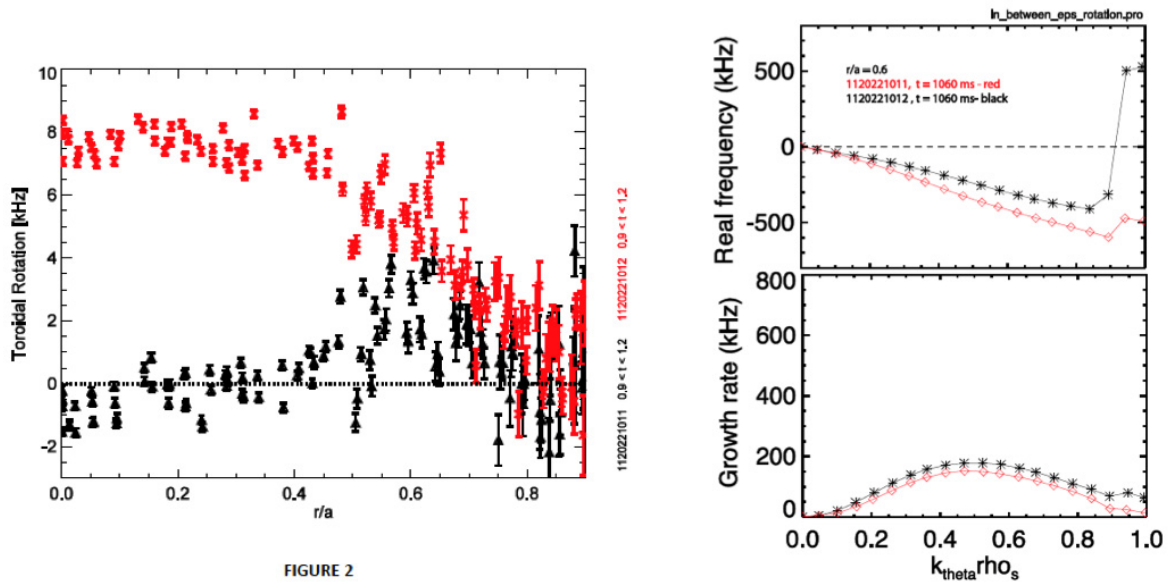

FIGURE 2

Figure 2.5 On the left, shots with peaked rotation profiles (red) and hollow rotation profiles (black) are both ITG dominant near half radius (right).

Data were obtained with LBO, CECE, reflectometer and FTCI in discharges that were matched extremely well (ne, Te, rot, WMHD, neutron rate, etc.) to the target discharges from 1120221 run day. For the high power cases, more RF power was required to compensate for a higher H/D ratio. The next step was to match the ITG and TEM cases, but with LBO, all fluctuation diagnostics and the high-resolution x-ray diagnostic configured to measure injected impurity evolution profiles. These experiments were successful and STRAHL analysis is planned for these shots: Low power ITG case with LBO data 1120706008 and High power TEM case with LBO data 1120706029/30.

Scans of density to produce rotation profile changes/hollowing in RF plasmas were also successful. The initial observations of this effect are the subject of a publication by M L Reinke accepted at PPCF [2.11], and gyro-kinetic analysis of the new data set (including

the LBO and fluctuation data) will carried out (and summarized in A E White's APS invited talk.) Key shots of interest for STRAHL analysis are the two low power ITG cases with density scans resulting in a hollowing of the rotation profile as density is increased from nl04= 0.60-0.85Interesting changes in the rotation profile were observed in ITG dominant plasmas when line averaged density was scanned on a shot by shot basis by +_20%. These rotation changes appear to be independent of the ITG/TEM boundary crossing, which indicates that ITG dominant plasmas can support both peaked and hollow intrinsic rotation profiles, as shown in Figure 2.5.

2.C.2 Reduction of core turbulence and transport across the L-I transition (MP680)
The goal of this experiment was to study the evolution of core turbulence and transport across the L-I transition. This experiment exploits the fixed frequency O-mode reflectometer fluctuation diagnostic. Since I-mode is a low density (for C-Mod) high performance regime, the reflectometer has access to the region $0.4 < r/a < 0.9$. I-modes at low edge q tend to have the clearest L-I transition with a strong WCM (weakly coherent mode) and a clear drop in fluctuation amplitude < 100 kHz in the edge turbulence, at the same time that an edge pedestal forms. The experiments for MP 680 sought to explore core-edge coupling across the L-I transition to determine if there were
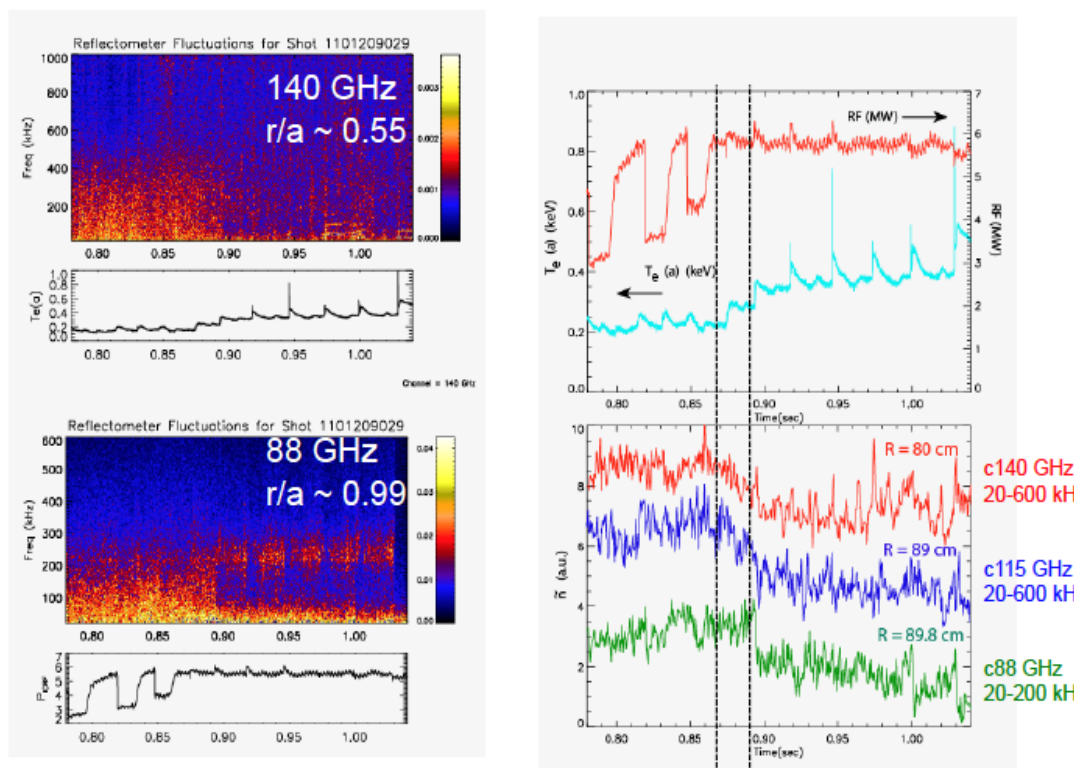

Figure 2.6. On the left are shown spectrograms of core (140 GHz) and edge (88 GHz) reflectometer channels. On the top right are shown the RF power and the edge temperature, $T_e(a)$, as a function of time. The integrated fluctuation levels from the reflectometer diagnostic are shown at the bottom right. Note that the core turbulence (red and blue) change before the abrupt drop in edge turbulence (green) at the L-I transition.

23

complementary changes in core and edge turbulence that give I-mode its favorable characteristics.

We have observed that after the L-I transition, core density fluctuations are reduced by up to 30%. This occurs in all I-modes examined, when a WCM is present in the edge. The fluctuation amplitude reduction is larger, deeper into the core, and smaller near the edge plasma.

We also find that contrary to a usual dynamic profile evolution accompanying L-H mode transitions [2.9], it is the core turbulence that changes before the edge turbulence at the L-I transition, as shown in Figure 2.6. Core density fluctuations are reduced at least a confinement time before the WCM appears. The reduction of core turbulence appears to follow modest increases in edge temperature, prior to formation of the full temperature pedestal. This observation indicates that synergistic changes in edge and core turbulence may be important for determining the threshold conditions for the L-I transition [2.12].
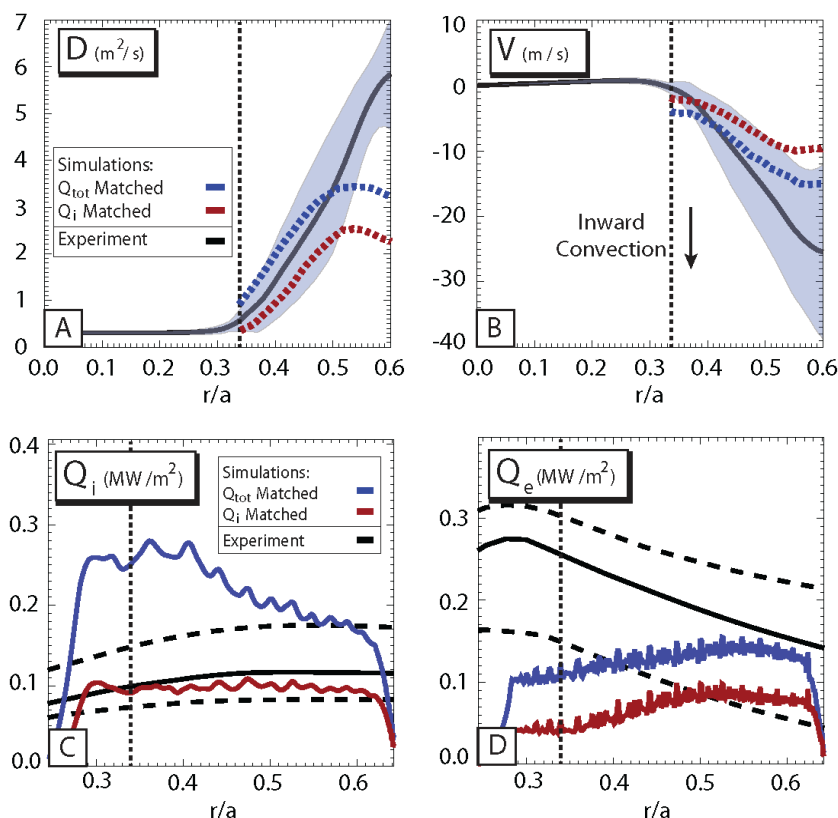

Fig. 2.7. Profiles of diffusivity and pinch velocity derived from experimental measurements are compared to values derived from GYRO simulations. At the same time, the simulations matched the experimental ion heat flux. The electron heat flux could not be matched with only low k modes included.

2.C.3. Impurity particle transport experiments and gyrokinetic simulations

Work has continued on analysis of impurity confinement experiments carried out in 2011. This includes work on discharges with dominant electron heating/electron transport and development of data analysis and simulation work-flow that was valuable

24

for other areas of JRT research. The experiments at C-Mod employed a laser blow-off system to inject trace quantities of calcium, a non-intrinsic, non-recycling impurity. The source function was monitored along with the profile evolution of Ca+18 in the plasma core using a novel, spatially resolving, high-resolution x-ray spectrometer. A single chord measurement of Ca+17 further constrained the impurity profile evolution. An iterative technique was then employed using the STRAHL atomic physics/impurity transport code to derive stationary diffusion and convective velocity profiles, $D_I(r)$ and $V_I(r)$, from the time evolving spectral brightness profiles [2.3]. These were compared to values derived from nonlinear gyrokinetic simulations using the GYRO code. A lengthy series of sensitivity studies was carried out to estimate the uncertainties in both the experimental and simulation values. As illustrated in figure 2.7, multiple transport channels were compared and within the derived uncertainties, the simulations could simultaneously match the values and shape of the impurity transport coefficients along with the ion heat flux [2.4]. Electron heat flux was not matched. A decrease in the impurity transport coefficients with plasma current was indentified experimentally and reproduced by nonlinear gyrokinetic simulation which demonstrated the importance of the q profile and the normalized density gradient. Overall, this represents an important step in transport model validation, which can help build confidence in turbulence models while identifying missing physics. This work was the first detailed quantitative comparison between experimental measurements of impurity transport and nonlinear gyrokinetic simulations. Work is underway to understand the role of higher k turbulence in electron energy and impurity transport and will be reported at the 2012 IAEA FEC conference.

2.C.4 Investigation of Core Impurity Transport in EDA H-Modes of Varying Collisionality (MP713)

Previous experiments had found a change in core density profiles and particle transport in low collisionality H-modes [2.13,2.14]. Quasi-linear analysis suggested that these changes were due to the relative dominance of ITG vs TEM transport [2.13]. To investigate this further and to add data for impurity transport, experiments were conducted to explore the transport of injected CaF2 in a variety of EDA H-mode conditions. We accessed a range of currents from 1MA to 430kA and ran at ICRF powers ranging from 1.5MW to 4MW. Initial estimates indicate that we obtained at least a factor of 5 change in effective collisionality ($\nu_{EFF} = 0.1\ Z_{EFF}\ <ne>\ R\ /\ <Te>^2$) between the low and high ends of the scan. The data from this run are currently being analyzed using the STRAHL code in order to obtain experimental profiles of the diffusivity D and the convective velocity V. In parallel with this analysis, GYRO (or other such gyrokinetic codes) simulations will be performed and compared to the experimental data in order to begin work on validation of gyrokinetic simulations in EDA H-modes.

2.D Summary of Thrust 2 experiments and analysis

Very low density OH/L-mode regimes crossing the boundary between Linear Ohmic Confinement (LOC or Alcator scaling) regimes and the Saturated Ohmic Confinement (SOC) regime: The saturated regime is coincident with L-mode, ion-dominated confinement – which previous analysis has shown to be dominated by ITG turbulence. While the LOC is an electron transport dominated regime. This boundary

also features a reversal in self-generated rotation and the disappearance of a moderate k fluctuation feature. Additional heating was applied in this regime to break covariances normally found in Ohmic data. Specific experiments included:

- Injection of impurities at very low density to study role of ion dilution in this regime and any connection to the TEM/ITG stability boundary.
- Scans of density/collisionality at constant Te/Ti and scans of Te/Ti at constant collisionality to study the role of "hidden" variables in LOC regime. This included a study of the role of auxiliary heating on the rotation reversal phenomena.
- Further investigation of high-frequency lobe found in LOC regime including PCI measurements at higher k, phase plate masking for spatial localization and improved measurement of Er to obtain plasma frame propagation direction.
- Cold pulse propagation in LOC vs SOC regimes.
- Studies of additional correlated phenomena including change in density gradient scale length, cross-field impurity confinement and parallel impurity confinement (leading to up-down poloidal asymmetries.)
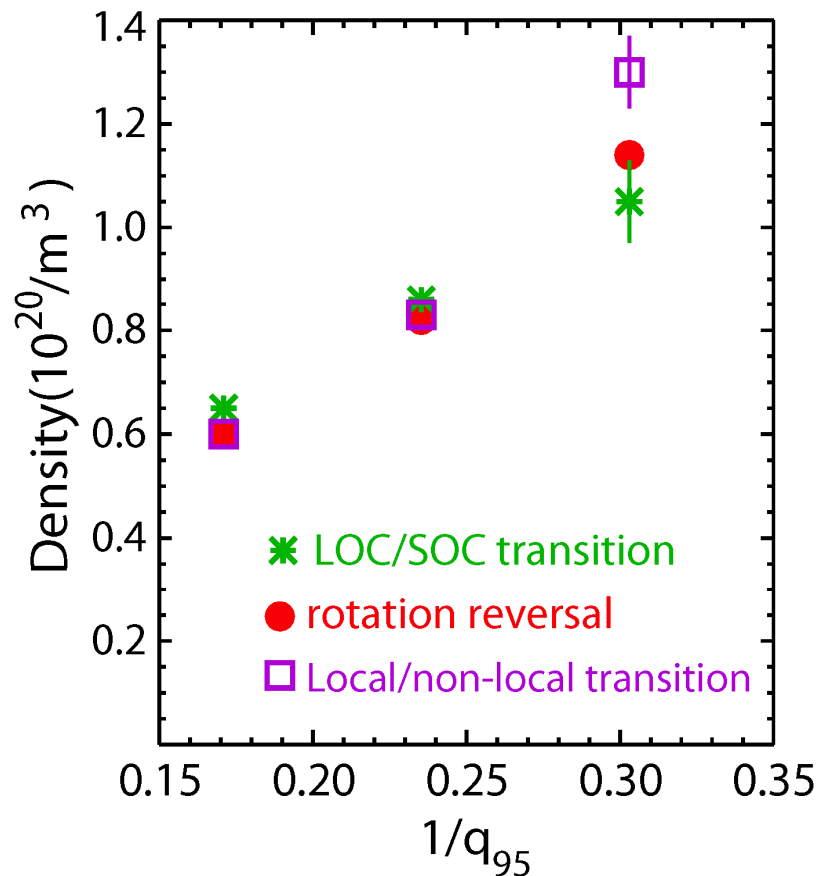

Fig. 2.8 The correlation between changes in energy confinement regime (green stars), rotation reversal (red circles) and local and non-local transient transport (purple squares) is illustrated. In each case the critical density for transition is plotted against the rotational transform value (1/q).

26

2.D.1 Hidden variables in neo-Alcator scaling (MP653)

Two run days were devoted to this experiment, obtaining a good set of data at 5.4 T, 1 MA. The aim of this experiment is to clarify the physics behind the linear density scaling in the neo-Alcator or linear Ohmic Confinement (LOC) regime. The linear scaling of global energy confinement time with density at low densities has long been observed ("Linear" Ohmic Confinement, or LOC). However, density scales out of the delta-f gyrokinetic Maxwell equations, and should only influence the core turbulent transport through collisionality, or other "hidden variables" which strongly co-vary with density in this electron-loss dominated regime. These include the electron to ion temperature ratio, inverse density gradient scale length, and impurity content. MP653 was motivated by gyrokinetic simulations and aims to break this covariance, both in LOC and in the transition to "Saturated" Ohmic Confinement (SOC), at which toroidal rotation reverses inside roughly the q=3/2 surface. The experiment used H-minority ICRF heating to (1) scan Te/Ti at constant density via power scans, (2) maintain constant Te/Ti during density scans by raising heating power with density, and (3) ramp density at constant heating power over a range of powers. By increasing heating power with density, the electron and ion temperatures were held within 10% of 2.5 and 1.5 keV, in two scans, as density increased from the lowest possible densities to well above the LOC-SOC transition. Slow density ramps overlaid the data from the steady state scans.

The critical density for rotation reversals increased with heating power, that is with plasma temperature, suggesting that collisionality may be a controlling parameter. Rotation behavior and reversals were identical in upper and lower single null discharges, which suggests that scrape-off-layer flows is not important for core spontaneous rotation in these cases. In the most recent cases, the core density fluctuation amplitude observed on microwave reflectometry exhibited large oscillations as the density oscillated around the LOC-SOC critical density. This could be an important indication of a change in turbulence characteristics near the rotation reversal density, and near the radius at which it occurs. Further analysis will be performed. Extensive profile and fluctuation data, including initial Correlation ECE, Phase Contrast Imaging, Polarimetry, Gas Puff Imaging, Reflectometry, Fast Two Color Interferometer, full ion temperature and toroidal rotation profiles, and low noise 50 Hz Thomson scattering data from the two new lasers, were obtained for comparison with gyrokinetic simulations. Gyrokinetic simulations with GS2 and/or GYRO are planned using synthetic diagnostics for comparison with fluctuation measurements. Because the electrons and ions are decoupled at low density, and heating power goes primarily to electrons, electron transport dominates the LOC regime.

2.D.2 Investigation of dilution effects on turbulence and transport in low density ohmic plasmas (MP696)

One thread being pursued to explain the low-density electron transport dominated regime is the role of ion dilution in reducing ion energy transport. As noted, Z_{EFF} is observed to increase at low density and the resulting dilution reduces the drive for ITG modes which dominate in the higher-density saturated regime. TGLF and GYRO analysis find that – providing the average impurity Z is less than 8 - the LOC regime electron transport became dominant due to excitation of dominant TEM/ETG turbulence. This experiment used deliberate injection of gaseous impurities in order to pin down the average impurity

charge. At the same time improved profile and fluctuation data were obtained as input for further gyrokinetic modeling with reduced uncertainties. Connections to the observation of spontaneous flow-reversal were also pursued, where impurity puffing in SOC drove a rotation reversal suggesting a transition to LOC.

Experimental results show that there is a decrease in the ion turbulence relative to electron turbulence when nitrogen seeding is added, or when the density is decreased. Flux-tube gyrokinetic runs have been completed and are under analysis. TGYRO and TGLF were used to try to get profiles that match the transport - reasonable can be obtained only between r/a = 0.6 and 0.8. Inside of r/a of 0.5 no turbulence predicted there by GYRO (the profiles are too flat to excite turbulence) and neoclassical transport is also too low to account for the heat flux observed. The sawteeth are a possible explanation, but the sawteeth on these ohmic discharges are quite small and don't extend out to r/a of
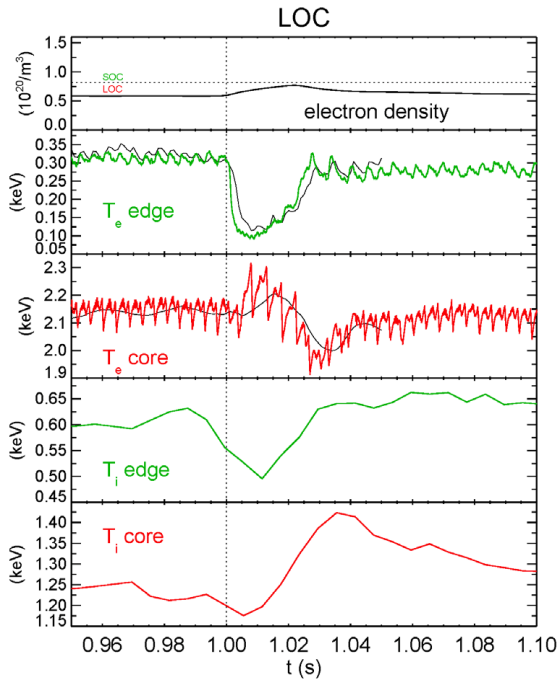

Fig.2.9a Time histories of the electron density, edge electron temperature, core electron temperature, edge ion temperature and core ion temperature for an LOC discharge with a CaF₂
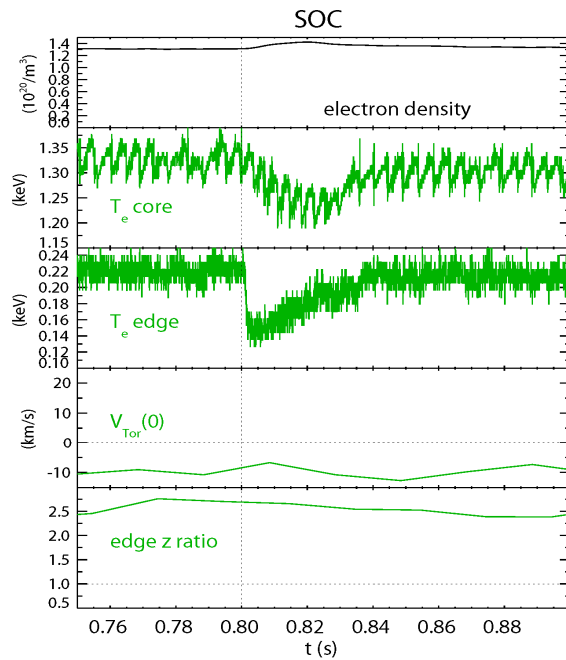
Figure 2.9b Core electron temperature drop following edge cooling at 0.8 s in the high collisionality SOC regime. Core rotation is counter-current and edge impurity density is up/down asymmetric.

0.5.

28

2.D.3 Nonlocal transport and the correlation with rotation reversal and the LOC/SOC boundary (MP672)

These experiments were aimed at understanding several longstanding mysteries in tokamak research: explanation of the observed edge up/down impurity density asymmetries [2.15, 2.16], the mechanism governing the linear Ohmic confinement (LOC, also known as neo-Alcator scaling) regime, the transition to saturated Ohmic confinement (SOC, L-mode) [2.17, 2.18] and the underlying cause of 'non-local electron heat transport' following cold pulses [2.19, 2.20]. Correlated with these is the rotation inversion or reversal process [2.20,2.21], in which the core toroidal rotation abruptly switches direction, with negligible effect on other macroscopic plasma parameters. Rotation reversal, the transformation from non-diffusive to diffusive heat transport, the switch of edge impurity density profiles from up/down symmetric to asymmetric and changes in turbulence propagation direction have all been observed dynamically during a single discharge with a density ramp to change the collisionality. Rotation reversals constitute a novel form of momentum transport bifurcation and have been induced by changes in the collisionality through the density, plasma current and magnetic field. The connection among rotation reversals, the transformation from LOC to SOC, saturation of electron density profile peaking and changes in turbulence characteristics has recently been demonstrated [2.22-25] and can be seen for example in figure 2.8. This connection is now extended to include 'non-local electron heat transport' and up/down impurity density asymmetries. All of these phenomena appear to be connected to the transition between electron and ion transport dominated regimes. Our investigations are aimed at understanding whether this is connected to a transition between ITG and TEM turbulence.

In the most recent experiments, thermal transport has been investigated by means of rapid edge cooling from impurity injection by laser blow-off. Shown in Fig. 2.9a are the time histories of the edge and core electron (from ECE) and ion temperatures (from x-ray spectroscopy) in an LOC discharge (5.4 T, 0.8 MA, $q_{95} \sim 4.2$, $n_e=0.6 \times 10^{20}/m^3$) with a CaF_2 injection at 1.000 s. Following the rapid edge cooling following the injection, there was a rapid *increase* of the core electron temperature on a time scale (~5 ms) faster than the diffusive time. This effect is suggestive of a short-lived internal transport barrier (ITB), triggered by
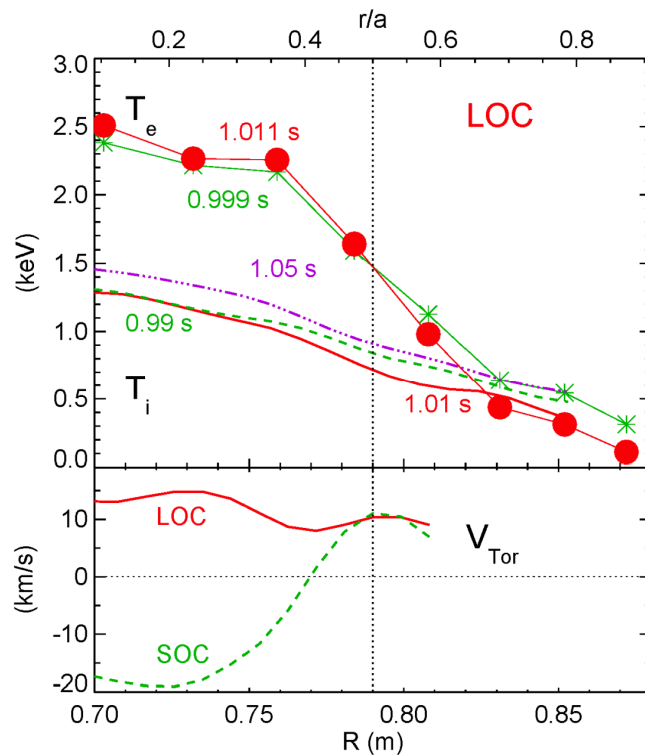

Fig.2.10 Electron and ion temperature profiles at three characteristic times during an LOC plasma (top) and rotation velocity profiles before and after a dynamic rotation reversal from LOC to SOC (bottom).

the sudden increase of the edge temperature gradient, which can be modeled with a sudden drop in the core electron thermal conductivity [2.19, 2.20, 2.26], and which persists for the duration of the edge cooling (~30 ms). The calculated electron temperature evolution is shown by the thin lines. This behavior can also be modeled with a transient heat pinch, which will be the subject of further investigations. There was also formation of an ITB in the ion temperature, which developed on a longer time scale; the central T_i reached its peak after 35 ms. This evolution of the electron and ion temperature profiles for the LOC discharge is shown in Fig. 2.10. The electron temperature reached its peak on a fast time scale of 12 ms (evaluated during the same phase of the sawtooth oscillations) and returned to its pre-injection shape after 30 ms. The flex point of the electron temperature profile was near R = 0.79 m r/a~0.5), marked by the dotted vertical line. R/L_{Te} at this location changed from 9.9 before the injection to 12.0 at 1.011 s. The ion temperature profile evolved on a longer time scale with a drop in the edge ion temperature occurring when the core electron temperature reached its peak. 7.1 at 1.01 s to 5.9 at 1.05 s. Interestingly the electron temperature profile flex point is very close to the intrinsic toroidal rotation reversal anchor point, as shown in the bottom frame of Fig. 2.10. These velocity profiles (from x-ray spectroscopy) were obtained from a discharge (q_{95}~4.2) with a dynamic rotation reversal [2.23] induced by ramping the electron density from 0.72 to $0.83 \times 10^{20}/m^3$. This suggests a connection, likely via a collisionality dependence, between the transient ITB formation (following edge cooling) in LOC plasmas and the intrinsic rotation reversal process.

Taken together, these results suggest an underlying unification of the disparate phenomena through consistent changes in the character of the turbulence. For example, spontaneous rotation can reverse direction if the momentum flux changes sign, which can occur if the residual stress (component of the momentum flux not proportional to the velocity or velocity gradient) changes sign due to a change in the mode propagation direction of the underlying turbulence [2.27]. One hypothesis is that at low collisionality in the LOC regime, the underlying turbulence is dominated by trapped electron modes and the rotation is directed co-current; at high collisionality in the SOC regime, ion temperature gradient modes prevail, the rotation is counter-current, and global energy confinement and density profile peaking saturate. Note however that related experiments with ICRF heating (described above in section 2.C.1) found profound changes in the rotation profile without a corresponding change in linear gyrokinetic stability. Nonlinear analysis of both sets of experiments is underway to help resolve the underlying physics. These results will also be pursued in the context of the emerging improvements to gyrokinetic modeling of momentum transport currently being implemented by the MIT theory group [2.28].

2.E Summary of Thrust 3 experiments and analysis
Internal Transport Barriers (ITB) with TEMs driven unstable by ∇n_e and ∇T_e. C-Mod can achieve ITBs through application of off-axis ICRF heating. The barrier is most evident in the particle transport channel and leads to strong density peaking. Similar phenomena have been observed with Ohmic heating alone. Specific experiments planned include:
- ITBs with an I-mode edge running in reversed field.

- Lower density, lower current ITB studies aimed at putting barrier foot in range of correlation reflectometer. The goal is to look for changes in fluctuations associated with the creation of the barrier.
- ITBs with very strong off-axis heating to drive ITBs with ∇n_e alone.
- On-axis heating of Ohmic ITBs.

2.E.1 Plasma fluctuation response to modulated ICRF heating of ITB discharges: MP602 crosses the ITG-TEM transition by applying heating in the present of a strong ITB density gradient
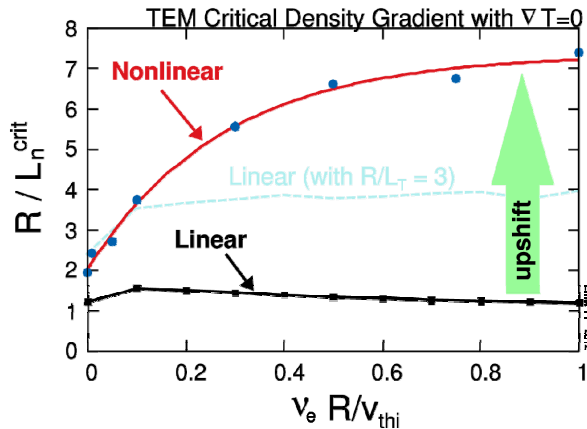

Fig. 2.11. A nonlinear upshift in the critical density gradient is found to increase with collisionality. While zonal flows are weak in ∇T_e TEM turbulence, they play a strong role in ∇n_e driven TEM turbulence. This introduces a new collisionality dependence and an associated strong sensitivity to temperature.

A new nonlinear critical density gradient for pure trapped electron mode (TEM) turbulence has been shown to increase strongly with collisionality, saturating at several times the linear threshold as shown in figure 2.11 [2.29]. The nonlinear TEM threshold appears to limit the density gradient in new modulated heating experiments on Alcator C-Mod ITBs (MP602). Gyrokinetic simulations show the nonlinear upshift of the TEM critical density gradient is associated with long-lived zonal flow dominated states. This introduces a new and strong temperature dependence that allows external RF heating to control TEM turbulent transport. During pulsed on-axis heating of ITB discharges, core electron temperature modulations of 50% were produced. Multiple edge fluctuation measurements show the edge response is out of phase with the core response. Bursts of line-integrated density fluctuations, observed on phase contrast imaging, closely follow sawtooth modulations of core electron temperature. A new limit cycle stability diagram shows the density gradient appears to be clamped during on-axis heating by the nonlinear TEM critical density gradient, rather than by the much lower linear threshold (see figure 2.12.). Fluctuation wavelength spectra are being quantitatively compared using profiles obtained from nonlinear gyrokinetic transport simulations using TRINITY/GS2. This work extends the comparison of gyrokinetic simulations and fluctuations spectra [2.33] by using modulated heating to separate core and edge fluctuations, and by simulating the radial profile of fluctuation intensity rather than just the ITB location. The fluctuation intensity from phase contrast imaging closely follows the temperature inside the ITB radius and is out of phase with fluctuations measured by a suite of edge diagnostics. In related work, we are implementing the first gyrokinetic exact linearized Fokker Planck collision operator [2.30] in GS2 and GYRO. Initial results show TEMs with $k_\theta \rho_i > 2$ are fully stabilized by classical diffusion for realistic collisionalities. Results from MP602 were presented in an

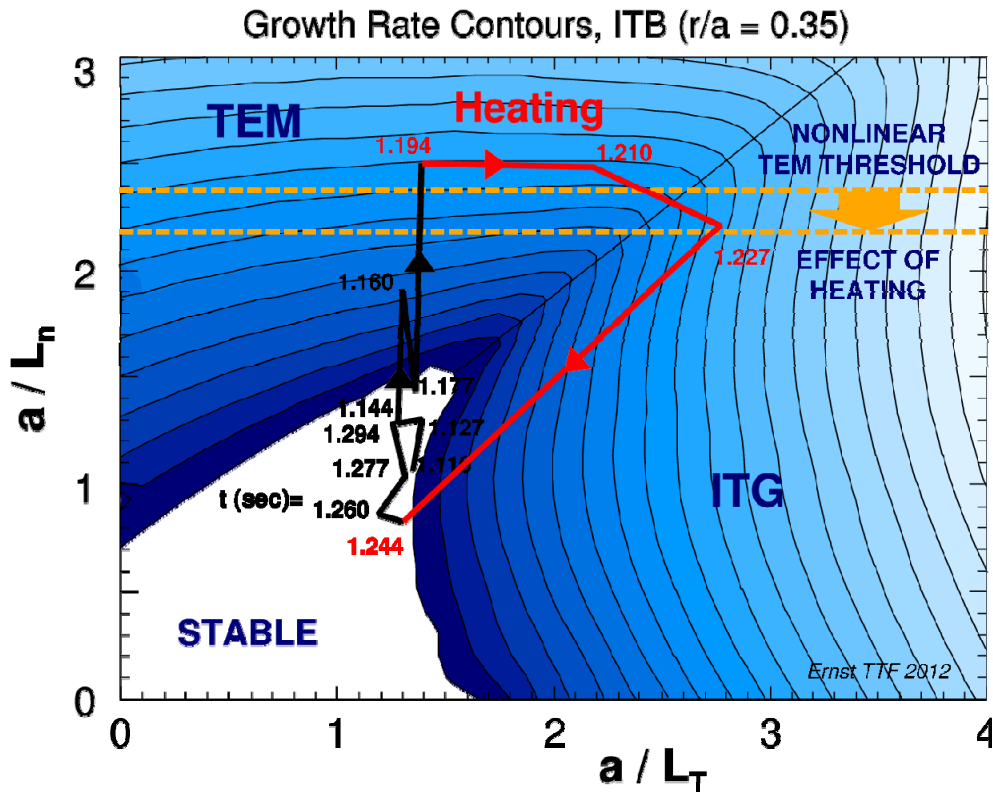invited talk at TTF by D. Ernst [2.29] and will be elaborated in an invited talk at the 2012 APS meeting.

Fig. 2.12. The trajectory of a modulated heating experiment is plotted in the plane of a/L_n vs a/L_T. The colored contours show the calculated linear growth rates. The experiment demonstrates that that the actual profiles are limited by the upshifted, nonlinear instability boundary.

2.E.2 Development of TEM in High Performance ITBs (MP691)

The primary purpose of this experiment is to study the formation of the trapped electron mode instability (TEM) that is associated with ITB control and saturation in Alcator C-MOD, in ITBs with off-axis heating alone (no central power). The instability should be driven by steep density gradients and hot plasmas resulting from high power off-axis ICRF heating. Figure 2.13 shows the evolution of the density profile peaking as the ITB develops. Identification of this instability relies upon observing the characteristic fluctuations with PCI, using techniques to determine the regions of origin such as sawtooth analysis and ICRF power modulation.

This run was completed in July 2012, with ITBs formed in 13 of 26 attempts. Complete diagnostic data for analysis was obtained in 9 of these. These were obtained with off-axis ICRF power between 3 and 4 MW, low field side. The increased power led to an ITB with 50% higher stored energy than previously obtained in an ITB plasma on C-Mod. Fluctuations characteristic of high power ITBs were observed on the PCI signal. Analysis of the PCI data to establish localization and direction of propagation is underway. Preliminary transport analysis for use in the gyrokinetic simulations has been

completed for half of the shots. It is anticipated that the linear gyrokinetic analysis will be completed shortly, with non-linear simulation and synthetic diagnostic analysis to follow.
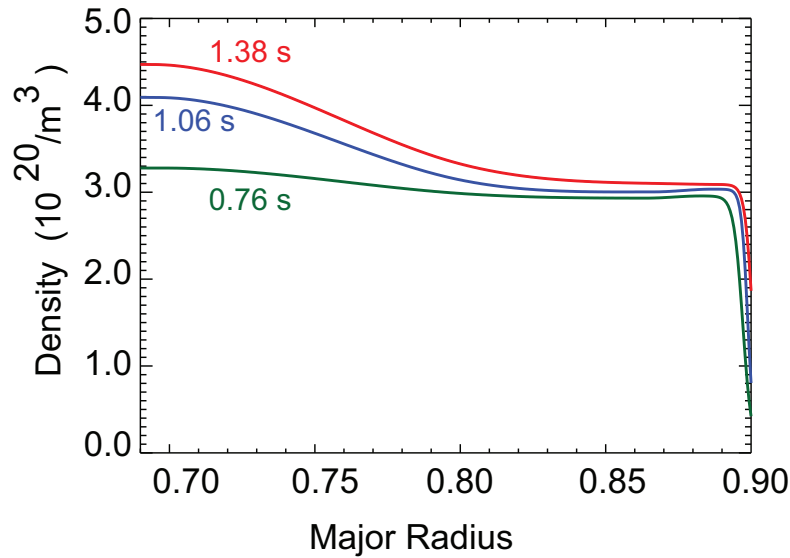

Fig. 2.13 Evolution of density profile in ITB generated by off-axis ICRF heating.

2.E.3 MP692: The influence of ion temperature profiles and toroidal rotation profiles on the formation of ITBs in I-mode plasmas.

This experiment investigated the ability to create internal transport barriers in I-mode via modification of the normalized Ti gradient and self-generated rotation shear – the same mechanism responsible for barrier formation in H-mode discussed above. While good I-modes were obtained throughout this experiment, ITBs were not formed.   Detailed analysis will look at the linear and nonlinear drift-wave growth rates and the magnitude of self-generated ExB shear. Figure 2.14 shows the evolution of the instability growth rates and the ExB shearing rate for a standard ITB developed from an H-mode plasma. The comparison should shed light on differences in transport mechanisms between these two regimes.   As noted above in section 1, I-mode plasmas have markedly lower collisionality when compared to H-mode, higher energy fast-ion tails from ICRF minority heating and thus more dominant electron heating.

2.F Plans for further analysis and simulations:

Continuing experimental analysis will rely on TRANSP for computation of RF power deposition, fast ion composition, ion and electron heat flux, and electron particle-flux, EFIT for magnetic equilibrium reconstruction, and STRAHL for impurity transport analysis. The core task here is to distill a picture of the transport fluxes that is consistent with the comprehensive diagnostic measurements, and to determine the uncertainties in these fluxes (the error bars)

The theoretical modeling will be extensive and include linear stability, quasi-linear and nonlinear turbulence simulations by TGLF, GS2 and GYRO, temperature profile predictions by TGLF, TRINITY and TGYRO, synthetic diagnostic simulation to compare

turbulence simulations to measurements of density fluctuations by the phase-contrast imaging (PCI) and electron temperature fluctuations by the correlation electron cyclotron emission (CECE) diagnostics. Additional code comparisons may be made through collaboration with other institutions, but these are not currently defined.
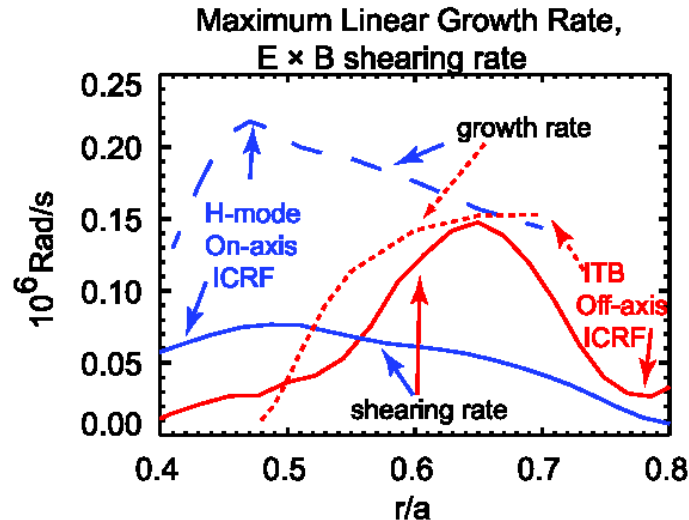

Fig. 2.14 Strong rotation is generated with both on and off-axis ICRF. However, with the heating off-axis the profiles have more shear. At the same the off-axis heating lowers the normalized ion temperature gradient and thus the ITG growth rate. These factors combine to produce an internal transport barrier

Several broad themes transcend the focus of individual experiments and will be the subject of in-depth modeling comparisons: the complex relationship between transport channels (ion, electron, particles and momentum) and their connection to the electron or ion dominated transport and the ITG/TEM boundary is found to be less straightforward than previously thought; we are exploring the role of ExB shear in transitions to reduced heat fluxes in the I-mode and ITB plasmas; understanding the condition and regions of the plasma where turbulence simulations based on experimental profiles under-predict the electron heat flux. We will study the importance of ExB change and $R//L_{Ti}$ change in ITB formation, the importance of electron turbulence drive in the center of an ITB plasma, how impurity transport fluxes depend on the level of heat flux and on plasma parameter scans, the parametric dependences of density peaking of electrons, D, H, and a range of low- to high-Z impurities.

C-Mod References

[2.1]   C. Sung et al. RSI, to be published, (2012)
[2.2]   C. Kasten et al. RSI, to be published, (2012)
[2.3]   N.T. Howard, et al., Nucl. Fus. **52**, 063002, 2012.
[2.4]   N. T. Howard, et al., Physics Plasmas **19**, 056110, 2012.
[2.5]   M. Reinke, submitted to RSI, 2012.
[2.6]   A.E. White et al., Phys. Plasmas. **17** (2010) 020701.

[2.7]   A.E.White et al., Phys. Plasmas **17** (2010) 056103.
[2.8]   L. Schmitz et al., Phys. Rev. Lett. **100** (2008) 035002.
[2.9]   L. Schmitz et al., Nuclear Fusion. **52** (2012) 023003
[2.10] C. Sung et al. Poster at 53rd Annual Meeting of the APS Division of Plasma Physics, Salt Lake City, (2011)
[2.11] M. L. Reinke, et al. accepted for publication, PPCF (2012)
[2.12] A. E. White, et al. in preparation for Phys. Plasmas (2012)
[2.13] C. Angioni, H. Weisen, et al., Nucl. Fusion 47 1326, 2007.
[2.14] M. Greenwald, C. Angioni, J.W. Hughes, J. Terry, H. Weisen, Nucl. Fusion, **47**, L26, 2007.
[2.15] J.L.Terry et al., Phys. Rev. Lett. **39** (1977) 1615.
[2.16] J.E. Rice et al., Nucl. Fusion **37** (1997) 241.
[2.17] R.R.Parker et al., Nucl. Fusion **25** (1985) 1127.
[2.18] F.X.Soldner et al., Phys. Rev. Lett. **61** (1988) 1105.
[2.19] K.W.Gentle et al., Phys. Rev. Lett. **74** (1995) 3620.
[2.20] P.Mantica et al., Phys. Rev. Lett. **82** (1999) 5048.
[2.21] [A.Bortolon et al., Phys. Rev. Lett. **97** (2006) 235003.
[2.22] J.E.Rice et al., Phys. Rev. Lett. **107** (2011) 265001.
[2.23] J.E.Rice et al., Nucl. Fusion **51** (2011) 083005.
[2.24] C.Angioni et al., Phys. Rev. Lett. **107** (2011) 215003.
[2.25] J.E.Rice et al., Phys. Plasmas **19** (2012) 056106.
[2.26] F.Ryter et al., Nucl. Fusion **40** (2000) 1917.
[2.27] P.H.Diamond et al., Phys. Plasmas **15** (2008) 012303.
[2.28] F. Parra, M. Barnes, P. Catto, Nuclear Fusion **51**, 113001, 2011.
[2.29] D. R. Ernst, Plenary Talk, US Transport Task Force Meeting, Annapolis, April 10, 2012.
        http://www.psfc.mit.edu/research/alcator/pubs/TTF/pdf2012/Ernst_TTF-talk_04-12.pdf
[2.30] B. Li and D.R. Ernst, Phys. Rev. Lett. 106, 195002 (2011).
[2.31] D. R. Ernst, et al., Phys. Plasmas 11(5) (2004) 2637.
[2.32] D. R. Ernst, J. Lang, W. M. Nevins, M. Hoffman, Y. Chen, W. Dorland, S. Parker, Phys. Plasmas **16** (2009) 055906.
[2.33] D.R. Ernst, et al., Proc. Of the 21st IAEA Fusion Energy Conference, Chengdu, China, 2006.

Table 2-1: Summary of C-Mod Run Time Dedicated to 2012 JRT

MP	Topic/Title	Run/Date	Run Time (days)
713	Impurity transport in H-modes of varying collisionality	120914 120808	0.5 1.0
703	Commissioning of the CECE diagnostic	120626	0.5
702	Cold pulse modulation experiments for the study of non-local heat transport	120919 120720 120620 120607	0.5 0.2 0.5 0.3
696	Investigations of dilution effects on turbulence and transport in low density Ohmic plasma	120626 120615	0.5 1.0
692	Influence of ion temperature profiles and toroidal rotation on the formation of ITBs in I-mode target plasmas	120830	0.9
691	Development of TEM in high performance ITBs	120719 120720	0.6 0.4
689	Validation of gyrokinetic transport models across the ITG/TEM boundary	120706 120221	0.9 1.0
680	Reduction of core turbulence and transport across the L-I transition	120921 120917	0.6 1.0
672	Non-locality and possible correlation with rotation reversal	120216 120106	1.0 0.7
653	Hidden variables in neo-Alcator scaling	120720 120718 120207	0.1 0.9 1.0
		TOTAL	**13.2 Days**

Table 2-2 C-Mod Publications derived from or supporting 2012 JRT

C-Mod Topics	JRT related publications Existing and planned
Diagnostic development, CECE and FTCI for Te and ne fluctuations (Supports all thrusts)	Sung "Design of a correlation electron cyclotron emission diagnostic" RSI 2012 Kasten "A new interferometry-based electron density fluctuation diagnostic" RSI 2012 Howard "Upgrades to CECE control and electronics" RSI 2013

Impurity and energy transport - Ip scan (Thrust 1)
 	
    Effects of low k turbulence
 	
    Effects of high k turbulence
	Howard "Measurement of plasma current dependent changes in impurity transport and comparison with nonlinear gyrokinetic simulation" PoP 2012
	
	Howard "Quantitative comparison of experimental impurity transport with nonlinear gyrokinetic simulations in L-mode plasmas" NF 2012
	
	Howard "Quantitative comparisons of experimental and gyrokinetic simulated ICRF and Ip dependent impurity transport" IAEA/NF 2013

Power scan, electron, ion and impurity transport (Thrust 1)	White "Multichannel transport in L-mode and I-mode plasmas at Alcator C-Mod and comparisons with gyrokinetic simulations" APS/PoP 2013 Howard "Validation of gyrokinetic simulations across the ITG/TEM boundary", PoP 2013
GK prediction shortfall (Thrust 1)	Howard "Comparison of experiments to gyrokinetic simulations of energy transport in outer regions of plasma" PoP 2013
H-mode collisionality scan, simultaneous energy, main ion and impurity particle transport (Thrust 1)	Chilenski "Energy, impurity and main ion particle transport in H-mode collisionality scans: experiments and gyrokinetic models" NF 2013
I-mode and QH-mode comparisons (Thrust 1) Changes in measured fluctuations and transport	White "Changes in core fluctuations across the L-I transition" PRL 2012
ICRF heated/rotation profile modifications (Thrusts 1 & 2)	Reinke "Density sensitivity of intrinsic rotation profiles in ICRF-heated L-mode plasmas" PPCF 2012

LOC/SOC (Thrust 2)
 	
    Electron vs ion transport
 	
    Hidden variables
 	
    Rotation reversal
 	
    Local/nonlocal transport
	Rice "Ohmic energy confinement saturation and core toroidal rotation reversal" PoP 2012
	
	Rice "Nonlocal heat transport, rotation reversals and up/down impurity density asymmetries" NF 2012
	
	Rice "A unified explanation of rotation reversals,

	confinement saturation and non-diffusive heat transport" IAEA/NF 2013
	Sung "An analysis of Te fluctuations and anomalous transport on Alcator C-Mod", PoP 2013
	Porkolab "Transport and turbulence studies in the linear Ohmic confinement regime" EPS/PPCF 2013
	Gao "Modeling of local and nonlocal transport across the LOC/SOC boundary"
	Ernst "Hidden variables in neo-Alcator scaling" PPCF 2013
ITB/TEM (Thrust 3)	Fiore "Producation of internal transport barriers via self-generated mean flows" PoP 2012
	Fiore "Gyrokinetic modeling of C-Mod ITBs" NF 2013?
	Ernst "Nonlinear upshift of trapped electron mode critical density gradient: simulation and experiment" APS/PoP 2013

SECTION 3.   DIII-D RESEARCH

3.   Introduction

The DIII-D contributions to the 2012 JRT included detailed comparison of theory/modeling with experimental results, primarily from experiments carried out in previous years, as well as results from four new experiments. Since the DIII-D 2012 experimental campaign took place from May through August 2012, there has been insufficient time for detailed analysis of the 2012 experiments.

The analysis work primarily focused on the electron and ion stiffness experiments. In addition, we discuss new analysis tools and development of metrics for assessing the agreement between models and experiment. These results are discussed in Secs. 3.A-3.D. In the four run days allocated to the JRT experiments by DIII-D management, we successfully carried out the following experiments.

1. Coupling of core electron and ion transport in TEM-dominated regimes
2. Transport model validation using high-density QH-mode discharges
3. Investigation of transport shortfall outside $\rho = 0.7$ in L-mode discharges
4. H-mode particle transport scaling with collisionality

The first two of these experiments are in Sec. 1 as part of the combined experiments. The last two are covered in Secs. 3.E-3.F.

3.A.   Measurements and Modeling of Electron Turbulence and Transport Stiffness

The transport model validation (TMV) group at DIII-D has led a multiyear investigation focused upon measuring how the local electron temperature gradient and multiple fluctuation levels vary at different plasma radii as the local electron heat flux is varied, while holding (as best as is possible) all other equilibrium parameters constant, and then using these measurements to test model and simulation predictions of the observed scalings. DIII-D contributions to meeting the JRT milestones using these experiments include a recently published [3.1] extensive gyrokinetic modeling study of a 2009 experiment [3.2], and documentation of experimental analysis and initial modeling results of a 2011 experiment which will be presented at the both the 2012 IAEA FEC [3.3,3.4] and APS-DPP meetings [3.5,3.6] (including an invited APS talk by J. Hillesheim).

3.A.1. *Comparisons of gyrokinetic simulation to DIII-D plasmas with modulated ECH heating*

The first DIII-D contribution in this area is a series of nonlinear, multiscale global gyrokinetic simulations modeling a 2009 DIII-D electron cyclotron heating (ECH) "swing" experiment [3.2]. In this approach, equal amounts of ECH on either side of a reference radius ($r/a = 0.6$) were modulated out-of-phase in time such that the local T_e gradient and electron heat flux passing through the reference surface are modulated in time, while keeping all other equilibrium parameters (including boundary conditions) fixed. The background plasmas studied were low current $(I_P = 0.8 \text{ MA})$, low density $\left(\overline{n}_e = 2 \times 10^{19} \ m^{-3}\right)$, inner-wall limited L-mode discharges. An extensive series of state-

of-the-art nonlinear gyrokinetic simulations modeling this experiment were performed with the GYRO code, and have recently been published in Nuclear Fusion [3.1]. To our knowledge, these have been some of the most expensive gyrokinetic simulations to date modeling actual plasma conditions, with each local simulation requiring 20,000-40,000 processor-hours and each global simulation requiring approximately 180,000 processor-hours on the Jaguar Cray XT5 system; access was provided by an INCITE award to the CSPM SciDAC center. The simulations included a full range of physics including gyrokinetic D and C ions, drift-kinetic electrons, like and interspecies collisions, magnetic fluctuations, and plasma shaping. The simulations resolved low-k turbulence $\left(\Delta k_\theta \rho_s = 0.07\right)$ but also extended up to $k_\theta \rho_s = 2.7-2.9$ in order to capture "intermediate-scale" $\left(k_\theta \rho_s > 1\right)$ fluctuations, which played a non-negligible role in the dynamics and were measured via the DBS system. In order to compare with the DBS measurements, a new synthetic DBS diagnostic was developed; its implementation is detailed in [3.1,3.7]. Visualizations of the turbulence are shown in Fig. 3.1.1, and comparisons of the predicted fluxes, T_e fluctuation levels, and ratio metric of $\tilde{T}_{e,RMS}/Q_e$ in Fig. 3.1.2.
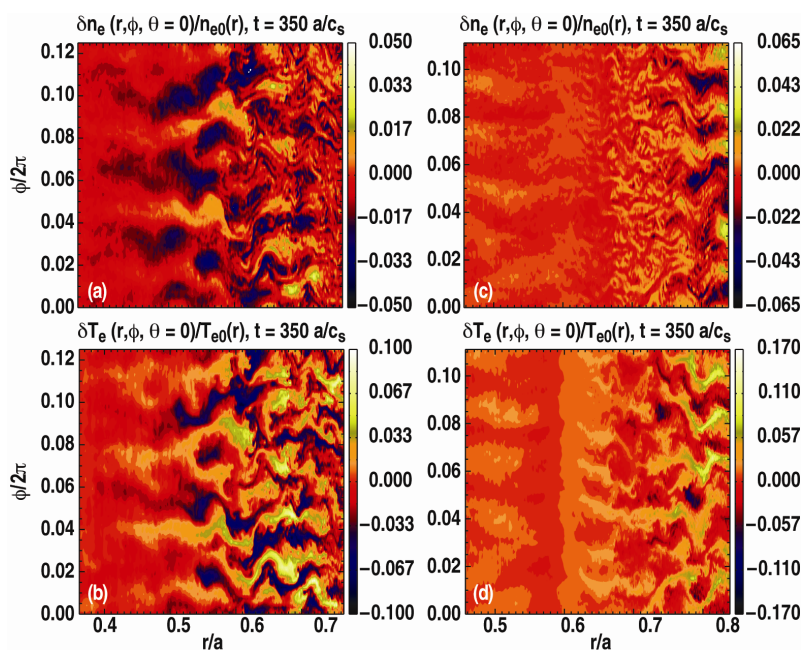

Fig. 3.1.1. Visualizations of locally-normalized electron (a,c) density and (b,d) temperature fluctuations for (a,b) high ∇T_e (inner heating) and (c,d) low ∇T_e (outer heating) at the reference radius.
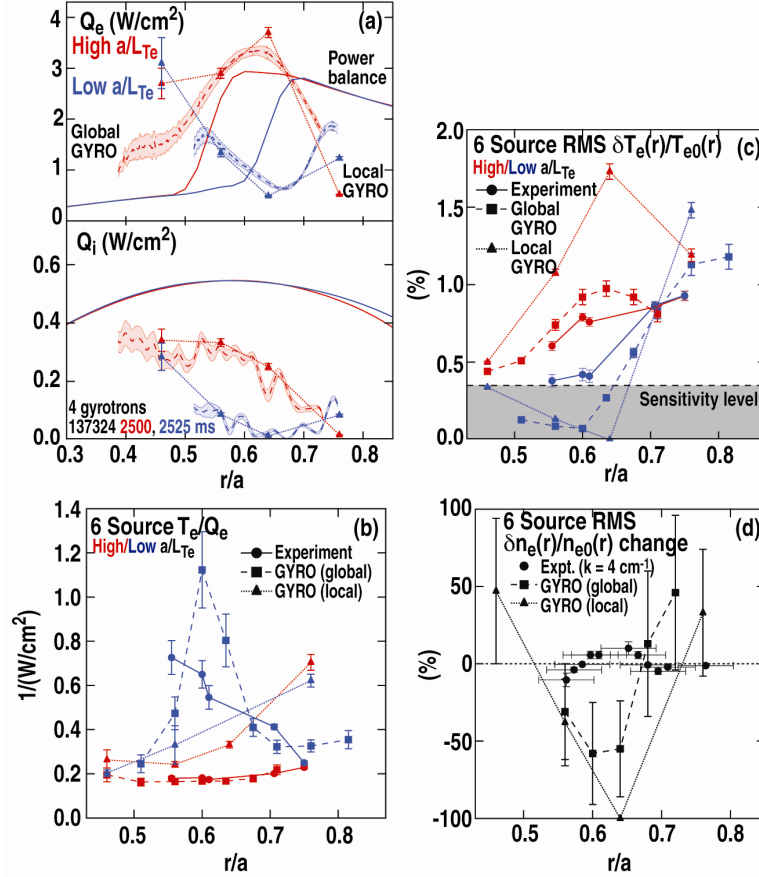
Fig. 3.1.2. Comparisons of GYRO predictions of Q_e and Q_i to power balance analyses, predicted RMS T_e fluctuation amplitudes $\tilde{T}_{e,RMS}$ to CECE measurements, the ratio metric $\tilde{T}_{e,RMS}/Q_e$ calculated for the GYRO predictions and experiment, and response of intermediate-k n_e fluctuations measured via to changes in T_e gradient.

The key findings of the study were:

- Global and local simulations generally yield qualitatively and quantitatively similar predictions of transport and turbulence levels, consistent with the small values of $\rho_s/a \approx 0.002$.
- Both local and global simulations predicted electron thermal transport levels and long-wavelength electron temperature fluctuation spectra with radial trends and responses to changes in a/L_{Te} consistent with the experimental observations.
- Using a variety of different comparison measures, the global simulations generally exhibited equal or better fidelity to the power balance results and experimental measurements than the local results, consistent with the rapidly varying gradient profiles induced with the localized ECH heating used in the experiment.
- Both the local and global simulations underpredicted ion thermal transport levels.
- Predictions of intermediate-k density fluctuations showed little correspondence with the experimental measurements.

Based on these findings, it is clear that improved methodology for assessing uncertainties and sensitivities in near-marginal conditions is needed. Toward this end, we have begun

work on developing a capability within the TGYRO framework [3.8] for efficiently calculating flux-matching profiles using global GYRO simulations (i.e. the n_e, T_e, T_i, and V_{tor} profiles which when input into the GYRO code yield predicted fluxes which match those calculated via the power balance analysis). A capability to efficiently calculate local flux-matching gradients using local gyrokinetic or gyrofluid models has also been implemented in TGYRO in the past year. Metrics based upon these calculations are being developed as well, and will be described further in Sec. 3.3.

3.A.2. *Analysis and modeling of local electron transport and turbulence stiffness in DIII-D*

Similar to the swing experiment described in the previous section, the 2011 experiments were performed in low current $(I_P = 0.8$ MA$)$, low-density $(\overline{n}_e = 1.9 \times 10^{19}~m^{-3})$ L-mode discharges. In these experiments, the resonant location of five ECH gyrotron sources (each providing ~ 500 kW of heating) was systematically varied about a reference radius, starting from all sources resonant outside the reference surface to one source resonant inside and four outside configuration, and so on until all five were resonant inside the reference radius. Using this approach, a very fine scan in the electron energy flux Q_e flowing through the surface, and corresponding local changes in a/L_{Te}, were obtained, while maintaining the local absolute temperature and density values relatively constant, as well as the net heating power and edge boundary conditions. In addition to the manipulations in resonant location of these five sources, a sixth gyrotron source was kept resonant outside the reference radius, but modulated at 28 Hz in order to obtain heat pulse measurements of the transport. This procedure was performed in Ohmic plasmas with no other heating, as well as in plasmas in co, counter-, and balanced NBI heating, about both $\rho = 0.4$ and 0.6 reference radii. Additional experimental details for various heating cases can be found in [3.9,3.4]. Modeling to date has focused on the conditions with only ECH heating centered about the $\rho = 0.6$ reference radius.

The global response of the T_e profiles to the variations in ECH deposition profile are shown in Fig. 3.1.3(a), where the (x,y) labeling convention denotes the number of gyrotron sources resonant inside $\rho = 0.6$ (x) and the number outside (y), including the modulated source. A clear rise in T_e at and inside the reference radius is observed, while T_e remains constant beyond the reference radius. Fig. 3.1.3(b) plots Q_e at $\rho = 0.6$ as a function of the measured value of a/L_{Te}, the most notable feature of which is the sharp break in slope between the points with $a/L_{Te} = 2.2$ and 3. This change is also observed in the amplitude of local T_e fluctuations measured with correlation electron cyclotron emission (CECE) radiometry [3.5,3.10], as shown in Fig. 3.1.3(c). While such a break seems consistent in some ways with a critical gradient for the electron temperature, the fact that neither the fluxes nor fluctuation levels go to zero below this break requires a more nuanced discussion than is feasible here. As such, we only describe this feature as the break point in the flux and fluctuation scalings presented in this analysis.
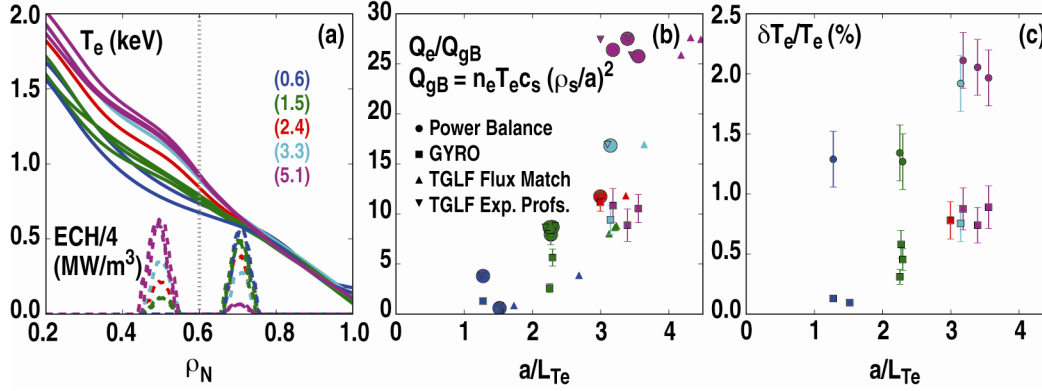
Fig. 3.1.3. (a) Response of T_e to changes in ECH deposition profile, (b) comparisons of TGLF and GYRO predictions of electron heat flux scaling with a/L_{Te} to experiment, and (c) comparisons of GYRO predictions of $\delta T_e/T_{e0}$ scaling with a/L_{Te} to experiment. Power balance calculations and experimental measurements are shown as (ℓ), GYRO predictions as ($\blacklozenge$), TGLF predictions using the experimental profile fits as inputs as (▫), and local flux-matching TGLF predictions as (▫).

These observations have been used to test the ability of both TGLF and nonlinear global GYRO simulations to accurately identify the break point and predict the scaling of transport (and turbulence in the case of GYRO) levels about this point. Global GYRO simulations are used based upon findings of the modeling of the swing experiment (Sec. 3.A.1), which found that at low gradient levels local simulations resulted in unphysical streamer-type eddies with radial correlation lengths on the order of the radial domain size, while inclusion of nonlocal effects yielded turbulence with physically relevant radial correlation lengths. Similar results were found in initial local simulations of these plasmas. The GYRO simulations included kinetic electrons (both passing and trapped), collisional effects, shaped geometry using a generalized Miller model [3.11], two gyrokinetic ion species (deuterium and carbon), and drift-kinetic electrons with fully realistic mass ratio $\sqrt{M_D/m_e} = 60$. The simulations are electrostatic based on the low values of β_e and linear studies which found no significant effect from their inclusion. The simulations used 40 toroidal modes with $\Delta n = 8$, corresponding to $0 \leq k_y\rho_s \leq 2.9$ with resolution $\Delta(k_y\rho_s) = \Delta n q \rho_s/r_{\min} = 0.074$, and binormal domain size $L_y = 1/\Delta k_y = 85\rho_s$. The total radial domain spanned the range $0.5 < \rho < 0.7$, corresponding to 104 ρ_s; 300 radial grid points were used yielding a radial resolution of $\Delta r/\rho_s = 0.35$. Quasilinear relaxation of the equilibrium profiles was prevented by using buffer regions and damping of the longest radial wavelength components of the $n = 0$ fluctuations as described in Ref. 20. Integration was done using Runge-Kutta integration with timestep $h = 0.01 \, a/c_s$, with the collisionless linear electron dynamics treated implicitly.

The first test of TGLF and GYRO was to simply input the local profile and gradient values derived from the experimental profile fits as inputs to the codes, and to then directly predict the local values of the particle and energy fluxes. Both codes predict values of Q_e consistent in both magnitude and scaling with a/L_{Te} at the lower experimental values below the break point, as shown in Fig. 3.1.3(b). However, only

43

TGLF appears to reproduce the highest fluxes, while the GYRO predictions appear to saturate at values lower than those observed for the highest values. Moreover, both TGLF and GYRO predict very low levels of the ion heat flux Q_i (which arises from the collisional exchange term as $T_e > T_i$ in these plasmas), several times lower than the power balance calculations. TGLF also predicts non-negligible particle fluxes Γ_e for some cases, such that the convective electron energy flux $Q_e^{conv} = 1.5 T_e \Gamma_e$ can be up to 50% of the total Q_e plotted in Fig. 3.1.3(b). To account for these discrepancies, a 2nd set of TGLF predictions were made, in which the local values of a/L_{Te}, a/L_{Ti}, and a/L_{ne} were systematically varied until the TGLF predictions of Q_e, Q_i, and Γ_e matched the local power balance calculations, while holding the local values of T_e, T_i, and n_e fixed. These results are also shown in Fig. 3.1.3(b), and demonstrate that the local flux-matching values of a/L_{Te} are systematically higher than those derived from the experimental fits. Along with this increase in a/L_{Te} relative to experimental values, we find that the local values of a/L_{Ti} must also be increase by 50% on average over the cases considered to match the local Q_i values, while a/L_{ne} must be reduced by 25% to yield no net particle flux (as the wall recycling source is assumed negligible at this radius). Developing a better understanding of the full physics underlying this upshift in flux-matching a/L_{Te} values relative to the experimental measurements (e.g. in terms of a change in the balance of TEM to ITG modes, or the balance between ∇T_e and ∇n_e driven TEM modes) is ongoing and will be reported in future work. Work is also currently underway to implement the capability to calculate self-consistent flux-matching global GYRO simulations within the TGYRO code as describe in Sec. 3.A.1, with the aim of investigating cases such as these.

In Fig. 3.1.3(c), the GYRO predictions for the measured $\delta T_e / T_{e0}$ levels are shown, in which the measurements are estimated using a simple synthetic diagnostic proxy of 0.5 ± 0.1 times the RMS amplitude of the finite-n T_e fluctuations in the simulation. This range was chosen based on the findings of a variety of previous validation studies [3.12-3.15] which find the full synthetic diagnostic calculations which convolve the predicted fluctuations in the (R,Z) plane with a two-dimensional spatial transfer function all yield attenuation levels of the gyrokinetic $\delta T_e / T_{e0}$ predictions by 40%-60%. Interestingly, these predicted fluctuation levels are systematically lower than the observed levels by a factor of two or more, and there is no clear evidence for a break point in the predicted fluctuation levels as is seen experimentally. This finding is contrary to what was found in the study of the swing experiment, which predicted both Q_e values and $\delta T_e / T_{e0}$ levels consistent with power balance and measurement, even while underpredicting Q_i as is found here. Fully quantifying the sensitivity of these findings to uncertainties in the driving gradients is currently underway, and future work will report those results along with the impact of including the full synthetic CECE diagnostic algorithm in the fluctuation amplitude predictions.

3.B.   Analysis of T_e / T_i scaling in L- and H-mode plasmas

A second focus of the TMV group's activities was investigating how transport and turbulence levels scaled with T_e/T_i in a variety of plasma confinement scenarios. In addition to the QH-mode studies described in the inter-machine section, the TMV group carried out studies measuring the responses of the turbulence and transport levels to changes in T_e/T_i induced via addition of near-axis ECH heating to beam-heated L- and H-mode discharges. Initial experimental and modeling results from the L-mode result were published in [3.14], which demonstrated the ability of nonlinear gyrokinetic simulations to quantitatively capture many aspects of the changes in density and electron temperature fluctuation spectra, as well as in the n_e-T_e crossphase (Fig. 3.2.1). Transport analyses and linear growth rate studies of the H-mode experiments were presented at the 2010 APS-DPP meeting [3.16] (Fig. 3.2.2). Motivated by improvements to gyrokinetic and gyrofluid models, the outstanding need to identify the source of the L-mode shortfall, and improved calibrations for some profile measurements, we have begun a full reanalysis of both the L- and H-mode experiments as part of our JRT work, and will report the results of both gyrofluid and gyrokinetic modeling of these experiments in planned future publications.
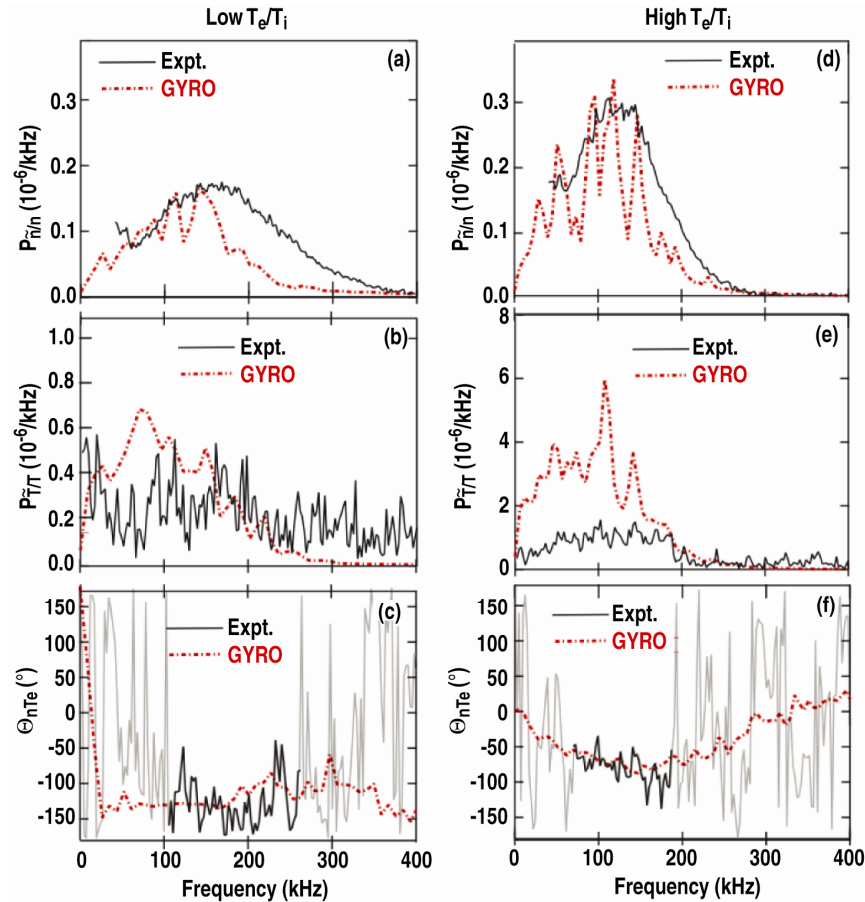
Fig. 3.2.1. Comparisons of experimental measurements and GYRO predictions for (a,d) density fluctuations measured by BES, (b,e) T_e fluctuations measured by CECE, and (c,f) the n_e-T_e crossphase measured by cross-correlating reflectometry and CECE diagnostics. From [3.14].
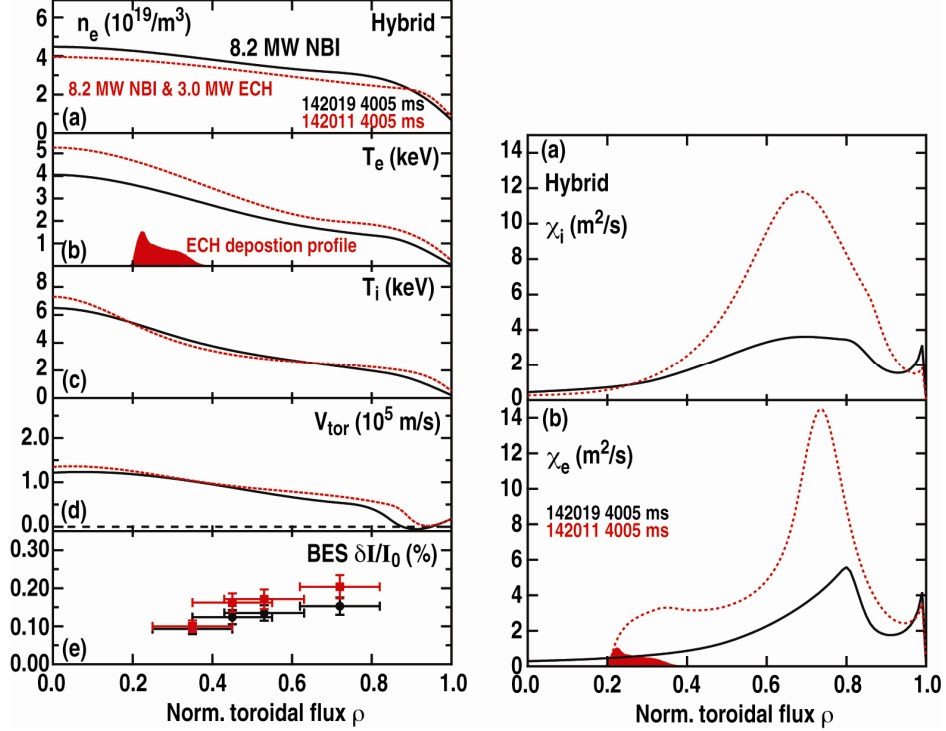
Fig. 3.2.2. (left) Measured equilibrium profile and turbulence changes in H-modes in response to 3 MW applied ECH heating centered at $r/a = 0.25$. (right) Changes in ion and electron thermal diffusivities induced by ECH.

3.C. Development of Validation Metrics and Results Database

In order to better synthesize and interpret the work done by the TMV group, during the JRT period we have begun to assemble a database of profile, fluctuation, power balance, and modeling results documenting the outcomes of various DIII-D validation studies, with the intention of expanding the database to include results from other groups whenever feasible. One of the primary motivations to begin this database was to create a broad dataset that could be used to improve existing validation metrics and design new ones, with an emphasis on more robust incorporation of uncertainties into these metrics. During the JRT a new metric was developed based upon the idea of local flux matching gradients, incorporating feedback and lessons learned from previous metric design studies. The local flux-matching gradients are those gradients which when input into a local transport model yield fluxes that match those calculated via power balance, while holding local density, temperature, and rotation profiles fixed. This approach therefore differs from the standard transport modeling approach (around which most existing metrics are based) in which profiles and gradients are self-consistently evolved. The advantage of the new approach is that it allows one to incorporate the inherent stiffness of turbulence models into the metric (via comparisons of predicted gradients rather than fluxes) while not requiring the assessment of model fidelity at one radius to depend upon model fidelity at other radii in the plasma. Uncertainty quantification is incorporated into the metrics by performing the gradient calculations for ensembles of plasma equilibria (assembled from either multiple timeslices or derived from Monte Carlo analysis of a single timeslice). A normalized error metric is then defined as

$$E_L = \left(a\!\!\!/_{L^{\text{model}}} - a\!\!\!/_{L^{\text{expt}}} \right) \Big/ a\!\!\!/_{L^{\text{expt}}} \quad , \tag{1}$$

and the uncertainty as a 95% confidence interval calculated using the standard t-statistic

$$\sigma_E = t^*\left(0.025, \min\left(N_{\text{model}}, N_{\text{expt}}\right)\right)\sqrt{\frac{\sigma_{\text{model}}^2}{N_{\text{model}}} + \frac{\sigma_{\text{expt}}^2}{N_{\text{expt}}}} \quad . \tag{2}$$

An example of this calculation (using the quasilinear TGLF model) for electron density and ion and electron temperature scale lengths in a specific shot are shown in Fig. 3.3.1. The results of calculating the metric for our initial database consisting of 8 NBI-heated L-mode discharges, 5 ECH heated L-mode discharges, and 7 NBI-heated H-mode discharges are shown in Fig. 3.3.2. In these plots, spline fits to the point profile measurements are used in the calculation, but the metric formulation is completely compatible with using gradients directly calculated from the measurements. The clear outcome of these metrics is an unambiguous demonstration that in the DIII-D L-modes considered, the local flux-matching gradients significantly exceed the experimental values, while no such trend is seen for the H-mode cases. This overprediction of near-edge gradients corresponds to an underprediction of the fluxes at the experimental gradients i.e. the L-mode shortfall, and thus allows us to quantify the magnitude, range, and scaling of the L-mode transport shortfall described in previous sections.
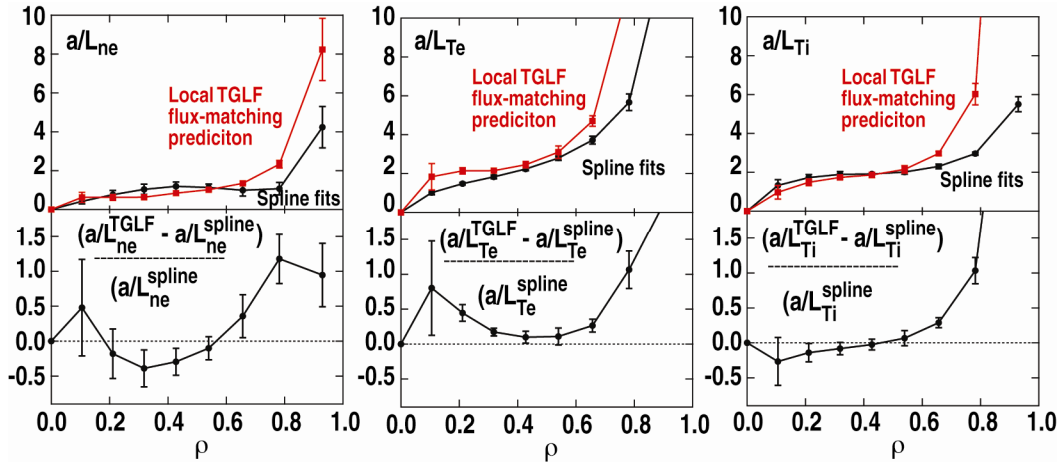

Fig. 3.3.1. Calculation of local flux-matching gradient error metrics for NBI-heated L-mode discharge 128913.
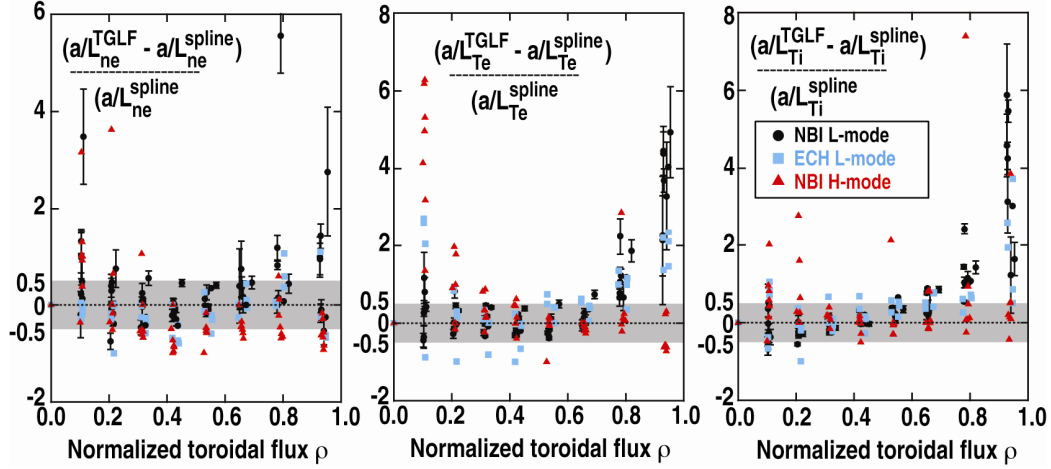
Fig. 3.3.2. Local flux-matching gradient error metrics calculated for a database of 8 NBI-heated L-mode discharges (ℓ), 5 ECH heated L-mode discharges (◆), and 7 NBI-heated H-mode discharges (⌐), demonstrating a clear overprediction of edge temperature gradients in L- but not H-mode plasmas (the so-called transport shortfall).

The breadth of measurements and modeling results incorporated in the database allows us to examine correlations and dependences between many different quantities, such as how the error metrics depend upon local collisionality, magnetic shear, fluctuation or transport levels (Fig. 3.3.3). Continued expansion of the database and analysis using new and improved metric formulations will allow us to develop improved understanding of the underlying physics of turbulent transport and greater confidence in knowing where current models can (and cannot) be expected to yield accurate predictions.
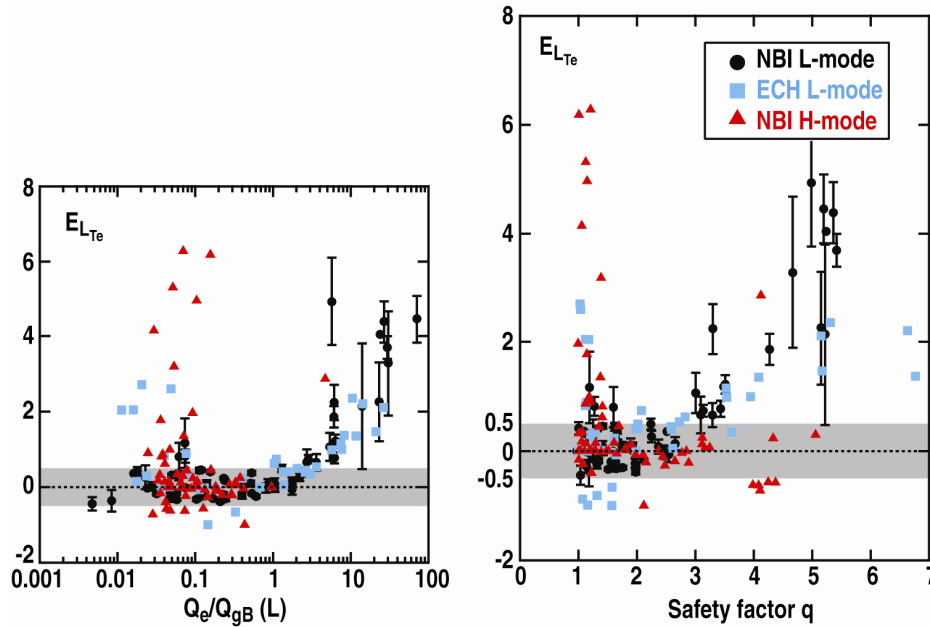
Fig. 3.3.3. Scaling of E_{Lte} vs (left) local gyroBohm-normalized electron heat flux Q_e and (right) local safety factor q.

3.D. Analysis of H-mode Ion Stiffness Experiment

For the H-mode experiments, a lower single-null plasma was chosen with ∇B pointing down to lower the L-H transition power threshold. The plasma was designed to have weak shaping (Fig. 3.4.1) under the premise that this would minimize the variation in the edge boundary condition and reduce the sensitivity of the resulting changes in profile shape on the boundary conditions. The total NBI power was scanned from ~ 3–7 MW at a low value of applied torque (~ 1.5 Nm) and from ~ 3–9 MW at higher values of applied torque (~ 3–7 Nm). The low torque cases were achieved by injecting the proper ratio of co-current and counter-current NBI while the higher torque cases used all co-current NBI. The resulting ion and electron temperature profiles are shown in Fig. 3.4.2. The focus here will be on the ion transport.
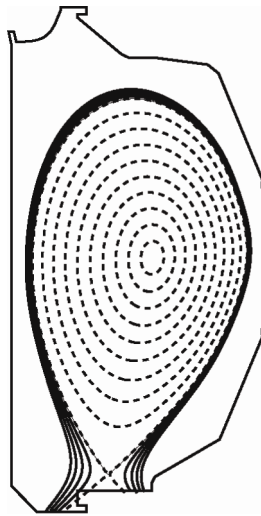
Fig. 3.4.1. Cross-section view of DIII-D plasmas used for the H-mode experiments.
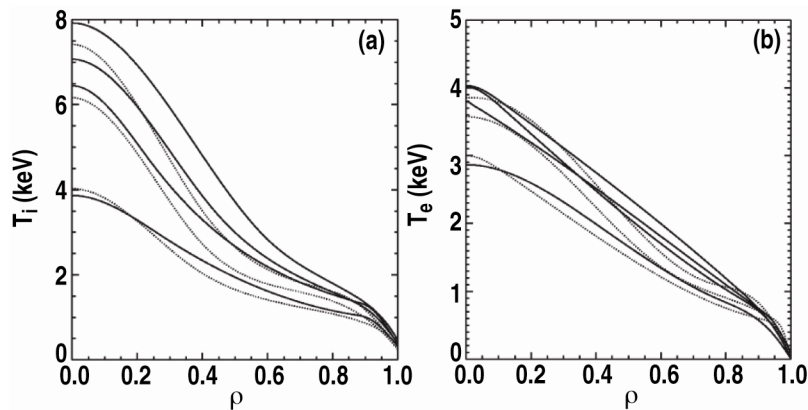

Fig. 3.4.2. (a) The fitted a) ion and b) electron temperatures vs normalized radius. The solid lines are the high torque cases with roughly 3, 5, 7, and 9 MW of total applied power (bottom to top). The dotted lines are the low torque cases with roughly 3, 5, and 7 MW of total applied power (bottom to top).

The flux-gradient relationship for the ions is shown for seven plasmas (three low torque, four high torque) at four different radii in Fig. 3.4.3. The solid lines in each of the panels

are a linear fit to the two datasets (low and high torque) with each point equally weighted and without constraining the fit to pass through the origin. This allows an assessment of the stiffness proxy directly. If the fit passes through the origin, then $S = 1$ and there is no stiffness. If the intercept at zero gradient is positive, as it is in most cases, then the incremental transport is actually weaker than the average value. Only in the case that the intercept is negative would stiffness be indicated. The fact that the intercept is near zero or positive in virtually all cases shown in Fig. 3.4.3 implies the data does not support a picture where the gradients are fixed by very strong transport above a threshold value. The only case where such a picture may hold is the low torque case at $\rho = 0.7$. In general, the transport is higher at low torque for the same gradient. If the $E_r \times B$ shear is correlated with the torque input as expected, the higher transport at low torque would be consistent with reduction in the underlying turbulence by $E_r \times B$ shear. On the question of a threshold, the data can be reconciled with a threshold as shown in Fig. 3.4.3(c) by fitting to a parabola opening to the right. The resulting fits show that both the low and high torque data can be reconciled with a common threshold gradient value ($\sim$ 1.5-2.0 keV/m) and stronger transport in the low torque case, consistent with weaker $E_r \times B$ shear. The picture of a common threshold and stronger transport at low torque is consistent with the data at all four radii shown. However, the data do not compel one to this explanation; the main evidence is the relative position of the data points at the lowest two power levels. An uncertainty analysis will be carried out to determine the confidence in the location of these points. But the fundamental issue with drawing a strong conclusion about a potential threshold is that the indicated threshold value lies below the range of the present data and is likely unachievable under these plasma conditions since the fluxes near threshold are likely lower than those needed to operate in H mode.
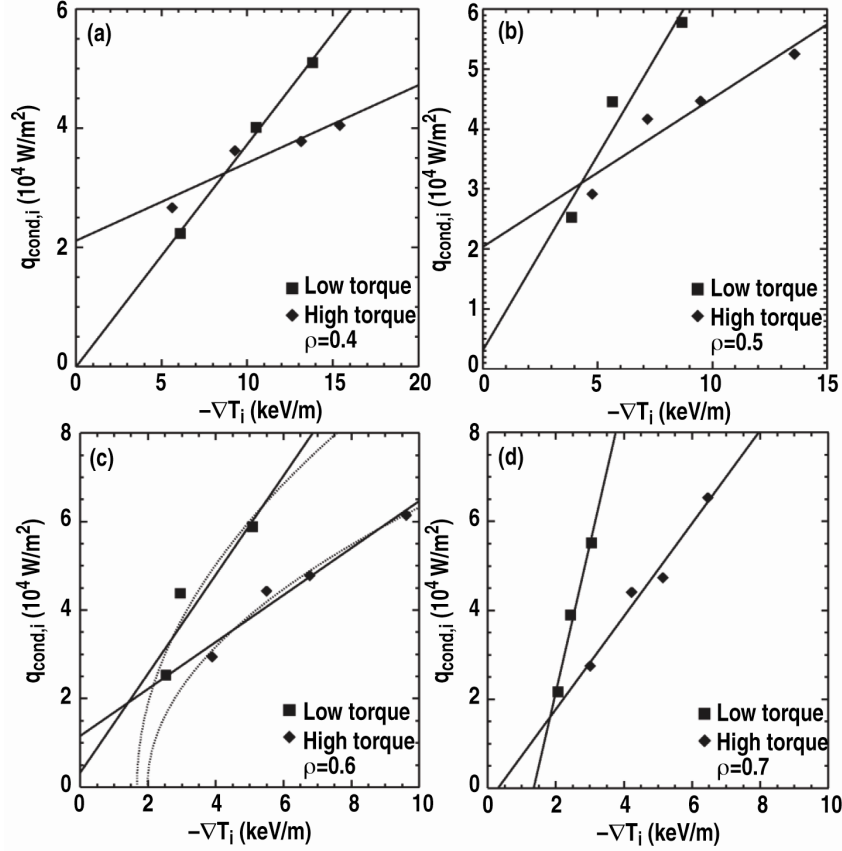
Fig. 3.4.3. The conducted power in the ion channel from power balance analysis vs the measured ion temperature gradient for (a) $\rho = 0.4$, (b) $\rho = 0.5$, (c) $\rho = 0.6$, and (d) $\rho = 0.7$. The squares are the low torque data and the diamonds are the high torque data.

The normalized fluxes and gradients for $\rho = 0.6$ are shown in Fig. 3.4.4. The variation in both quantities is substantially smaller than the corresponding unnormalized quantities [Fig. 3.4.3(c)]. The fact that the flux variation is reduced implies the variation is described well by the expected gyro-Bohm scaling of the flux and the influence of other uncontrolled parameters is either weak or cancels out. The variation in the normalized gradient (R/L_{Ti}) is significant, which is inconsistent with the picture of strong transport above a threshold that is constant in temperature gradient scale length, but consistent with the lack of stiffness seen in the unnormalized data shown in Fig. 3.4.3.

Although not shown here, the electron heat transport in these plasmas is more consistent with the hypothesis of strong transport beyond a critical gradient and warrants further investigation.
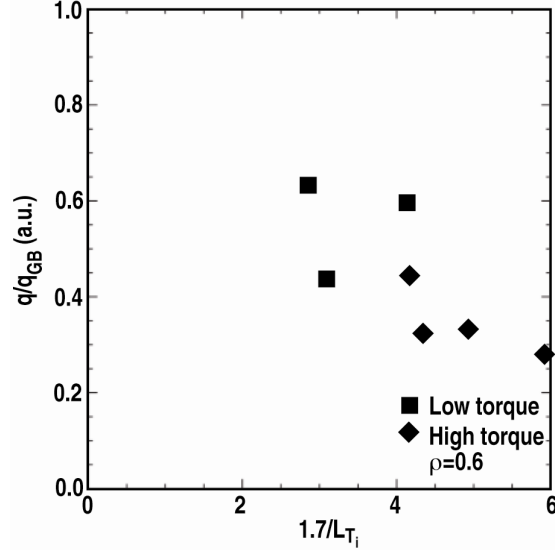
Fig. 3.4.4. The same data as Fig. 7(c) with the flux normalized to the gyro-Bohm scaling and the gradient normalized to give R/L_{Ti}.

3.E. Investigation of transport shortfall outside $\rho = 0.7$ in L-mode discharges

3.E.1. *Puzzle of Transport and Turbulence Underprediction by First Principles Simulations in the Near Edge of L-mode Tokamak Plasmas*

It has been observed that first principles turbulence/transport simulations often have good agreement with experiment in the deep core of L-mode plasmas, $\rho \sim 0.5$, but underpredict both the thermal transport and fluctuation levels towards the edge, $\rho > 0.75$ [3.10,3.12]. The agreements and, more significantly, the disagreements do not appear to depend upon the type of simulation code used (i.e. PIC or continuum solvers as reported in Ref. 3.14). Importantly, the underprediction or 'shortfall' is in the fluctuation levels (both $\tilde{n}_e$ and $\tilde{T}_e$) and in the thermal transport indicating that the discrepancy occurs at a fundamental level in the simulations. This then is the problem – why do we have reasonable agreement in the core and significant disagreement towards the edge, all for the same plasma, diagnostics, codes, and analysis techniques?

Calculations have shown that the transport underprediction moves inward in radius as the safety factor q is increased (see Fig. 3.5.1 from Ref. 3.17). A potentially related observation is that the predicted turbulent eddy tilting is larger than experimentally measured [3.18] which may be related to the magnetic shear tilting of the turbulent eddies. This latter could be a key to why the simulations underpredict the transport and might successfully be investigated with a q scan. The discharges shown in Fig. 3.5.1 were obtained in 2001 when only limited fluctuation diagnostics were available. Since then, the breadth and depth of fluctuation and turbulence diagnostics has significantly improved with the addition of advanced measurements of $\tilde{n}$ (over a very broad k range, ITG-TEM-ETG), electron temperature fluctuations, GAM and zonal flow measurements, n-T cross-phase, and magnetic fluctuations (from BES, DBS, high-k backscattering, CECE, PCI, magnetic probes, polarimetry). Profile diagnostics, n_e, T_e, T_i, and rotation, have also been significantly expanded and improved.
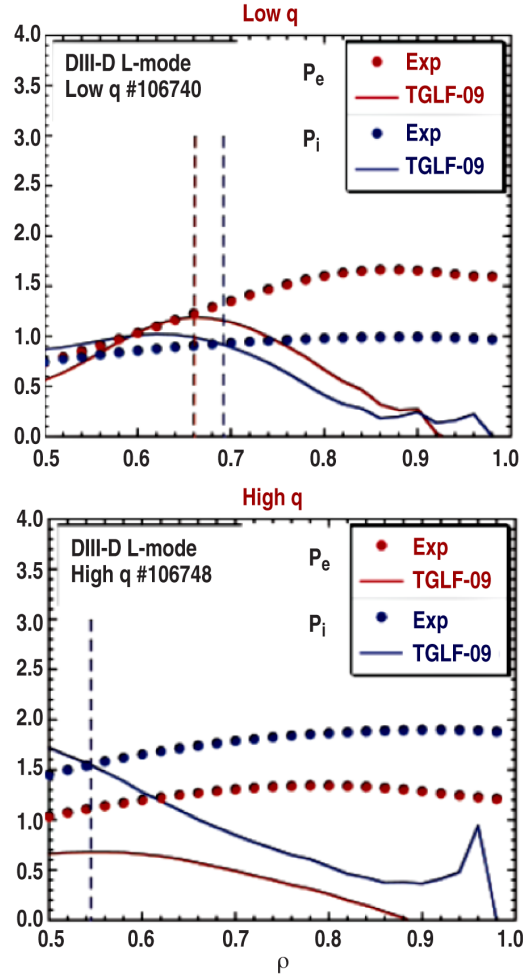
Fig. 3.5.1. Viewgraph from Ref. 3.17, showing variation of predicted transport as q is varied.

To systematically explore these simulation predictions we designed a joint, collaborative experiment (JRT 2012) that takes advantage of these advanced diagnostics as well as comparing measurements and simulations across two different tokamaks, C-Mod and DIII-D. Although these machines have very different engineering parameters (B_0, I_p, n_e, etc.) the experiments were designed so that the plasma shape and safety factors were similar.

3.E.2. *Description of Collaborative DIII-D/C-Mod Experiment*

The goal of this experiment was to test the effect of q profile and plasma current (I_p) changes on the L-mode transport underprediction found in DIII-D L-mode discharges (e.g. Refs. 3.10,3.12,3.14). We sought to capitalize on the expanded data set capabilities of DIII-D to address this question (CER, ECE, reflectometry, Thomson, BES, CECE, DBS, ECEI, n-T crossphase, PCI, etc.). MIT personnel (A. White, N. Howard, M. Greenwald, C. Rost, A. Marinoni) participated fully in the design of this experiment with A. White and N. Howard being on-site for the experiment itself.

The discharges in this experiment were designed to approximately match the shape and q_{95} values of an experiment previously performed on Alcator C-Mod and described in [3.19]. In that study, measured impurity transport was compared to linear and non-linear gyrokinetic simulations for a range of plasma current or q_{95} values. The C-Mod discharges used approximately 1.0 MW of ICRH heating at a moderate density $\left(n_e \sim 1.0 \times 10^{20}\ m^{-3}\right)$ and at a C-Mod standard field $\left(B_T \sim 5.4\ \mathrm{T}\right)$. For comparison, the DIII-D discharges used 2.2 MW neutral beam injected power, low and medium target densities of $2.2 \times 10^{19}\ \mathrm{m}^{-3}$ and $3 \times 10^{13}\ \mathrm{m}^{-3}$, and a toroidal field of 1.9 T. In our collaborative JRT experiment we obtained good overlap in the q_{95} values between the two tokamaks as seen in Table I. In addition, a good match was obtained in the plasma shapes as seen in Fig. 3.5.2. Existing GYRO analysis of the C-Mod discharges will be extended out to $\rho = 0.75$ (or further) to both investigate the presence of L-mode transport underprediction in C-Mod and to allow for direct comparison with the DIII-D discharges. The density range was chosen for optimum access for the microwave-based diagnostics.

Table I

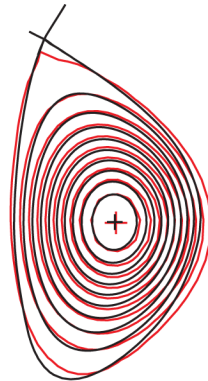| q_{95} C-Mod	q_{95} DIII-D	I_p DIII-D
3.15		
3.7	3.7	1.4 MA
5.65	5.0	1.0 MA
	6.5	0.76 MA

Fig. 3.5.2. Comparing plasma shapes: C-Mod (**red**, shot 1101014006) and DIII-D (**black**, shot 150136).

The experiment was divided into two half-day experiments, each self-contained by design. The first half-day concentrated on an engineering scan of plasma current at fixed shape and field. This varied both q_{95} and dq/dr. Early neutral beam injection was used to suppress sawteeth and provide q_0 above 1. This provided a better match of dq/dr early in the discharges, however, no attempt was made to improve this match which was the goal of the second half-day experiment. For the comparison to C-Mod we will

concentrate on the sawtoothing period of these discharges since the C-Mod results were from sawtoothing discharges. The second half-day experiment concentrated on a similarity scan of q keeping q, dq/dr, $\rho*$, $\nu*$, and β, etc. approximately fixed. This was addressed by early injection of NBI to suppress sawteeth and keep q_0 above 1. Keeping dq/dr constant as q_{95} is varied requires that q_0 increases proportionately. Achieving this while keeping n_e, T_e, T_i, Mach number, etc. approximately fixed was a significant challenge for this half-day experiment.

During the experiment J. Kinsey reported that the TGLF transport underprediction was more dominant in the electron channel compared to the ion channel. This was very different from the higher density reference shot case and quite interesting. This seemed important enough to prompt us to obtain data at a higher density for the three target q_{95} values. Overall, this gave us scans in q_{95}, density, and rotation (we had an NBI power ramp later in each plasma discharge).

The transport underprediction seen in 2001 was indeed replicated in this experiment, as can be seen in Fig. 3.5.3. Preliminary data from beam emission spectroscopy (BES) (McKee/Yan) and correlation ECE (CECE) (G. Wang) indicated that the density and electron temperature fluctuation levels increased as q increased (Fig. 3.5.4). Doppler back scattering (DBS) analysis showed that a geodesic acoustic mode (GAM) feature increased in frequency with decreasing q (consistent with a $\sqrt{T_e}$ scaling of frequency expected from GAM theory) and also expanded further inward to smaller radii (Hillesheim) (Fig. 3.5.5). In addition, a second frequency GAM appeared in the 1.4 MA case. Our attempt at decreasing the rotation using a counter beam was less successful due to an unwanted H-mode. We rapidly abandoned this attempt and instead concentrated on a co-NBI power/rotation scan. This was mostly successful in avoiding H-mode.
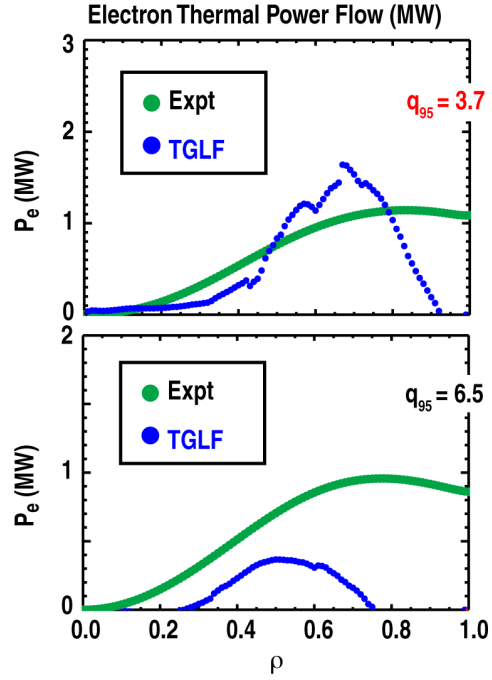
Fig. 3.5.3. Comparing electron thermal power flows from the Joint Collaborative Experiment and TGLF predictions. The shortfall is begins to occur for $\rho \sim 0.8$ for $q = 3.7$ and is significantly worse at $q = 6.5$.
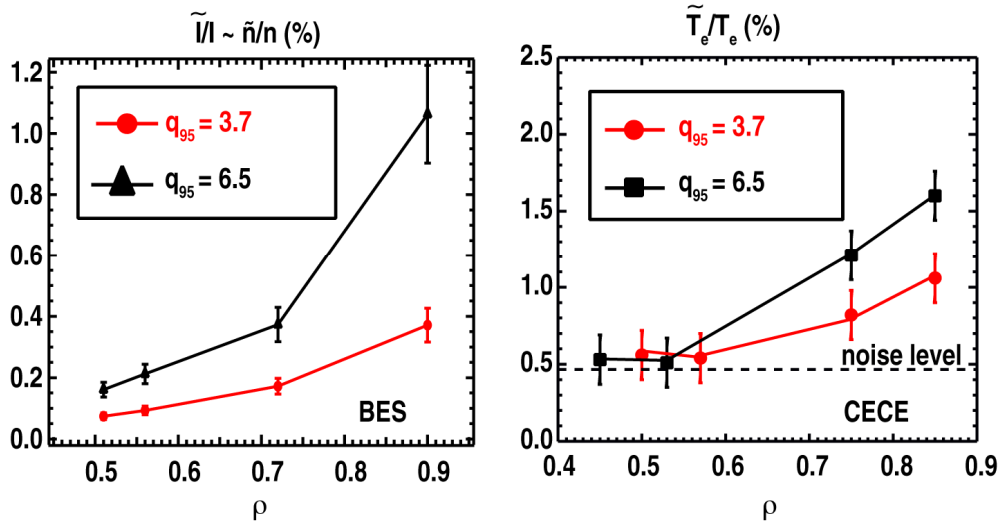

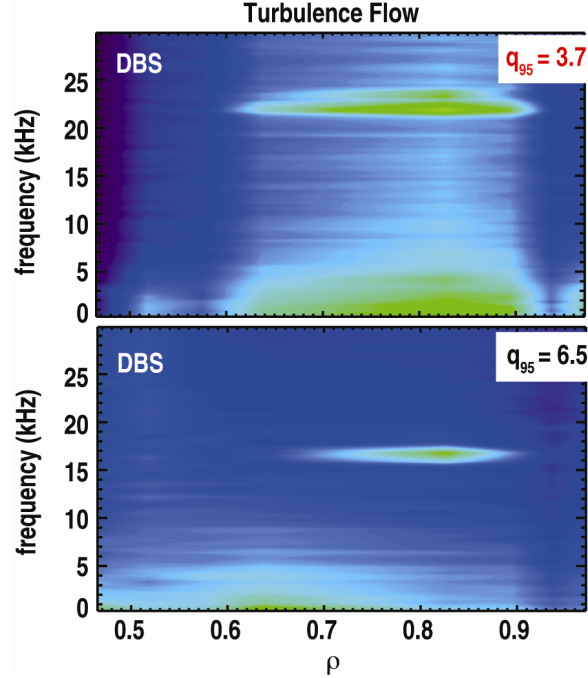Fig. 3.5.4. Radial profiles of density and temperature fluctuation levels for different q values.

Fig. 3.5.5. GAM and zonal flow behavior for different q values.

For the second half-day, we were able to make a fairly good similarity match at two different q values. Early neutral beam injection was used to keep q_0 above one in both cases. The neutral beam injected power was adjusted and density feedback used to improve the match in density, temperature, and rotation. Further analysis will be necessary to determine the level of matching however our initial estimate is that we obtained a reasonably good match. Extensive fluctuation and profile data were obtained.

3.E.3. *Analysis Plan*

We will be focusing our initial analysis efforts on the engineering I_p scan. Analysis times will be during the sawtoothing portion of the discharge to match the C-Mod sawtoothing discharges. By design, this is a close match with the work already performed on C-Mod and so makes an excellent starting point. Profile analysis, transport calculations, etc. will be performed followed by TGLF transport modeling. It is expected that C-Mod personnel will be fully involved in this analysis effort. Initial non-linear GYRO runs will then be compared to the transport and fluctuation measurements. In the meantime, C-Mod plans to extend their initial GYRO runs out to $\rho = 0.75$ or further. This will determine the amount of transport underprediction (if any) observed on C-Mod as well as provide a basis for cross-machine comparison. The next step will be a similar set of analysis and calculations focused on the dimensionally similar q scan.

3.F.   H-mode particle transport scaling with collisionality

The density profile plays an important role in the fusion performance of a tokamak. Since the fusion rate scales with n^2, a peaked profile yields more fusion power when the

57

average ion temperature is low relative to the peak in the fusion cross-section. However, a peaked density profile is often observed to lead to impurity accumulation and corresponding radiative losses and fuel dilution in the core. Therefore, in a burning plasma at higher ion temperature, a flatter density profile may be a more attractive situation. This makes the observations from a multi-machine database shown in Fig. 3.6.1 that density profiles peak at lower collisionality (the direction from present-day experiments to burning plasmas) of significant concern.

A DIII-D experiment was carried out to investigate the dependence of density peaking on collisionality directly through a controlled scan where only collisionality was varied, while the normalized gyroradius, pressure, and rotation velocity were held fixed. This requires a scan in magnetic field B where the density is constant, while current and rotation scale as B and temperature scales as B^2. Given the desire to use the reflectometer to measure the density profile, the range in B was limited to 1.65-2.15 T at the plasma center, which yields a factor of 3 change in collisionality. In addition to the density peaking, measurement of the diffusive and convective particle transport was desired. This requires perturbative techniques to separate the two types of transport. Three types of perturbations were used to probe the particle transport in addition to the intrinsic perturbations due to ELMs: fuel species gas puff, impurity (helium) gas puff, and modulation of an off-axis neutral beam. Since this experiment was just run in the 4th quarter of FY12, analysis of the perturbation data has not been carried out, and this report will focus on preliminary analysis of the density peaking.

First analysis of the profile matches in the collisionality scan indicate that good profiles matches exist for the kinetic parameters. The most striking result is that the density profiles measured by the reflectometer match quite well (see Fig. 3.6.2).

If the strong peaking trend in the database shown in Fig. 3.6.1 were a collisionality effect, it should not be possible to carry out a true collisionality scaling experiment, since the density profiles would be impossible to match. More extensive analysis is needed to verify the data and the preliminary conclusion, but it appears that the density peaking from the database analysis is likely due to another variable correlated with collisionality and not collisionality itself. One possibility is that the central fueling from neutral beams leads to the peaking (higher neutral beam heating leads to lower collisionality), but the C-Mod data would seem to preclude this. The DIII-D experiment plan included plasmas with off-axis NBI plus ECH to test this directly, but the off-axis NBI hardware was not available at that point in the experimental plan.

Future analysis of this data includes more extensive profile analysis to verify that the above profiles are typical of the DIII-D data taken and to find the best matches of all the kinetic profiles. Equilibrium and perturbation analysis will be carried out on the best-matched plasmas.
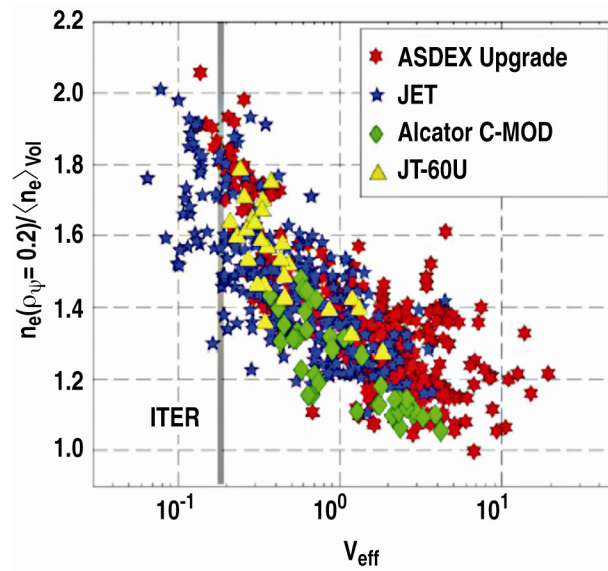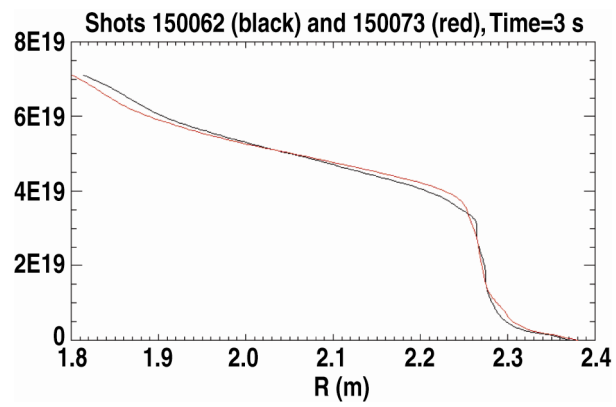
Fig. 3.6.1.

Fig. 3.6.2.

References

[3.1]   C. Holland, *et al*., Nucl. Fusion **52**, 063028 (2012).

[3.2]   J.C. DeBoo, *et al*., Phys. Plasmas **17**, 056105 (2010).

[3.3]   C. Holland, *et al*., "Validation Studies of Gyrofluid and Gyrokinetic Predictions of Transport and Turbulence Stiffness Using the DIII-D Tokamak," 24th IAEA Fusion Energy Conference, San Diego, California, EX/P7-09.

[3.4]   T.C. Luce, "Experimental Tests of Stiffness in the Electron and Ion Energy Transport in the DIII-D Tokamak," 24th IAEA Fusion Energy Conference, San Diego, California, EX/P3-18 (2012).

[3.5]   J.C. Hillesheim, *et al*., submitted to Physical Review Letters (2012).

[3.6]   S.P. Smith, "Probing Electron Temperature Critical Gradients in Experiment and Simulation," 54th Ann. Mtg. of Division of Plasma Physics, Providence, Rhode Island (2012).

[3.7]   J.C. Hillesheim, *et al*., Rev. Sci. Instrum. **83** 10E331 (2012).

[3.8]   J. Candy, *et al*., Phys. Plasmas **16**, 060704 (2009).

[3.9]   J.C. DeBoo, *et al*., Phys. Plasmas **19**, 082518 (2012).

[3.10] A.E. White, *et al*., Physics Plasmas **15**, 056116 (2008).

[3.11] J. Candy, Plasma Phys. Control. Fusion **51**, 105009 (2009).

[3.12] C. Holland, *et al*., Phys. Plasmas **16**, 052301 (2009).

[3.13] C. Holland, *et al*., Phys. Plasmas **18**, 056113 (2011).

[3.14] T.L. Rhodes, et al., Nucl. Fusion **51**, 063002 (2011).

[3.15] C. Holland, *et al*., accepted for publication in Nuclear Fusion (2012).

[3.16] G.R. McKee, "Velocity Analysis of 2D Turbulence Imaging Data from Beam Emission Spectroscopy," 54th Ann. Mtg. of Division of Plasma Physics, Providence, Rhode Island (2012).

[3.17] J. Kinsey, "Energy Transport in the DIII-D L-mode Near Edge," 25th Transport Task Force Workshop, 2012

[3.18] M.W. Shafer, *et al*., Physics Plasmas **19**, 032504 (2012).

[3.19] N.T. Howard, *et al*., Physics Plasmas **19**, 056110 (2012).

Section 4: NSTX Research

4.A. Background

The anomalous level of electron thermal transport inferred in magnetically confined configurations is one of the most challenging problems for the ultimate realization of fusion power using toroidal devices: tokamaks, spherical tori and stellarators. It is generally believed that electrostatic or electromagnetic plasma turbulence is responsible for the electron thermal transport [4.1-3]. The turbulent sources of the electron transport can be on the short-wavelength electron scale or longer wavelength ion scales. Pure modes in each regime include Electron Temperature Gradient (ETG) modes in the short-wavelength regime ($k_\theta \rho_e \leq 1$) [4.4-6], or Ion Temperature Gradient (ITG), Trapped Electron (TEM) or microtearing modes at longer wavelengths ($k_\theta \rho_i \leq 1$) [4.7-10], where k_θ is the poloidal wavenumber and ρ_e and ρ_i are the electron and ion gyro-radii. Hybrids or combinations of the above modes or cascading of power from one wavelength regime to the other may also be important. Consequently, a full picture of plasma turbulence in both the large and small wavenumber ranges is required.

While both the low and high-k turbulence has been measured in various magnetic configurations [4.11- 16], the connection between the turbulence and transport in the various channels, as well as the coupling of these channels, has yet to be established firmly. The first connection necessarily involves coupling the turbulence measurements and transport inferences to results of non- linear gyrokinetic calculations to compare both the characteristics of the turbulence and the transport levels. These comparisons have met with some, but not complete success, with agreement between turbulence characteristics and transport levels in some regions of the plasma but not others [4.9, 4.17-20]. The second connection, that being among the various transport channels simultaneously, has been studied only sparingly.

The National Spherical Torus eXperiment (NSTX) provides a unique laboratory with which to study the short-wavelength, electron-scale turbulence and its relation to electron transport. The low toroidal field of NSTX, approximately a factor of five lower than that in conventional aspect ratio devices, leads to plasma operations in parameter regimes that are different from those at higher aspect ratio and this provides new opportunities to make new diagnostic measurements and to extend and benchmark theory. The enhanced toroidicity and natural shaping at low aspect ratio is predicted to lead to reduced microturbulence levels, and thus reduced transport associated with the microturbulence. Enhanced toroidicity also results in higher trapped particle fractions, which can influence Trapped Electron Mode (TEM) turbulence and zonal flow damping. Furthermore, the low toroidal field and near Mach flow yield large values of the ExB shearing rates, believed to be important for the suppression of long wavelength microturbulence (ITG/TEM) and its associated transport. Indeed, in some typical H-mode plasmas, the ion thermal transport is on the neoclassical level [4.21], and the dominant thermal loss is through the electron channel. The χ_e values in NSTX can be in the range of 5 to 30 $\chi_{e,gyroBohm}$, which is what would be expected for ETG-driven electron transport [4.22]. Additionally, NSTX operates in regimes whose plasma collisionality is similar to that at conventional aspect ratio (and to that of ITER), but in which plasma beta, (β_{th}), and the electron and ion gyroradii (ρ_e, ρ_i respectively) can be up to a factor of 10 greater than those at higher toroidal field and aspect ratio. The high β (up to 40%) enables NSTX to explore electromagnetic and stochastic magnetic effects that may influence transport, and the large electron gyroradius (0.1 mm) allows for a direct measurement of spatially-resolved electron-scale turbulence.

It is believed that anomalous electron transport is related to short-wavelength turbulent density fluctuations, and that is with $k_\theta \rho_e \leq 1$. To investigate this, a microwave (1 mm wavelength) scattering diagnostic (high-k_r scattering system) was developed for NSTX [4.23-25]. Due to its tangential scattering scheme, this scattering system measures mostly the k_r spectrum. The system allows measurements at five scattering angles simultaneously, corresponding to a perpendicular wavenumber range of $k_\perp \approx 5 - 35$ cm^{-1} with a resolution of ~1 cm^{-1}. By using steerable optics, this high-k_r scattering system is capable of measuring density fluctuations over most of the plasma minor radius with a radial resolution of ± 2 cm.

The electron-scale turbulence measured by this high-k_r scattering system has gross characteristics and dependence on ∇Te and magnetic shear consistent with Electron Temperature Gradient modes being the source [4.26-29]. In particular, large negative magnetic shear was shown to stabilize electro-scale turbulence in experiments, consistent with ETG stability analysis [4.28-29]. Furthermore, recent work on NSTX also suggested that these modes could be affected by the large ExB shear rate exist in NSTX NBI-heated H-mode plasmas, where the magnitudes of the ExB shearing rates can exceed those of the ETG growth rates as estimated by linear gyrokinetic calculations [4.30]. More recently, the stabilization effect of density gradient on the electron-scale turbulence in quantitative agreements with linear ETG stability analysis and its correlation with a reduction in plasma thermal diffusivity [4.31] has been demonstrated. However, even under NSTX conditions, the relationship between the electron-scale turbulence and electron transport is not fully established, with agreement in certain situations but not in others [4.21, 4.31, 4.32]. This is not surprising, since limitations of the present diagnostic system, *e.g.* limited measurable $k_\perp$ range and being not able to measure the predicted spectral peak of ETG turbulence, as well as in turbulence theories and numerical codes themselves restrict the comparisons that can be made. Furthermore, other turbulence such as TEM modes and microtearing modes [4.33-36], not yet studied by the present diagnostic configuration, may also be a source of electron transport. Additionally, Global Alfvén Eigenmodes may be responsible for high levels of electron transport in regions of the plasma where the driving terms for ETG, TEM and microtearing modes (i.e., gradients in either or both the temperature and density profiles) are absent [4.37].

Measurements of the high-k turbulence spectra are complemented by measurements of the lower-k spectrum using a Beam Emission Spectroscopy (BES) diagnostic. The BES system on NSTX [4.38] consists of two optical sections, centered at r/a~0.45 and 0.85 and it has 56 sightlines, providing core to edge radial coverage. It also has four poloidal arrays.

The objective of this work is to substantially advance our understanding of plasma turbulence and its relation with anomalous transport by assessing transport in several channels simultaneously, with one channel common to all studies, for all devices, being the electrons. In NSTX, main ion particle diffusion, as well as diffusion of naturally occurring (carbon, lithium) and injected (neon) impurities, will be assessed relative to the electron thermal transport. The studies will be performed using the aforementioned turbulence diagnostics, as well as a suite of electron and ion profile diagnostics, including measurements of current profile, that will allow for determination of the various transport levels using the TRANSP analysis code. These calculations will be augmented by linear and non-linear gyrokinetic simulations using GYRO [4.39], which can be used in an attempt to understand the source of the transport, which is essential to the development of the predictive capability for future ST and non-ST devices.

63

For the 2012 Joint Research Target, the NSTX emphasis, in the absence of operation, is on analysis of pre-existing data that addresses the target goals of assessing simultaneously turbulence and transport in electrons and particles. The work is broken into three main areas:

1. H-mode collisionality scan. Several discharge sets were chosen for analysis that had a large range of collisionality and/or availability of both high- and low-k turbulence measurements. Lithium and carbon transport analysis of these discharges, in addition to electron transport, will be assessed.
2. L-mode discharges to assess the particle diffusivity in the core region where the particle source (due to beam fueling) is well known. Low-k turbulence measurements are available in the core region. What will also be studied in this dataset is the effect of ExB shear on the high- and low-k turbulence near the plasma edge, and the nonlinear interaction between the modes.
3. Neon transport in H-mode plasmas. Discharges from this experiment spanned a range of I_p and B_T, some at fixed and some at varying q. Low-k turbulence from poloidal and radial arrays are available.

4.B.   Collisionality Scan in H-mode

4.B.1   Energy transport

Early transport experiments in NSTX were carried out with wall conditioning consisting of boronization and between-shot Helium Glow Discharge cleaning. As previously reported, these "unlithiated" plasmas exhibited confinement dependences in H-mode plasmas that showed a strong, nearly linear dependence on B_T with a weaker dependence on I_p, going as $I_p^{0.4}B_T^{0.9}$ [4.21, 4.32]. When transformed to dimensionless physics variables, the NSTX confinement scaling showed a strong increase, almost inverse linearly, with decreasing collisionality [4.32]. The dependences on both the engineering and physics parameters observed in NSTX were also observed on the MAST spherical tokamak [4.40, 4.41].

More recently, NSTX has employed between-shots lithium conditioning of the vessel walls through evaporation from two "LITERs" (LIThium EvapoRators) mounted at the top of the NSTX vessel [4.42]. Discharges from these experiments will be referred to as "lithiated". Lithium conditioning has extended the lower range of accessible collisionality by approximately a factor of two, and has led improvements in energy confinement time during the H-mode, most notably in the electron channel [4.43, 4.44]. It is found that the unlithiated and lithiated discharges scale differently with engineering parameters; the lithiated discharges revealed confinement dependences on I_p and B_T that are dissimilar from the early NSTX observations, but which are similar to those in conventional aspect ratio tokamaks, as embodied in the ITER98y,2 scaling, going as $I_p^{0.86}B_T^{0}$ [4.45]. It was found that these differing dependences could be reconciled by an underlying collisionality variation, which unifies both sets of data and which exhibits a strong improvement of normalized energy confinement with decreasing ν^* [4.46].

The discharges used for this study are all H-modes based on I_p, B_T scans in both lithiated and unlithiated plasmas, and a lithium deposition scan at fixed I_p and B_T. The unlithiated discharges cover the range of I_p from 0.7 to 1.1 MA, B_T from 0.35 to 0.55 T, had deuterium neutral beam (NB) heating powers of ~ 4 MW into Lower Single Null (LSN) deuterium plasmas, elongation, κ, ~2.2 and plasma densities up to 6×10^{19} m^{-3}. All of these discharges exhibited small ELMs,

which did not affect confinement significantly. The lithiated discharges were obtained from results of several different experiments, all in the LSN configuration [4.45]. I_p and B_T scans were performed in sets of discharges for which the between-shots lithium evaporation was held to between 90 and 270 mg. These discharges covered the range I_p=0.7 to 1.3 MA, B_T=0.34 to 0.54 T, $\kappa \sim 2.3$, and had NB heating powers of approximately 3 MW. Another set of discharges was taken from a lithium evaporation scan (Li scan), covering the range from 0 to 1000 mg of lithium evaporated between shots at fixed I_p=0.8 MA, B_T=0.44 T and κ=1.8. The NB heating power in this latter set varied from 2.2 to 4.2 MW. While there were repetitive Type I ELMs at low levels of lithium, the ELMs disappeared at higher levels. Confinement and transport levels for the analysis presented here were taken during inter-ELM periods (for lower deposition values), and thus the direct effect of ELMs was removed.

The primary reason for the strong improvement in confinement time with decreasing collisionality was the broadening of the temperature profile with decreasing ν_e^*. Figure 4.1a and 4.1b show the how T_e changes with changing collisionality. Fig. 3a shows the color-coded sequence of T_e profiles themselves, plotted as a function of the square root of the normalized toroidal flux, x, while Fig. 3b is a spectrogram of the T_e profile as a function of x and ν_e^*. This data was taken from a collection of lithiated and unlithiated discharges in which dimensionless parameters other than ν_e^* were held as fixed as possible. For this series, $q_{r/a=0.5}$ = 2 to 2.5 and $<\beta>$ was between 8.5 and 12.5%. Both panels clearly show the broadening of the T_e profiles with decreasing collisionality.
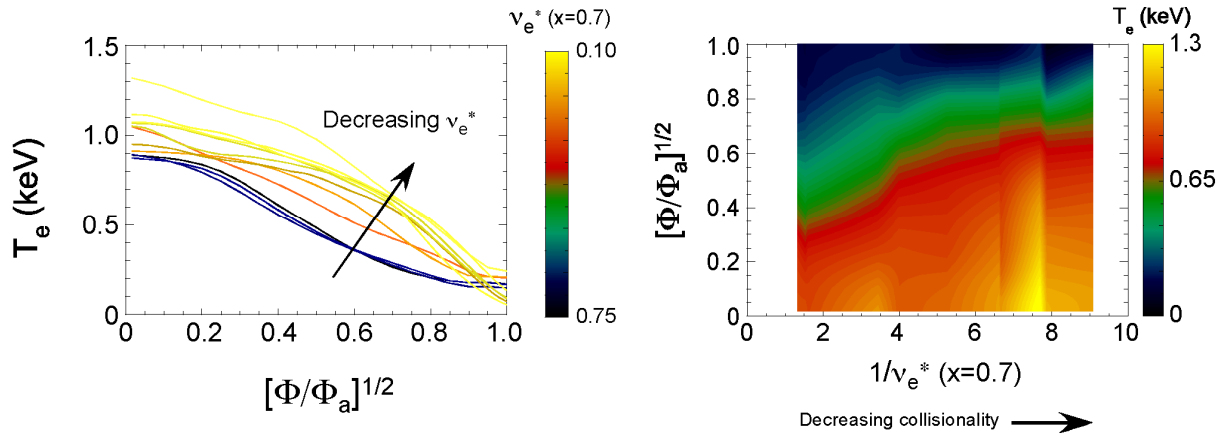

Fig. 4.1(a) T_e profiles color coded by collisionality and (b) T_e profile contour plot.

The electron temperature profile broadening reflects a progressive reduction in the electron thermal diffusivity in the outer region of the plasma as collisionality decreases. The decrease of the electron thermal diffusivity can be seen clearly in Fig. 4.2a. The curves are color-coded to be proportional to the collisionality for that discharge within the collisionality range studied. As can be seen in the figure, the electron thermal diffusivities decrease by approximately an order of magnitude over the range of collisionality at x=0.7, going from 10 m^2/s at the highest collisionality to 1 m^2/s at the lowest.

The change in electron thermal diffusivity with collisionality can also be examined in a relative sense by normalizing χ_e to $\chi_{e,gyroBohm} = \rho^{*2} c_s/a$. This normalization takes into account changes in

65

ρ^* and ion sound speed c_s due to changes in T_e to reflect the transport levels relative to what may
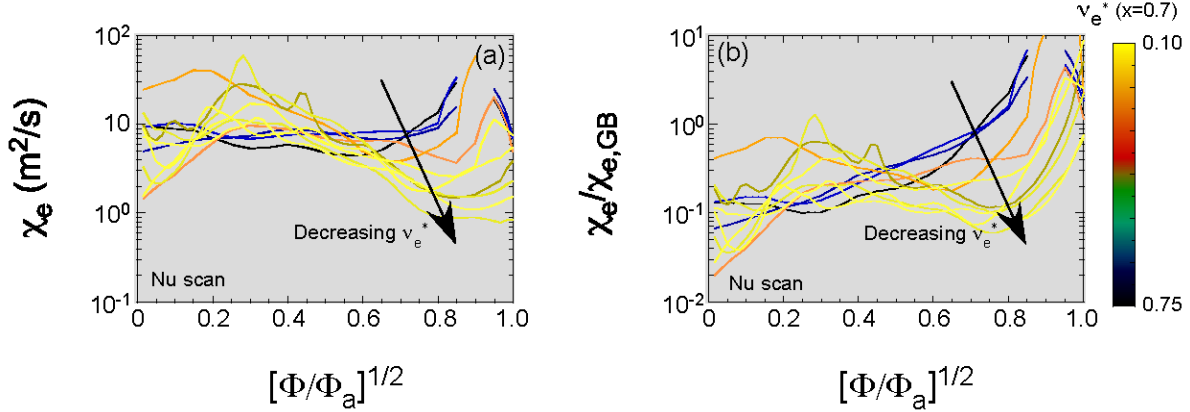

Fig. 4.2 (a) Electron thermal diffusivity profiles and (b) χ_e normalized by $\chi_{e,gyroBohm}$ in arbitrary units color coded by collisionality

be expected by gyroBohm transport. The profiles of $\chi_e/\chi_{e,gyroBohm}$ are shown in Fig. 4.2b in arbitrary units, and similar to the trend observed for χ_e alone, the normalized transport also decreases approximately an order of magnitude.

Ion transport behaves differently from that of electrons. Fig. 4.3a shows the ion thermal diffusivity normalized by the neoclassical ion thermal diffusivity as computed by NCLASS for both scans at x=0.60. This particular radius was chosen for this comparison to avoid regions of sharp gradients in the ion temperature that existed farther out. While there is clearly scatter in the data, $\chi_i/\chi_{i,neo}$ increases approximately a factor of five to ten going from high to low collisionality, a trend that is reversed from that of the electron transport. At the highest collisionality, $\chi_i/\chi_{i,neo} \sim$ 0.5, which we take to be at a neoclassical level when the differences among neoclassical theories and the uncertainty in χ_i are taken into account. As collisionality decreases, the ions become more anomalous, reaching a factor f four to five.

Coupled to this increase in relative ion transport at low collisionality are the trends that both the local toroidal flow velocity increases and toroidal flow shear decreases as collisionality decreases. This is due to a relative broadening in the toroidal flow velocity profiles at this location as collisionality decreases. Fig. 4.3b shows the relation between the normalized ion transport and the flow shear, as characterized by the normalized gradient of the toroidal Mach number M_s. As can be seen, as the flow shear tends toward zero, the normalized ion transport increases; this occurs at low collisionality. This trend may reflect the role of flow shear

Local linear stability calculations have been run for several series of discharges. The gyrokinetic code GYRO is utilized as it can include all appropriate physical effects: general geometry magnetic equilibrium reconstructions, multiple kinetic species (typically deuterium, carbon, and electrons), finite collisionality, and complete magnetic perturbations (shear and compressional).
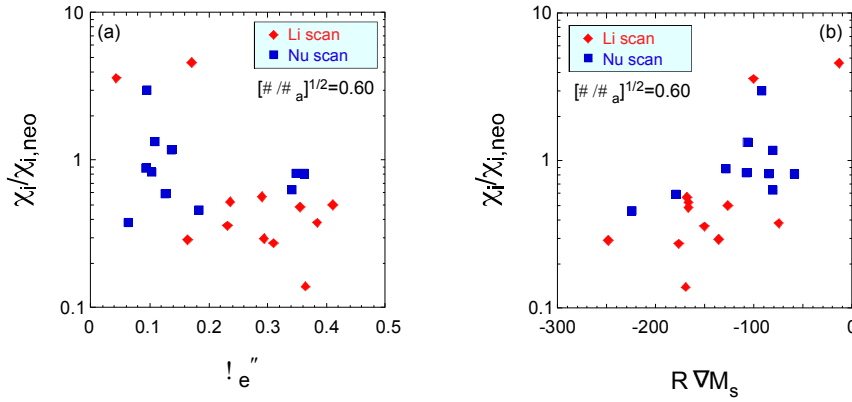
Fig. 4.3 Ion thermal diffusivity normalized to that from NCLASS neoclassical as a function of (a) collisionality and (b) toroidal flow shear at x=0.6

Finite flow and global effects are ignored for linear simulations but will be included in nonlinear simulations as necessary.

The linear calculations reveal a complicated mixture of dominant modes, depending on both radius and collisionality. Several collisionality scans were used for this analysis, one in which plasma current and toroidal field were both varied at constant q and constant lithium deposition, and one in which the amount of between-shot lithium deposition increased continuously across a range of discharges (reduced collisionality with increased lithium deposition). Results here will be shown only for both scans.
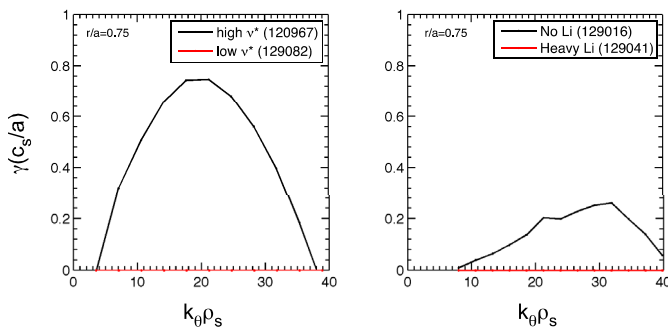
Fig. 4.4 Normalized ETG growth rates at r/a=0.75 at the extreme collisionalities for two collisionality scans. ETG is unstable at the highest collisionality in both scans, but completely stable at the lowest.
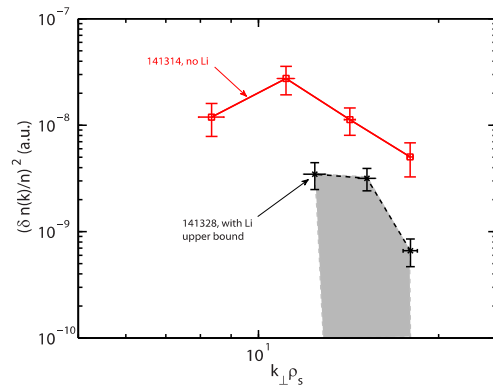
Fig. 4.5 Normalized high-k fluctuation amplitudes as a function of normalized radial wavenumber for discharges with no lithium (high collisionality) and heavy lithium (low collisionality) between-shot evaporation. The "with Li" discharge fluctuation amplitudes are upper limits.

At high-k, in the electron gyroradius-scale regime, the growth rate of Electron Temperature Gradient (ETG) modes is found to decrease with decreasing collisionality, becoming completely stable at the lowest ν_e^*. This result is shown in Fig. 4.4, which uses the highest and lowest collisionality cases from the two scans mentioned above. As can be seen for both scans, the ETG

growth rate at r/a=0.75 peaks in the $k_q r_s$=20 to 30 range at the highest collisionality (black curve), but is completely stabilized at the lowest (red curve). This is consistent with comparisons of the measured electron temperature gradient to the critical gradient for ETG [4.47] which shows approximately a factor of five reduction with decreasing collisionality in the region from r/a=0.7-0.8. to <1, indicating stability of ETG modes.

These results are consistent with observations of high-k turbulence from the microwave scattering diagnostic. k-spectra for discharges with no lithium (high collisionality) and heavy lithium (low collisionality) evaporation are shown in Fig. 4.5. Note that these discharges are not part of the same scan for which the gyrokinetic calculations were performed. The normalized fluctuation amplitudes are approximately one order of magnitude (or more) lower at low than at high collisionality. The causality of this result, relative to the improvement in electron transport and change in the T_e profile, has not yet been determined.
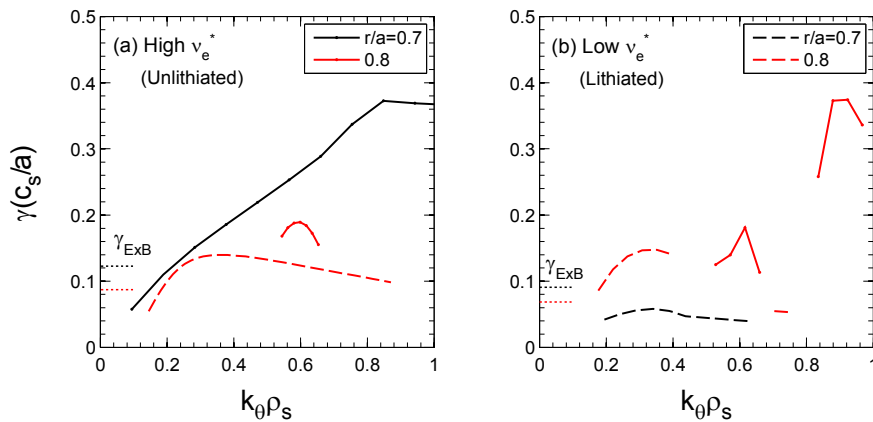

Fig. 4.6 Normalized growth rates of low-k modes from linear GYRO runs for (a) high and (b) low collisionality cases in the Nu scan. The solid lines represent microtearing modes while the dashed lines represent the hybrid TEM/KBM mode. The normalized ExB shearing rates for each radius are given by the color-coded horizontal dashed lines on the left of each plot.

The results of linear gyrokinetic calculations for low wavenumbers in representative low (lithiated) and high (unlithiated) collisionality discharges from the first scan shown in Fig. 4.5 is shown in Figs. 4.6a and 4.6b. The results for r/a=0.7, 0.8 (x=0.6, 0.7) are shown. Previous analysis results for unlithiated discharges alone have shown that microtearing modes were an important component of the electron transport at these wavenumbers, and the decrease in electron transport going from high to low collisionality was associated with the stabilization of the microtearing modes [4.34-37]. The results in both collisionality scans support this conclusion, and broadens it by considering the variation of collisionality across the lithiated discharges (results from only one scan will be shown). Fig. 4.6a and 4.6b shows that the microtearing modes (solid lines) are strong and dominant, and much greater than the normalized ExB shearing rate, at the high collisionality at r/a=0.7, but they are completely suppressed at r/a=0.7, however, at the lowest ν_e^*. Some residual microtearing remains at r/a=0.8. On the other hand, the unstable region of the ion modes (dashed curves), actually expands in radius going from high to low collisionality, although both at r/a=0.7 and 0.8, the normalized growth rates are comparable to the normalized ExB shearing rates.

Non-linear simulations will be run to assess the expected level of electron and ion transport from this mixture of modes. Also, analysis of both carbon and lithium impurity transport are underway for these discharges to assess the relation between the particle and energy transport.

4.B.2 Impurity transport

The transport of carbon and lithium are determined with respect to predicted neoclassical transport of these impurities. Departures between measured (measured on the low field side) and predicted profiles are possible indications of anomalous (i.e., turbulence-driven) processes. The tools used for the impurity transport calculations include MIST [4.48], NCLASS [4.49] and NEO [4.50], the latter two describing local and non-local neoclassical transport respectively. The approach taken is summarized below:

Interpretive/predictive MIST runs
Experimental carbon and lithium data [4.51, 4.52] are used in an interpretive/predictive hybrid modeling approach. Experimental profiles are first input into NCLASS (or NEO) to determine the neoclassical particle diffusivity, D. Then, the particle convective velocity, v, is adjusted for both carbon and lithium to arrive at the best match between predicted carbon and lithium profiles (using the D and v combinations) and the time evolution of the experimental impurity profiles.. The source, which is taken to be a point source at the very plasma edge, is adjusted to match the absolute value of the experimental impurity density for carbon. This approach was chosen due to the large number of degrees of freedom. Estimates of the v/D and experimental density profile peaking factors are the metrics used for comparison. It must be noted that the temporal waveform of the impurity source will affect the D and v profiles that are adjusted to match the experimental profiles for time periods that are not in steady state. Here a singly ionized carbon source at the separatrix is assumed, increasing until the H-mode transition and then constant throughout the rest of the discharge. Once a good fit is obtained, then the experimental or interpretive v/D ratio can also be used in the source-free region. An assumption used here is that D and v are taken to be the same for all impurity ionization stages.

Fully predictive MIST runs
Time-dependent neoclassical values for both D and v are determined from NCLASS, and are used as input for fully predictive MIST calculations. MIST is then used to derive the full neoclassical prediction of the impurity charges states.

Experimental Peaking
In steady state and, in the source free region, the experimental peaking $1/L_{nC}$ is equal to the ratio of the experimental convective velocity and the diffusion coefficient (v/D). In this way, the experimental levels of impurity transport and predictions from neoclassical codes can be compared.

The v/D ratios derived in these three ways are then compared for the various discharges for both carbon and for lithium for a range of collisionality in representative discharges from a high-β collisionality scan discussed in the preceding section. The differences in impurity transport regimes, collisionality, inventories, profile shapes and experimental peaking factors will be analyzed for C and Li, and the experimental values of peaking factors vs those computed from neoclassical theory using NCLASS and NEO will be compared.

The impurity profiles (Li and C) do not show any large, obvious differences. The carbon profiles in a low (left panel) and a high (right panel) collisionality discharge are shown in Fig. 4.7. The carbon profile in both discharges are, as typical, hollow just after the H mode transition and then slowly fills into the core region. Lithium profiles for these discharges have large error bars and thus are not shown in this figure.
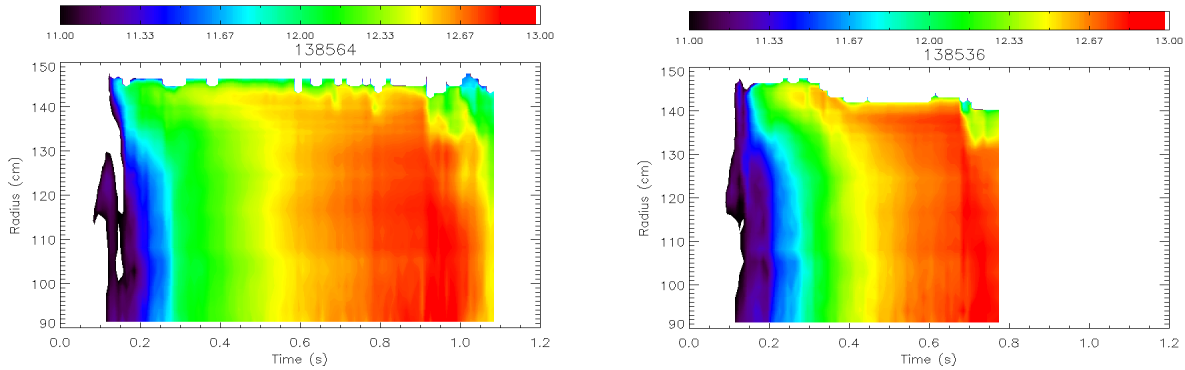

Fig. 4.7 Carbon profile evolution for a low (left panel) and high (right panel) collisionality discharge.

The evolved profiles, taken at t=0.405 s, are shown in Fig. 4.8. The curve in blue is from the low collisionality discharge, while the one in black is at high collisionality (the red curve is at intermediate collisionality). It can be seen that the carbon density profile (top panel) exhibits peaking slightly farther in at high collisionality than at the lower collisionalities, in addition to having higher accumulation. It is difficult to draw conclusions from the lithium profiles because of the large measurement error bars. As the discharges evolve further, to 0.605 s, the outboard carbon peaking for the high collisionality discharge remains, while the profiles are flat (no outboard peaking) at lower collisionality (Fig. 4.9)
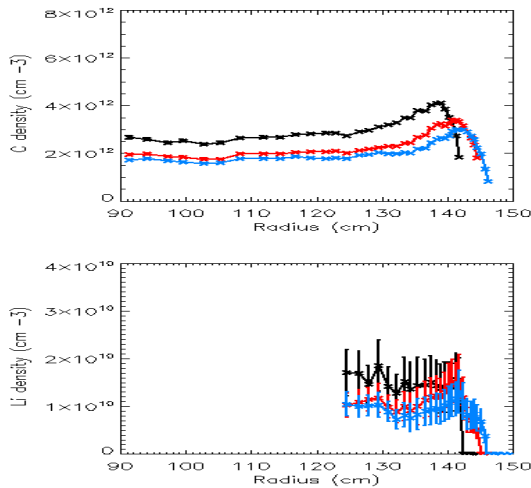

Fig. 4.8 Carbon (top panel and lithium (bottom panel) profiles at t=0.405 s for high (black curve), intermediate (red curve) and low (blue curve) collisionality discharges.
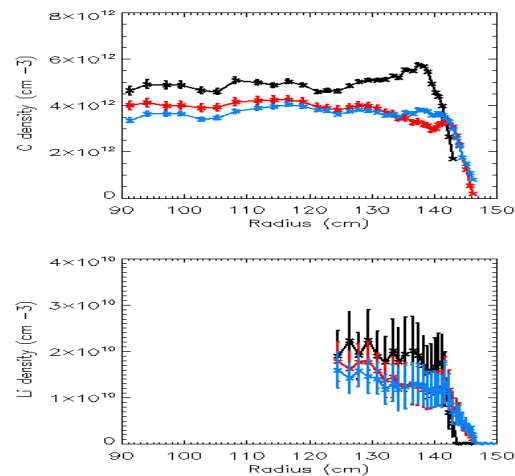
Fig. 4.9 Similar to Fig. 8 but at 0.605 s

The deuterium and impurity collisionalities are shown in Fig 4.10 for the high collisionality (left column) and low collisionality (right panel) discharges at t=0.405 s (top row) and t=0.605 s (bottom row). The collisionalities for the respective ion species at both collisionalities and times are very similar, and they indicate that the carbon and lithium are in the banana-plateau regime in the core of the plasma, indicating the neoclassical fluxes are driven by gradients in the plasma profiles, while the collisionalities become >1 farther out (r/a>~0.7), indicating the neoclassical fluxes are driven by collisions.
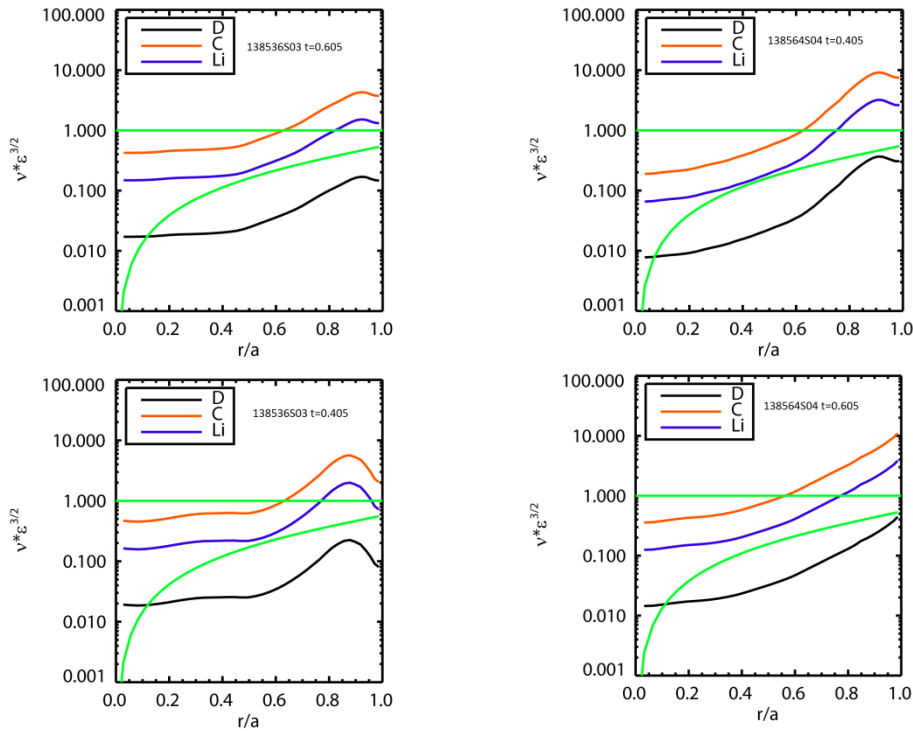
Fig 4.10 Ion species collisionality profiles at t=0.405 s (top row) and t=0.605 s (bottom row) for the high collisionality discharge (left column) and low collisionality discharge (right panel).

The results of the hybrid and predictive MIST calculations are for the high collisionality discharge are shown in Fig. 4.11, where the experimental carbon density profile at various times is compared to those calculated by the two methods. In the hybrid calculation (labeled "Interpretive (MIST)"), D is determined from neoclassical theory and the particle convection velocity v is determined from the best fit between the measured and calculated carbon density profiles. In the predictive calculation, both D and v are calculated from neoclassical theory. It is clear from Fig. 4.11 that there is much better agreement in the hybrid calculation, where the measured and calculated profiles (solid and dashed curves respectively in the right column of Fig. 4.11) show much better agreement than the profiles determined in the fully predictive calculation. The comparison in the predictive case indicates outboard peaking at later times farther inward for the prediction than for the measurement. In addition, peaking is predicted in the very core of the plasma, especially at later times; this core peaking is not seen in the measured profiles. The results suggest that processes, such as turbulent transport, may be important; neoclassical transport alone cannot explain the carbon density profile evolution.
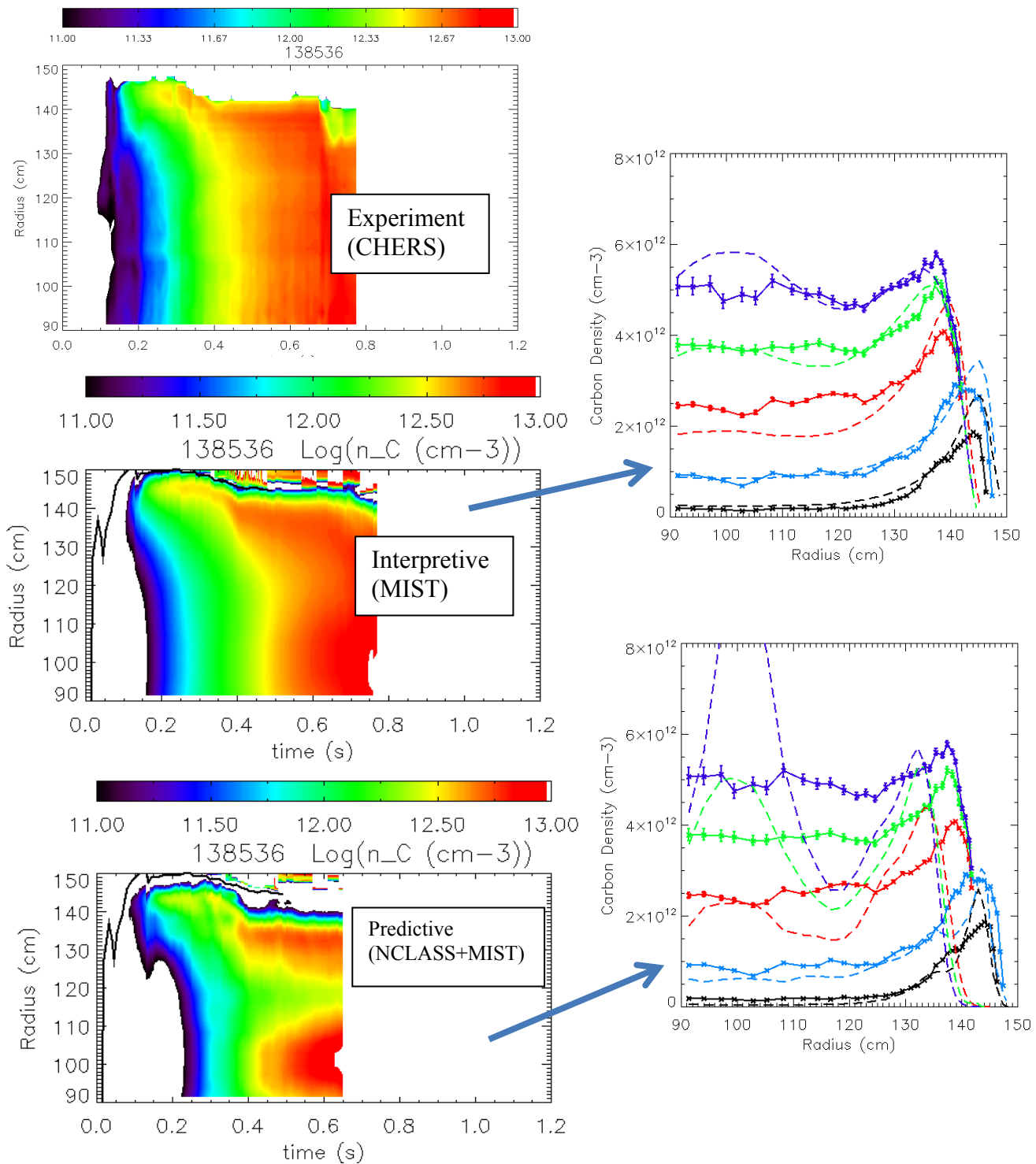
Fig. 4.11 (Left column) Evolution of the carbon density profile vs time and radius for the experimental measurement (top panel), Hybrid MIST calculation (middle panel) and predictive MIST calculation (bottom panel) for the high collisionality discharge. The direct comparisons between the respective MIST calculations (dashed lines) and experimental profiles (solid curves) are shown at increasing times in the Right column. Curves are plotted for t=0.2 to 0.6 s in increments of 0.1 s

A similar comparison was made for the low collisionality discharge, and this is shown in Fig. 4.12. The results are similar to those shown in Fig. 4.11; neoclassical transport alone is insufficient to describe the transport necessary for agreement between measured and predicted carbon density profiles.
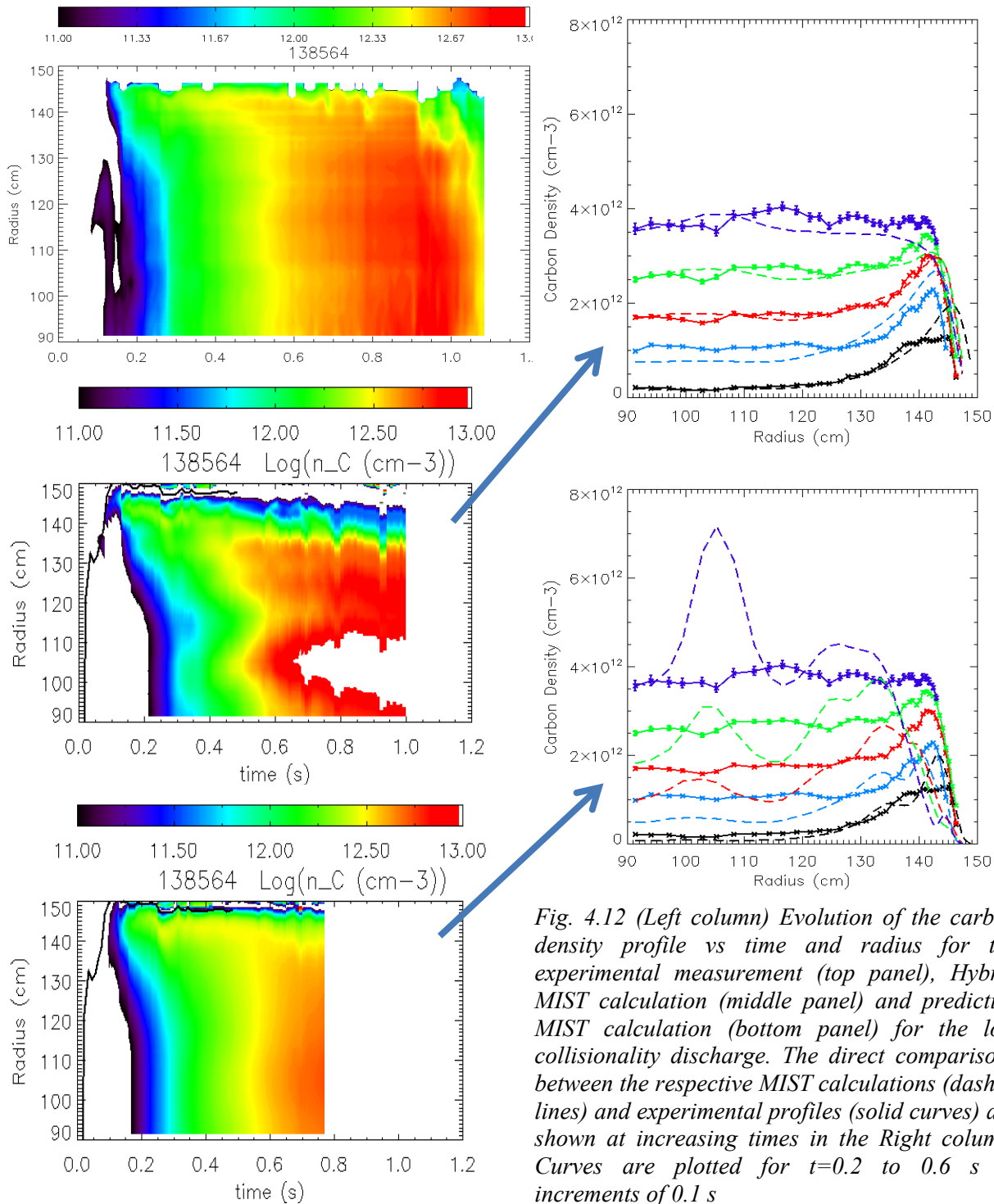

Fig. 4.12 (Left column) Evolution of the carbon density profile vs time and radius for the experimental measurement (top panel), Hybrid MIST calculation (middle panel) and predictive MIST calculation (bottom panel) for the low collisionality discharge. The direct comparisons between the respective MIST calculations (dashed lines) and experimental profiles (solid curves) are shown at increasing times in the Right column. Curves are plotted for t=0.2 to 0.6 s in increments of 0.1 s

73

The peaking factors for both discharges, as determined by both measurement and analysis/prediction, is shown in Fig. 4.13. The figure shows these factors for the high (left column and low (right column) collisionality discharges for t=0.405 s (top row) and t=0.605 s (bottom row). For both collisionalities and both times, the experimental peaking (red curve) is clearly greater than that from the hybrid MIST calculation ("Interpretive") and especially for the full neoclassical prediction ("NCLASS"). In fact, the latter, as seen in Figs. 4.11 and 12, exhibits a large inward pinch both in the inner and outer regions of the plasma, accounting for strong peaking in those locations (which are different than those seen from experiment).
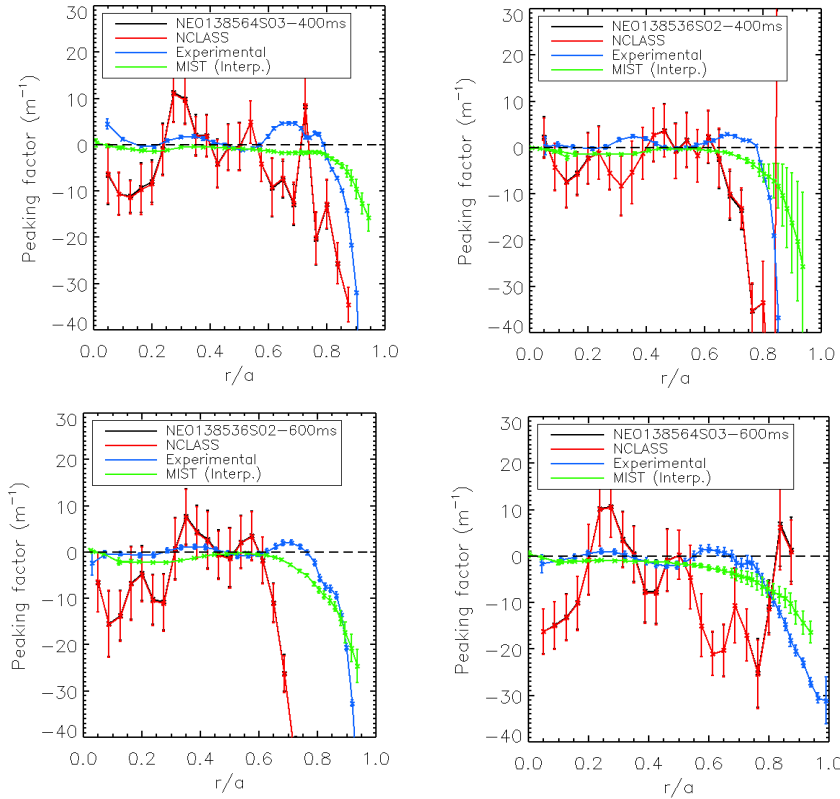
Fig. 4.13 Carbon density profile peaking factors for high (left column) and low (right column) collisionality discharges at t=0.405 s (top row) and t=0.605 s (bottom row).

To briefly summarize this section, it is seen that collisionality has a strong influence on the electron and ion energy transport, with a strong decrease in electron transport, especially in the outer portion of the plasma, with decreasing collisionality. Linear gyrokinetic calculations indicate that this decrease is due to a complete stabilization of high-k ETG modes and a suppression of the range and growth rate of low-k microtearing modes as collisionality is reduced. Ion transport with respect to neoclassical estimates actually increases going to lower collisionality, with neoclassical transport at the high collisionality but several times greater than neoclassical at the lowest collisionality. Low-k ion modes are predicted to become more widespread and stronger as collisionality decreases. This trend may, in fact, also be due to decreasing rotation (and ExB) shear as collisionality is reduced, instead of collisionality itself, and future experiments in NSTX-U will help resolve this uncertainty. Particle transport, as gauged from impurity transport, does not show the strong dependence on collisionality that is seen in the thermal ion species. Hybrid and predictive calculations indicate that neoclassical

transport alone cannot account for the characteristic peaking near the edge of the plasma of the measured carbon density profile as the discharges evolve temporally; purely neoclassical transport would predict outer region peaking farther in than is measured, and an additional strong peaking in the very core. Consequently, some some turbulent process may be important.

4.C. L-Mode

4.C.1 Energy Transport: Effect of ExB Shear on High-k Fluctuations/Turbulence Characteristics

An important tool for controlling microturbulence in toroidal magnetic confinement devices is the equilibrium ExB shear generated by externally driven (or intrinsically generated) plasma flow [4.53]. It was pointed out that ExB shear affects microturbulence and associated turbulent transport both linearly and nonlinearly: change mode stability, e.g. enhance damping by coupling to stable modes; change the relative phase between fluctuation quantities, e.g. density fluctuation and radial velocity fluctuations; reduce fluctuation amplitude. The most physical way to determine the effect of ExB shear on turbulence is to compare ExB shearing rate, $\omega_{E\times B}$, with turbulence decorrelation rate as pointed out in [4.54]. However, the turbulence decorrelation rate is usually unknown, and a rule of thumb is that turbulence is significantly stabilized by ExB shear when the Hahm-Burrell ExB shearing rate [4.54], $\omega_{E\times B,HB}$, is larger than the maximum linear growth rate of a particular instability, γ_{max} [4.53]. A quantitative numerical study of ExB shear effects on turbulence and transport was reported in [4.55], where extensive linear and nonlinear gyrokinetic simulations were used to determine the amount of ExB shearing rate needed for quenching a specific kind of plasma turbulence. In particular, the ion-scale turbulence (ITG/TEM) and the associated turbulent transport is found to be quenched if $\omega_{E\times B,WM}/\gamma_{max} \approx 1.41(A/3)^{0.6}/(\kappa/1.5)$, where $\omega_{E\times B,WM}$ is the Waltz-Miller ExB shearing rate [4.56], γ_{max} is the maximum linear growth rate for a particular instability, A is the aspect ratio and κ is the elongation. Indeed, experiments have shown that increase in ExB shear is correlated with the formation of H-mode edge transport and internal barriers and reduction in ion-scale turbulence [4.57, 4.26]. However, we note that in these cases, the ExB shear mainly comes from pressure gradient rather than from plasma rotation. On the other hand, spherical tokamaks (STs) with tangential neutral beam heating typically have strong toroidal flow with Mach number approaching 1, and ExB shear can be dominated by the contribution from plasma rotation. Thus ion-scale turbulence is expected to be stabilized by ExB shear, which is supported by the observed neoclassical level of ion thermal transport in STs [4.32, 4.58]. Furthermore, ExB shear was also shown to suppress electron-scale turbulence when the ExB shearing rate is comparable to the maximum ETG linear growth rate [4.30], where the turbulence spectrum was measured by a high-k scattering system [4.25] on the National Spherical Torus eXperiment (NSTX) [4.59]. However, the change in spectral shape was not explored in Ref. [4.30] since only a single k measurement was available due to limitations in the scattering scheme and most importantly correlation with transport was not investigated.

Here, with much improved scattering schemes of this high-k scattering system, we present the first experimental observation of a progressive change in electron-scale turbulence k spectrum and thermal confinement at the core-edge transition region of a set of NSTX NBI-heated L-mode plasmas (r/a~0.66-0.78), as the ExB shearing rate is continuously increased due to plasma toroidal velocity increase from Neutral Beam Injection (NBI). We observed that as the ExB shearing rate is continuously increased, the ratio between the ExB shearing rate and the aximum

ITG mode growth rate continuously increases and the maximum power of the measured electron-scale turbulence wavenumber spectra decreases. Meanwhile, both the electron and ion thermal transports are also reduced as long as MHD activities are not important. These observations are consistent with that some of the observed electron-scale turbulence is nonlinearly driven by ITG turbulence and its power decreases as ITG turbulence is progressively suppressed by ExB shear.

Observations on continuous ExB shear ramping-up were made in a set of center-stack limited and NBI-heated L-mode plasmas. These plasmas have a toroidal field of 5.5 kG, a plasma current of 900 kA and a two-phase NBI with the first 2 MW NBI pulse from about 100 ms to 200 ms and the second 2 MW NBI pulse from about 350 ms to the end of discharges. During the second phase of NBI, plasma continuously spins up, which leads to a simultaneous increase in the ExB shearing rate in the outer half of the plasma ($r/a \gtrsim 0.5$). Here in this paper, we present the observations from shot 141716 for which we have done extensive analysis. In this shot, the second 2 MW NBI pulse is re-injected from 335 ms after a first injection from 90 ms to 230 ms. With the presence of the 2 MW NBI pulses, ion temperature and plasma toroidal velocity are measured with a charge exchange recombination spectroscopy (CHERS) diagnostic [4.60] and magnetic field pitch angle is measured by a Motional Stark Effect (MSE) diagnostic [4.61]. Electron temperature and density are measured with Multi-point Thomson Scattering (MPTS) [4.62]. Plasma equilibrium is obtained using LRDFIT (LR circuit model with Data FITting capabilities) equilibrium reconstructions constrained by magnetic pitch angle measurements from the MSE diagnostic [4.58] and electron temperature iso-surfaces.
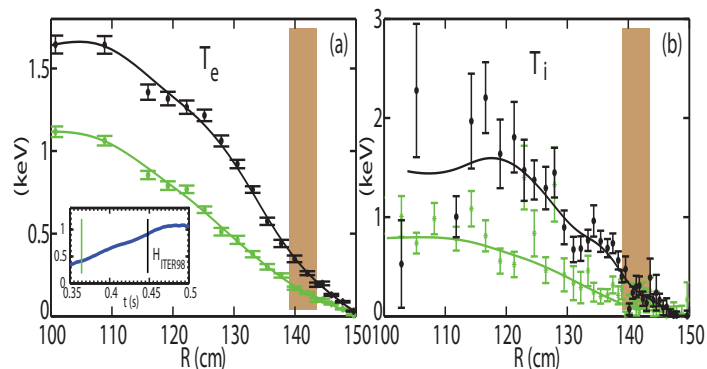

Figure 4.14 (a) Radial profiles of electron temperature at t=364 and 448 ms. (b) Radial profiles of ion temperature at t=364 and 448 ms. The shaded regions in both panels denote the measuring of the high-k scattering system. Note that the insert in (a) shows the time trace of H_{ITER98} and the two vertical lines denotes the time points used for (a) and (b).

The electron and ion temperature, T_e and T_i, radial profiles are plotted in Fig. 4.14(a) and (b) at t=364 ms and at t=448 ms (corresponding to two exact MPTS time points). The high-k measurement region, the overall radial region covered by all channels with the center of scattering location separated by $\lesssim 1$ cm, is denoted by the shaded region in the figure from about R=139 to 144 cm ($r/a \sim 0.66$-0.78). The H_{ITER98} time trace shown in an insert in Fig. 4.14(a) shows about a factor of 2 increase in H_{ITER98} from t=350 ms to 500 and we note that this increase is coincident with the increase of plasma toroidal flow velocity shown in Fig. 4.15. We can see that both the maximum T_e and T_i increase by 50-100% as H_{ITER98} (and toroidal flow velocity) increases, and both T_e and T_i gradients also increase in the high-k measurement region. On the other hand, we would like to point out that the gradient scale lengths remain relatively constant. We note that although the energy confinement of this L-mode plasma reaches that of the H-mode plasmas in conventional tokamaks, no formation of an energy transport barrier has been observed, and as we will show later, thermal transport is reduced significantly in the outer half of the plasmas which is consistent with the increased ExB shear there.
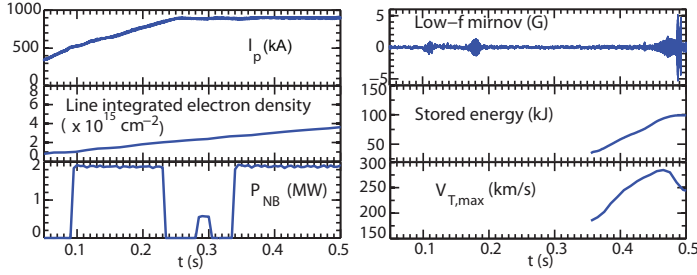
Figure 4.15 An overview of shot 141716 with time traces of plasma current, linear integrated electron density, neutral beam power P_{NB}, low-f magnetic fluctuation, stored energy and maximum plasma toroidal flow velocity.

The upper panels Fig. 4.16 show the spectrograms of the scattered signals from t=350 ms to 500 ms (during which the plasma is spinning up), where the two exact MPTS time points, i.e. t=364 and 448 ms, are denoted by two colored lines in each panel. The lower panels show the frequency spectra at the above two time points for each of the four high-k channels. The wavenumbers measured by the four channels correspond to $k_\perp \rho_s$ of 8-10, 6-8, 4-6 and 2-4 from channel 1 to 4 at t=364 ms. At t=448 ms, because of the increase in T_e and density gradient, ρ_s and the wavenumber measured by each channel become larger, corresponding to $k_\perp \rho_s$ of 13-15, 10-12, 7-9 and 4-6 from channel 1 to 4 respectively. For each channel, the signal from collective scattering of microwave by electron density fluctuations manifests as a spectral peak at negative frequencies, which corresponds to wave propagation in the ion diamagnetic drift direction in the laboratory frame (Lab frame).

Figure 4.16 Upper panels: The spectrograms of four high-k channels during the second NBI phase; Lower panels: The frequency spectra at the two exact MPTS time points (the same as in Fig. 2) for four high-k channels. The two colored lines in the upper panels denote time points used for plotting the lower panels with the same color coding and the vertical lines in the

lower panels denote the Doppler frequencies, $f_{Doppler}=k_T V_T/2\frac{1}{4}$, for different channels at t=364 ms (Note that for clarity, only $f_{Doppler}$ at t=448 ms is not shown). The electron direction is on the ride hand side of the vertical lines in the lower panels, as shown for channel 2.
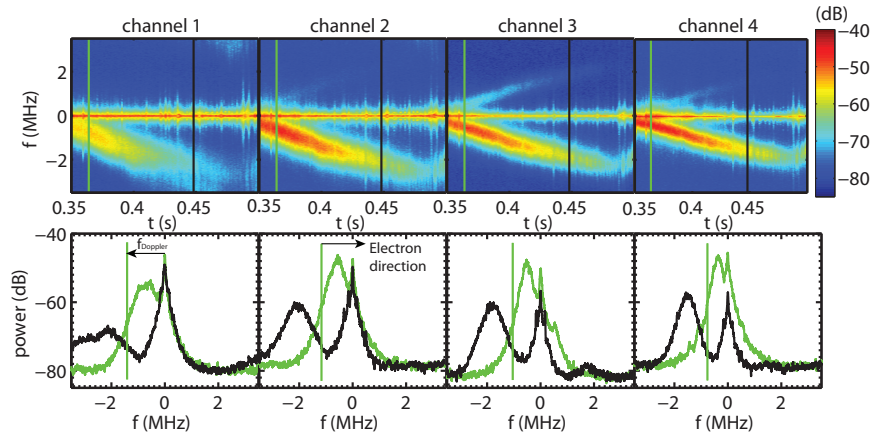
However, each channel has a Doppler frequency shift [$f_{Doppler}=k_T V_T/2^{\frac{1}{4}}$, k_T is the toroidal wavenumber from ray tracing and V_T is the plasma toroidal flow velocity from CHERS measurement] denoted by vertical lines in the lower panels of Fig. 4.3. After subtracting the Doppler shift, channels 1, 2, 3 and 4 show that the wave propagating direction is in the electron diamagnetic direction which is on the right hand side of the vertical lines (For clarity, only $f_{Doppler}$ at t=364 ms is shown but conclusion is the same for t=448 ms), and the propagation direction is in the electron direction. We also note that the large symmetric central peaks at f=0 are due to the spurious reflections of the probing microwave beam. Large frequency separation of the scattering signals from the central peaks ensures accurate measurements of scattered microwave

power. From Fig. 4.16, it can be immediately seen that the measured fluctuations in all channels show continuous increase in Lab-frame fluctuation frequency, consistent with a Doppler shift frequency resulting from plasma spinning-up. Furthermore, it is also clear that the fluctuation intensity denoted by color in the spectrograms shows gradual decrease as the Lab-frame fluctuation frequency increases (a more quantitative evaluation of the decrease can be seen in the lower panels).

Only radial data exists for the BES measurements of low-k turbulence for these discharges, so the determination of poloidal correlation lengths is not possible. The radial data show little change in frequency spectra over the time range of interest in these shots, however.

To model ExB shear effect on microturbulence, nonlinear gyrokinetic simulations are needed. However, here we use linear stability analysis to provide some initial assessment of the ExB shear effect in the experiment, motivated by the studies on ExB shearing rate and linear growth rate reported in [4.54-55].

In Fig. 4.17(a), $\omega_{E\times B}/\gamma_{max}$ averaged in the high-k measurement region is plotted as a function of time (Note that both $\omega_{E\times B,HB}$ and $\omega_{E\times B,WM}$ are used and they differ by about a factor of 5), and γ_{max} is the maximum linear growth rate for the most unstable ion-scale instability (ITG modes) calculated with the GS2 code [4.64]. We note that the gradual increase of $\omega_{E\times B}/\gamma_{max}$ from t=364 to 448 ms is due to the increase of $\omega_{E\times B}$, while the faster
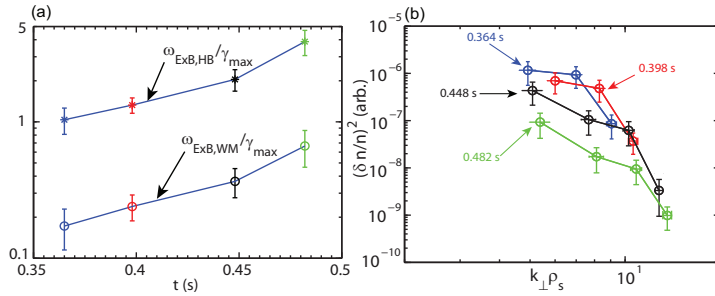

Figure 4.17 (a) The ratio between the ExB shear rate and the maximum linear growth rate for ITG instability (both the Hahm-Burrell ($\omega_{E\times B,HB}$) and Waltz-Miller ($\omega_{E\times B,WM}$) ExB shearing rates are shown); (b) $k_\perp$ spectra in arbitrary unit at the 4 time points shown in (a.)

increase of $\omega_{E\times B}/\gamma_{max}$ after t= 448 ms is due to both the increase of $\omega_{E\times B}$ and decrease of γ_{max}. Figure 4.17(b) shows the measured $k_\perp$ spectra at time points used in Fig. 4.16(a). From t=364 to 398 ms, the measured maximum spectral power (at $k_\perp\rho_s \approx 5$) decreases by about 40% while $\omega_{E\times B,WM}/\gamma_{max}$ increases from about 0.17 to 0.24. Meanwhile, the spectral power at larger wavenumbers ($k_\perp\rho_s \gtrsim 8$) has about a factor of 2 increase, and it appears that the slope of the spectra (at $k_\perp\rho_s \gtrsim 7$ for t=364 ms and at $k_\perp\rho_s \gtrsim 8$ for t=398 ms) is preserved. Larger decreases, about 60-80%, in spectral power at $k_\perp\rho_s \lesssim 10$ occur while $\omega_{E\times B,WM}/\gamma_{max}$ approaches 0.4 at t=448 ms and 0.7 at t=482 ms. We note that from t=398 to 448 ms the k spectra seem to preserve the shape and power at $k_\perp\rho_s \gtrsim 10$, but at t=482 ms the spectral power at $k_\perp\rho_s \gtrsim 10$ also starts to drop. This overall decrease in spectral power with the large $\omega_{E\times B,WM}/\gamma_{max}$ (~0.7) at t=482 ms is consistent with being close to the quenching threshold $\omega_{E\times B,WM} \approx (1.1 - 1.2)\gamma_{max}$ calculated using the quenching rule in [4.55] with A≈1.9-2.1 and $\kappa \approx 2$. Since the maximum ETG growth rate in the high-k measurement region, $\gamma_{max} \sim 10 - 20C_s/a$ (C_s is the sound speed and a is the plasma minor radius), is much larger than the experimental ExB shearing rate [$(0.1 - 0.4)C_s/a$], ETG turbulence is unlikely to be affected by the experimental amount of ExB shear. However, as we have shown in Fig. 4.17 (b), electron-scale turbulence indeed decreases as ExB shear is increased, and this motivate us to speculate that some of the observed electron-scale turbulence is nonlinearly driven by the ion-scale turbulence and its power decreases as the ion-scale

turbulence is progressively suppressed by the ExB shear. However, in order to fully investigate this multi-scale interaction, multi-scale gyrokinetic simulations are required and are planned and will be carried out in future work.
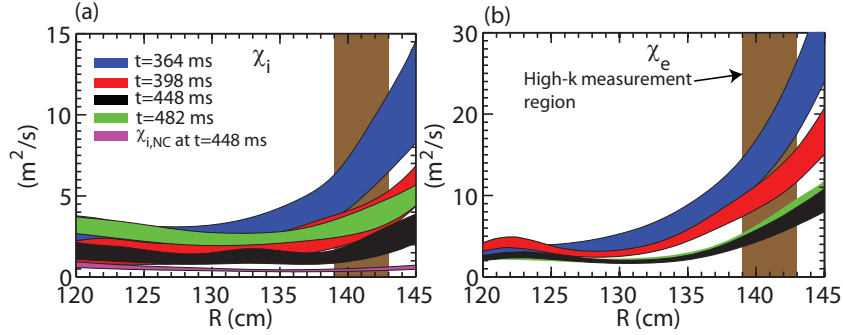

Figure 4.18 The radial profiles of Ion (a) and electron (b) thermal diffusivity at t=364 ms (blue), 398 ms (red), 448 ms (black), 482 ms (green) . The ion neo-classical thermal diffusivity, $\chi_{i,NC}$, (magenta) is also shown in (a). The vertical width of the colored bands denotes the experimental uncertainty mainly due to the uncertainty in ohmic heating and measured kinetic profiles (applicable to χ_i and χ_e). The rectangular shaded region denotes the high-k measurement region.

Having shown the variation in electron-scale turbulence responding to the equilibrium change in the high-k measurement region, here we present the accompany changes in plasma thermal transport. The transport analysis was carried out with a time dependent tokamak transport and data analysis code (TRANSP [4.65]) with measurements from MPTS, CHERS and equilibria from LRDFIT reconstruction. To show how individual transport channel changes, the ion and electron thermal diffusivity profiles at the times of interest used in Fig. 4.17 are plotted in Fig. 18. (We note that the uncertainty in $Â_i$ and $Â_e$ in Fig. 4.18 is mainly due to uncertainties in ohmic heating and measured kinetic profiles). We can immediately see that the largest decrease in both χ_i and χ_e occurs at $R \gtrsim 130\ cm$ ($r/a \gtrsim 0.5$), which coincides well with where the ExB shear varies most in the experiment. Figure 4.18 also shows that from t=364 to 398 ms, χ_i decreases by about 50% and χ_e decreases by about 35% in the high-k measurement region, and a decrease in χ_i and χ_e by about 50% occurs from t=398 to 448 ms, which correlates well with the changes in $\omega_{E\times B,WM}/\gamma_{max}$ shown in Fig. 4.17(a), i.e. about 40% increase from t=364 to 398 ms and about 50% from t=398 to 448 ms. χ_i is always anomalous since at its smallest at t=448 ms, it only approaches to a factor of about 2-3 of the ion neo-classical thermal diffusivity, $\chi_{i,NC}$, which is consistent with the ion-scale turbulence not being completely quenched. We also point out that χ_i becomes larger and χ_e remains essentially the same from t=448 to 482 ms, even though $\omega_{E\times B}/\gamma_{max}$ is almost doubled. As we have pointed out (see Fig. 4.15), an n=1 MHD mode starts to grow at about t=450 ms and saturates at t=470 ms. Thus it is likely that this MHD mode could enhance both ion and electron thermal transport at t=482 ms in addition to microturbulence. However, our analysis shown here concentrates on the time period free of MHD activity.

Non-linear local GYRO runs were performed to determine the transport expected from low-k modes in the outer region of the plasma. The results are shown in Fig. 4.19 for electrons (left panel) and ions (right panel). ExB shear effects were included in the non-linear calculations. The non-linear GYRO transport estimates are shown as a function of r/a in the outer region by the blue squares, while the experimentally inferred transport level is indicated by the colored horizontal bands. What is clearly seen is that no single conclusion can be drawn concerning the

inferred and calculated transport levels. At lower radii (r/a~0.6), the prediction underestimates the transport in both species by up to an order of magnitude. A bit farther out (r/a~0.7), the
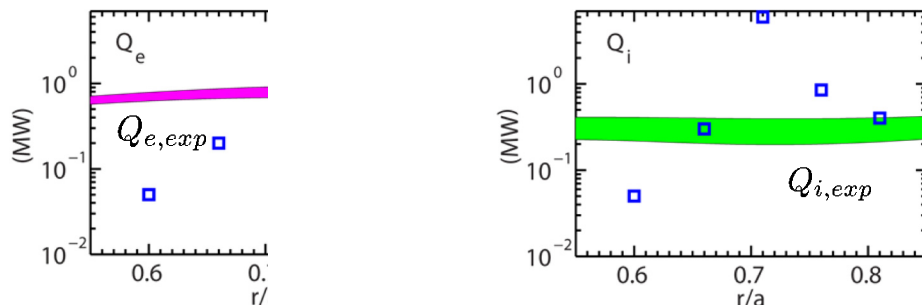

Fig. 4.19 Transport levels for electrons (left panel) and ions (right panel). Blue squares represent the predicted levels from local, non-linear GYRO runs, while the colored bands represent the experimentally inferred values.

predicted transport is in excess of the experimentally inferred value, also by up to an order of magnitude, especially for the ions. However, at other radii, the predicted and inferred transport agrees to within a factor of several. This suggests that the low-k modes can indeed account for the experimentally inferred transport levels in a significant portion of the outer region, and in these cases there is no "missing transport". Future work on this will include comparing predicted turbulence levels.

BES measurements from the discharge discussed above are shown in Fig. 4.20. Plotted are the time-frequency spectrograms and power spectra at selected times for three radial locations, R=129, 136 and 142 cm respectively. The data at the outermost radial location (far right panel in Fig. 4.20) overlaps with the measurement location of the high-k scattering diagnostic discussed above. At this location, there appears to be a decrease in turbulence level from earlier to later times, consistent with the high-k observations and inferences about the importance of the low-k turbulence in controlling transport. The increase in signal at 449 ms, however, is due to the onset of an MHD mode, as pointed out above. Future work will include comparing these spectra to the computed non-linear low-k spectra as filtered through the BES synthetic diagnostic.
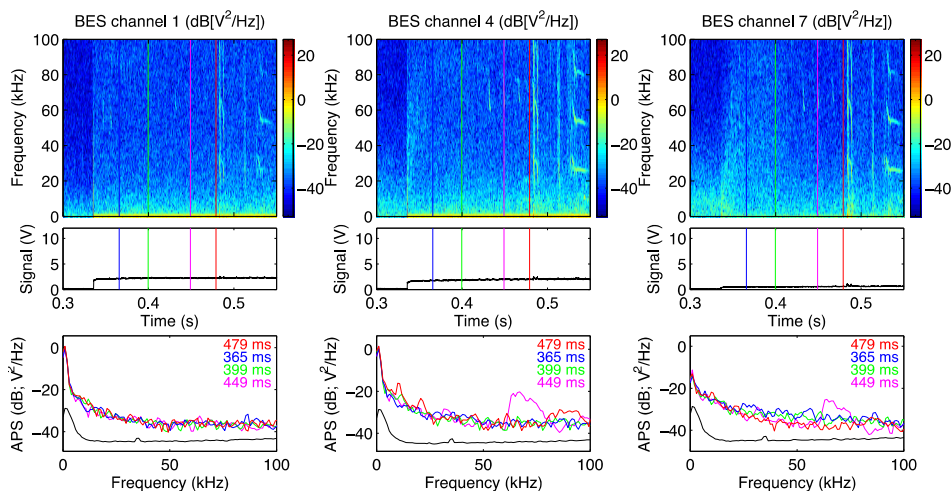

Fig. 4.20 BES spectra at R=129, 136 and 142 cm

4.C.2. Particle Transport

A series of shots was analyzed to assess the thermal deuterium particle transport in the core of the plasma. The study was confined to the core since that is where the particle source, dominated by beam fueling, is known best. The particle source beyond r/a~0.6 is dominated by gas fueling, and the precise source rates, including recycling, in this region are not well known. The discharges chosen have I_p=0.9 MA, B_T=0.55 T, line-averaged density of $\sim$4x10^{19} m^{-3}, and injected heating powers of 2 MW. The range of effective particle fluxes, and predicted levels of neoclassical particle transport for the thermal deuterium ions is shown in Fig. 4.21. The experimental range is indicated by the brown shaded region, which has been plotted only out to r/a=0.8 for the reasons given above. The range of predicted neoclassical fluxes is given by the blue shaded region. This comparison indicates that the particle flux ranges are comparable to what would be expected from neoclassical transport within r/a~0.6. A greater difference between the two is seen for larger radii, but the experimental determination of particle transport is very uncertain due to not knowing the source of neutrals from gas puffing. Ion thermal diffusivities are approximately a factor of several greater than neoclassical, as is seen in Fig. 4.18.
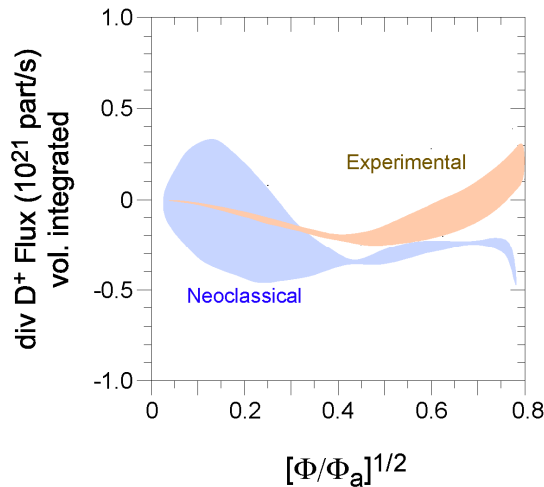

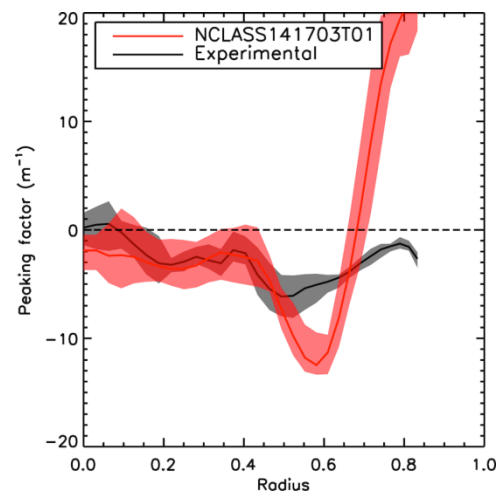Fig. 4.21 Inferred and neoclassical deuterium particle fluxes for L-mode scan

Fig. 4.22 Experimentally inferred (black) and neoclassical peaking factors for the carbon density profile in a representative L-mode discharge.

The carbon density profile evolution was calculated in the same manner as described in the previous section for L-mode discharges from this study. A representative result is shown in Fig. 4.22, where the measured carbon density profile peaking, as reflected by the pinch number v/D, is compared to that as determined from the NCLASS neoclassical calculation out to r/a=0.6. Uncertainties in the ion temperature and impurity density profiles prevented analysis beyond this radius. The measured v/D agrees with the neoclassical result out to r/a~0.5, but then neoclassical theory predicts a greater peaking (inward pinch) farther out. This is generally consistent with the deuterium particle transport result shown in Fig. 4.21, and is consistent with the trend, if not magnitude, of the ion energy transport, which becomes more and more anomalous with increasing radius.

To summarize this section briefly, the energy transport in representative L-mode discharges is anomalous for both ions and electrons, with the ion energy transport becoming more anomalous

as the plasma radius increases. The transport levels, however, decrease with increasing rotation (ExB) shear, and this is accompanied by a reduction in the mid-k range levels of microturbulence. It is believed that this mid-k range of turbulence is coupled to that at lower k. Non-linear gyrokinetic calculations indicate that most of the transport in the outer region of the plasma, for both electrons and ions, can be accounted for by the transport induced by the low-k (ITG-like) turbulence; on average, there is no shortfall of transport. Only in selected radial locations is the transport underestimated by the non-linear predictions. Particle transport of both the main plasma and impurity species again appears to be somewhat decoupled from the energy transport in that the particle transport appears to be consistent with neoclassical estimates in the core (r/a<0.5) of the plasma. There is more of an anomalous behavior farther out.

4.D. Particle transport in neon puff experiments

4.D.1. Edge Impurity Transport Measurements with a Multi- Energy SXR Diagnostic

Perturbative impurity transport measurements were performed in the NSTX plasma edge using short neon gas puffs and a multi-energy soft x-ray (ME-SXR) diagnostic. Sharp temperature gradients in the edge pedestal region of tokamaks and STs necessitate diagnostics with high spatial resolution, as well as create large gradients in ionization state distributions, which limits the usefulness of diagnostics that rely on line emission from a single charge state. A practical solution to this problem is to use photodiode-based diagnostics that measure broadband emission. On NSTX, a new diode-based diagnostic, utilizing multiple filters to help distinguish low charge state emission from higher charge state emission, has been used to measure impurity transport in the ST plasma edge for the first time. Emission from low charge states, measured with thinner filters, provides the source terms for transport analyses of higher charge states.
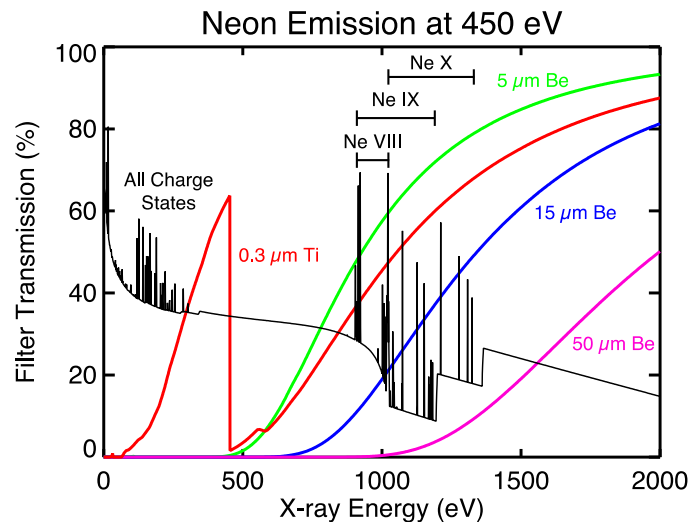

Figure 4.23 The x-ray transmission of the ME-SXR foils over-plotted on the spectrum emitted by neon in a 450 eV plasma (on a log scale).

For the NSTX plasma edge, an ME-SXR system of five 20-channel silicon photodiode arrays, each with a view of essentially the same plasma volume, was constructed and implemented [4.66]. Four arrays have different foil filters (currently 0.3 μm Ti and 5, 15, and 50 μm Be) to provide 4-color spectral resolution, and the fifth array, with no filter, is used for bolometry. The filters discriminate line emission from groups of impurity ionization states as seen in Figure 4.23. Each array has a mid-plane tangential view of the plasma edge with radial coverage from $r/a \sim$ 0.6 to the scrape-off layer (SOL), with a radial resolution of 1 cm. Variable-gain preamplifiers produce a signal with high time resolution, ranging from about 10 kHz for high gain to greater than 100 kHz for low gain. Second-stage amplifiers are used to further boost the signal for digitization. In conjunction with other diagnostics, the ME-SXR arrays can provide fast T_e and impurity density measurements for transport calculations.
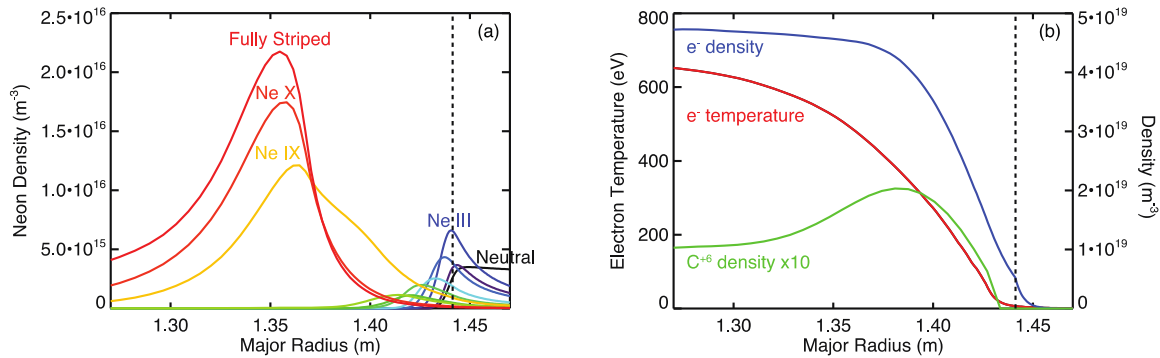

Figure 4.24 (a) Distribution of neon ionization states 20 ms after injection at the plasma edge from the I_p = 1.1 MA, B_T = 0.55 T discharge described below. (b) Electron temperature and density, measured with Thomson scattering, and C^{+6} density, measured CHERS, from this discharge at this time.

To model the particle transport of an injected impurity, we use the STRAHL 1D impurity ion radial transport code [4.67]. For a given impurity, the density evolution of each ionization state is described by a transport equation with a flux-surface averaged diffusion coefficient $D(r, t)$ and convective velocity $v(r, t)$ provided by the user. The particle source/sink term for each ionization state depends on n_e, T_e, and the density of neighboring states through the rate coefficients for ionization and the recombination coefficients for radiative and dielectronic recombination. Neutral deuterium density is not diagnosed in NSTX and is assumed to be negligible inside the separatrix, thus recombination coefficients due to charge exchange are not included in the model. All rate coefficients, along with x-ray emissivity coefficients, are obtained from the ADAS atomic database [4.68]. The plasma parameters n_e and T_e are measured with Thomson scattering. Along with D and v, the third free parameter in this transport model is the source of neutral impurity atoms, both directly from the impurity injection and from divertor and vacuum vessel wall recycling. A simple synthetic diagnostic uses the densities of each charge state of an impurity, calculated by STRAHL, to determine the filtered x-ray intensities that would be measured by the ME-SXR system. A typical neon charge state distribution found with STRAHL is shown in Figure 4.24(a), and the corresponding electron temperature, electron density, and C^{+6} density (the predominant intrinsic impurity in NSTX discharges) are plotted in Figure 4.24(b). ADAS routines are used to calculate the free-free and free-bound continuum emission and the photon emissivity coefficients for line emission from electron impact excitation and from radiative and dielectronic recombination. This total emission is then integrated along the line of sight of each detector and normalized by the transmission of the filter, the detector response, and detector etendue.

To solve for the transport coefficient profiles, this model is fit to the measured data by applying a chi square minimization, with the radial D and v profiles and the neutral source term acting as the free parameters. Note that on the time scale of the gas puff perturbation (~20 ms), the D and v profiles are assumed to be constant in time, thus experimental plasma conditions are chosen to avoid transients such as ELMs. Background emission from intrinsic impurities is found to be small and slowly varying on these timescales, thus for the purposes of this analysis, the emission at the start time of the gas puff is subtracted from the measurement and the remaining signal is assumed to be solely due to neon emission. STRAHL assumes a static magnetic equilibrium while experimentally, the magnetic flux surfaces, including the separatrix, shift radially in time. To account for this, STRAHL's input parameters are mapped to a normalized poloidal flux coordinate ρ_{pol} using the MHD equilibrium code EFIT [4.69], and the resulting x-ray emission is mapped back to major radius. For this work, $D(r)$ and $v(r)$ are defined using a linear spline with knots at $\rho_{pol} = \{0.6, 0.7, 0.8, 0.9, 1.0\}$. Scrape-off layer transport is set equal to the values of the knot at $\rho_{pol} = 1.0$. A core SXR measurement was not available when these measurements were performed, and the edge measurements are insufficient to constrain transport inside $r/a \sim 0.6$. Therefore, based on previous core measurements demonstrating neon transport to be neoclassical in the core of NSTX discharges under nearly identical conditions [4.70, 4.71], $D(r)$ and $v(r)$ are fixed to neoclassical values for $\rho_{pol} \leq 0.5$, with a linear interpolation between $\rho_{pol} = 0.5$ and the knot at $\rho_{pol} = 0.6$. The neoclassical $D(r)$ and $v(r)$ profiles were calculated using the NCLASS code [4.72]. Ion-ion collisions with deuterium and with carbon, the main impurity species, were included in these calculations. Neoclassical neon transport falls in the Pfirsch-Schlüter regime throughout the plasma volume for all cases considered due to its high collisionality, particularly with carbon.

Perturbative impurity transport measurements were performed in NSTX using short 5 ms neon gas puffs at the outboard midplane, injecting about 2.5×10^{17} neon particles. Electrons from the neon puff accounted for only about 0.5% of the total plasma electron density, and Thomson scattering indicates that the perturbation to the bulk plasma was negligible. A toroidal field scan was performed, with q_{95} kept roughly constant by scaling the plasma current accordingly: 0.8 MA at 0.40 T, 0.9 MA at 0.45 T, and 1.1 MA at 0.55 T. Additionally, a few high current (1.1 MA), low field (0.45 T) discharges were obtained. MHD-quiescent, ELM-free discharges were desired to prevent large changes in the measured transport quantities on the time scales of the neon perturbation, a few tens of ms. To this end, the neutral beam power was stepped down from 6 MW to 4 MW after current ramp-up to reduce fast-ion driven modes. Lithium wall conditioning was utilized in an effort to reduce ELM activity. In addition to the ME-SXR array, key diagnostics for the experiment included Thomson scattering for electron temperature and density profile measurements, and magnetic diagnostics, including MSE, needed for equilibrium reconstructions with EFIT. For the initial perturbative impurity transport measurements described here, the ME-SXR diagnostic was not yet fully constructed; only the 5 μm Be array and fractions of the 15 μm and 50 μm Be arrays were available. In place of the ME-SXR edge bolometer array, a separate bolometer, with a coarser spatial resolution covering the entire plasma radius, was employed to constrain the source term.

ME-SXR x-ray brightness measurements from an $I_p = 0.8$ MA, $B_T = 0.40$ T discharge, along with fits from the transport model, are shown in Figure 4.25. The impurity transport profiles resulting from this fit, and from a fit of an $I_p = 1.1$ MA and $B_T = 0.55$ T discharge, are shown in Figure 4.26. The error bars represent the uncertainty in the transport profiles due to uncertainty in the ME-SXR and Thomson measurements and in the neoclassical values used to constrain core transport. For comparison, the results from the NCLASS neoclassical transport calculations are shown with shaded regions on the plots, covering the variation in the calculations during the time frame of the measurement. The results from the measurements roughly match neoclassical calculations, in agreement with previous results from the core [4.70, 4.71]. The diffusion coefficients obtained from measurements are within a factor of 2 of neoclassical transport across most of the plasma radius. Deviations from neoclassical diffusion in the edge region, particularly in the far edge of the low-field discharge, are likely due to edge turbulence and are the topic of ongoing studies. The convection profiles also roughly agree with neoclassical values, though NCLASS does not provide reliable convective velocities outside of $r/a \sim 0.9$. For the two cases shown, the neoclassical convective velocity remains outward far into the core, which is consistent with the hollow neon profile found in the STRAHL simulations at later times.
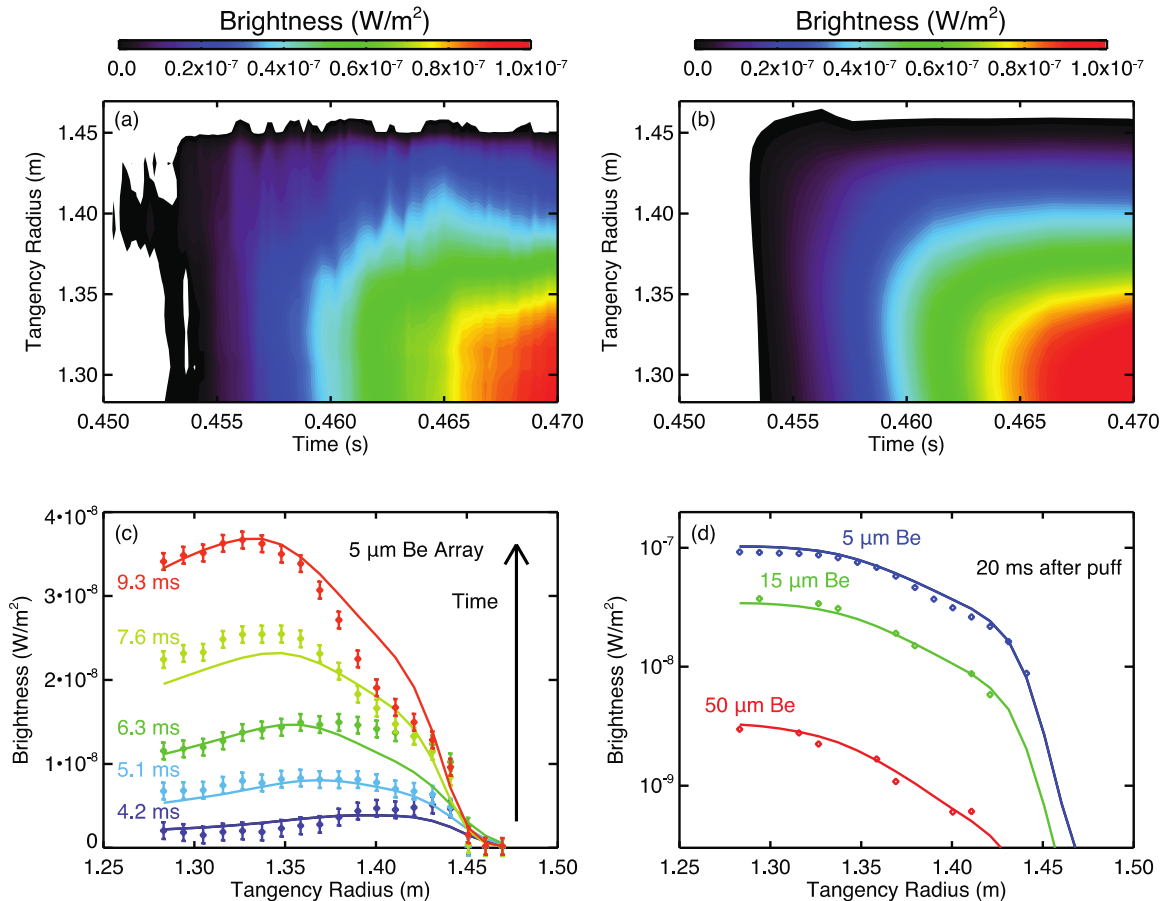

Figure 4.25 (a) Contours of time-evolving x-ray brightness profiles from the $I_p = 0.8$ MA, $B_T = 0.40$ T discharge, measured with the 5 μm Be array. (b) Modeled brightness that best fits the data in (a). (c) Five time slices from (a-b), showing the evolution of the brightness profile shortly after the gas puff. (d) A time slice of the brightness profiles from the 5 μm Be array compared to the 15 μm and 50 μm Be arrays. The points represent measurements and the solid lines represent the fits from the model.

85

Previous results from core measurements have shown that neon convection near mid-radius can be either inward or outward, depending on the ion temperature and density profiles, and that neon profiles can thus be either peaked or hollow [4.70, 4.71]. In conclusion, inside the pedestal region and under the conditions of these quiescent discharges, plasma turbulence is not sufficient to alter transport from neoclassical levels.

4.D.2 Carbon transport

In much the same way as in the previous two main sections, the carbon transport was studied using hybrid and fully predictive MIST simulations as a complement to the STRAHL analysis of the SXR signals discussed in Section 4.a. Without going through all the details of the input data (the data showed many of the same characteristics, e.g., collisionality, etc., as in the datasets discussed earlier), the results are given in Figs. 4.26 and 4.27 for the hybrid MIST and fully predictive MIST calculations respectively. As can be seen in the hybrid prediction in Fig. 4.26. The agreement appears to be quite good at t=0.22 and 0.34 s (the SXR analysis was performed at 0.32 s), but later on, at 0.4 s, the MIST simulation would predict broader peaking and inboard of the observed location. It must be noted that the disagreement here (and in the previous sections) could be due to several effects. First, the implementation of MIST is not flexible in the variation of the adjustable parameters, and the diffusivity is assumed to be constant throughout the discharge. Further, a singly ionized point carbon source is assumed at the separatrix location. The source is increased from t=0 until the H-mode transition, and then it is assumed to be constant throughout the remainder of the discharge. The actual source rate, however, is unknown. This uncertainty can affect the profile evolution in or near the source region, and consequently the required transport coefficients can also be affected.

The results from the fully predictive MIST simulation (assuming neoclassical diffusion and convection) is shown in Fig. 4.28. Here, the neoclassical assumption is good for the earliest time point, at 0.22 s, both for the peaking factor and the location of the edge peaking. At later times, however, the location of the carbon density peaking predicted using the NCLASS D and v is more inboard of that observed experimentally by as much as 5 cm.
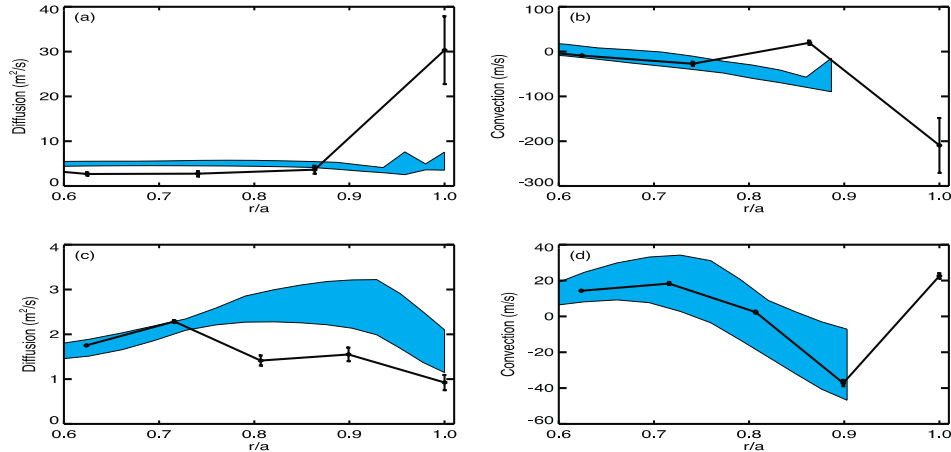

Figure 4.26 (a) The resulting diffusion profile and (b) convection profile from the $I_p = 0.8$ MA, $B_T = 0.40$ T discharge. The shaded region represents the results from NCLASS neoclassical transport calculations. (c) Diffusion profile and (c) convection profile for the $I_p = 1.1$ MA, $B_T = 0.55$ T case. The radial knots are defined for fixed values of ρ_{pol} and thus shift radially between the two cases with different q profiles.
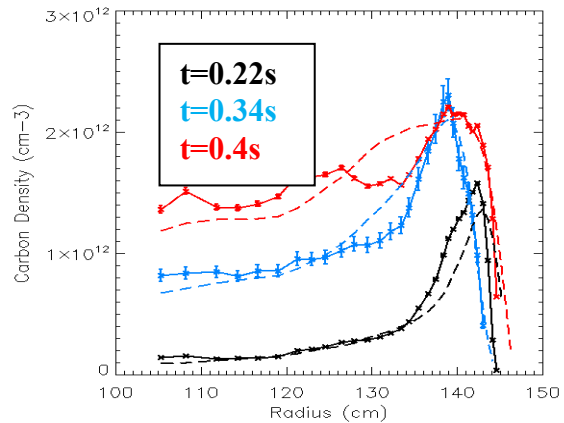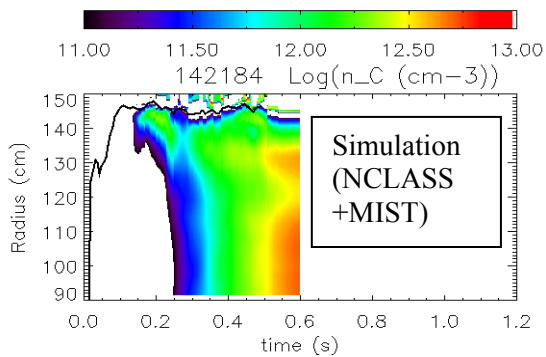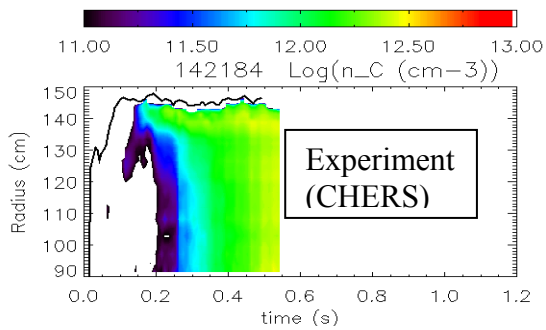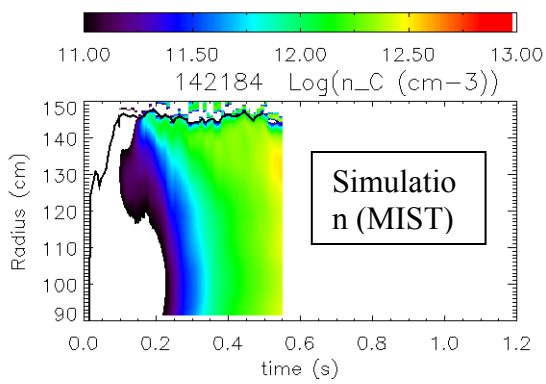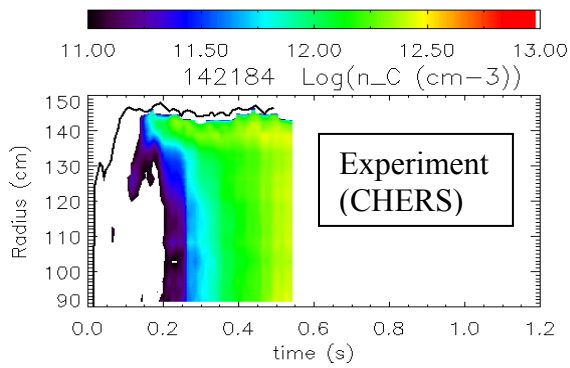
Fig. 4.27 (Left column) Evolution of the carbon density profile vs time and radius for the experimental measurement (top panel) and Hybrid MIST calculation (bottom panel) The direct comparisons between the respective MIST calculations (dashed lines) and experimental profiles (solid curves) are shown at increasing times in the Right column.
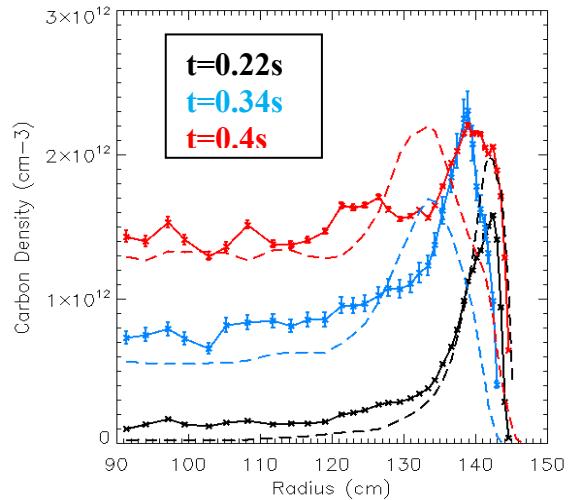

Fig. 4.28 (Left column) Evolution of the carbon density profile vs time and radius for the experimental measurement (top panel) and fully predictive MIST calculation (bottom panel) The direct comparisons between the respective MIST calculations (dashed lines) and experimental profiles (solid curves) are shown at increasing times in the Right column.

87

4.D.3   Energy transport, turbulence measurements and gyrokinetic simulation results

The ion energy transport the discharges used in the neon injection study is shown in Fig. 4.29 for a representative discharge. Plotted is the ratio of the inferred to the neoclassical ion thermal diffusivity as a function of minor radius. In the core of the discharge, r/a≤0.5, the ions appear to be somewhat anomalous, with values of the χ_i ratio from three to seven. Outside that radius, the ratio is near one, indicating the ion energy transport is consistent with neoclassical there. The neoclassical behavior of the ions outside of r/a=0.5 is consistent with the inferences from the neon transport analysis (Section 4.a). The carbon transport results (Section 4.b) possibly indicates some anomalous behavior. The electron transport in these discharges is high, consistent with levels seen in other H-mode discharges.
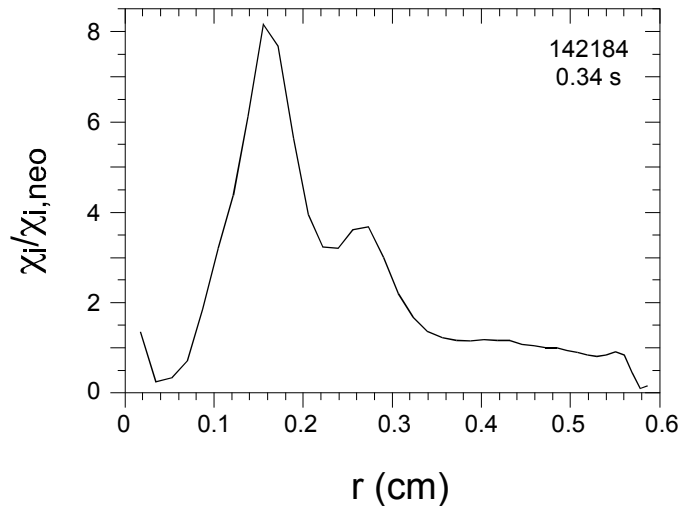

Fig. 4.29 Ratio of inferred to neoclassical ion thermal diffusivity as a function of minor radius for a representative discharge in the neon injection study.

BES measurements from one of the discharges used in this study is shown in Fig. 4.30, and they are typical of the measurements in the other discharges. The spectra from three different radial positions are similar in their broadness and lack of detail. Correlation analysis in the frequency range from 8 to 50 kHz indicates poloidal correlation lengths of approximately 8 cm, confirming the low-k nature of these modes. Analysis of this data will continue with comparisons to turbulence levels calculated from gyrokinetic codes and filtered through synthetic diagnostics. Gyrokinetic calculations are underway for these plasmas.

To summarize this section briefly, measurements of impurity profiles and analysis of their transport in the outer half of the plasma suggest that the impurity transport is, to zeroth order, neoclassical. There are some departures from strict neoclassical transport, especially in the position of the carbon peaking towards the plasma edge, and this may reflect the effects of residual low-k turbulence in that region. The ion thermal transport in the mid-radius range of the plasma is also found to be near neoclassical. Gyrokinetic calculations, to attempt to understand the role of low-k turbulence and where it might be important, are underway.
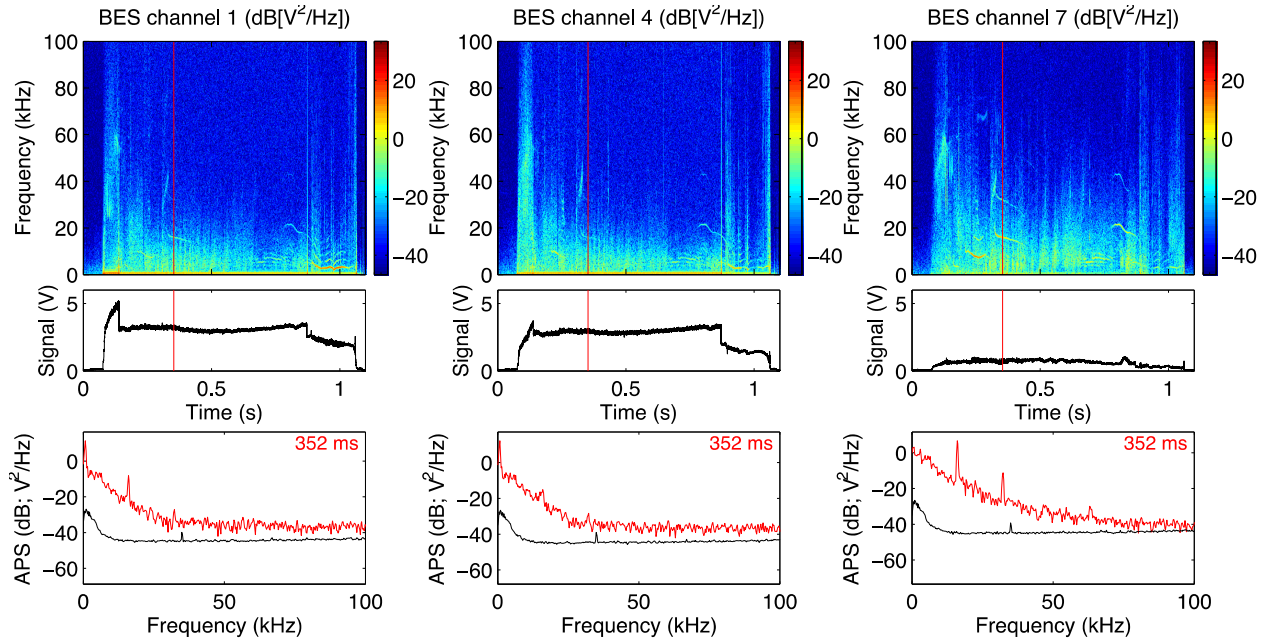
Fig. 4.30 BES spectra for R=129, 136 and 142 cm.

4.E. Summary

NSTX studies were carried out in three main areas to couple to those studies on other devices. H-mode collisionality scan studies pointed to a strong increase of confinement time with decreasing collisionality, reflecting a strong decrease in electron transport in the outer region of the plasma with decreasing collisionality. This is coupled with an increase in the ion transport, from neoclassical to anomalous levels, as collisionality decreases. While high- and low-k electron modes are believed to be suppressed (through linear gyrokinetic calculations), hybrid modes, which may drive ion transport, are more extended and stronger at the lower collisionalities. At the higher collisionality, the electron transport appears to be driven primarily by microtearing modes, with possible contributions from ETG modes. At lower collisionalities, the source of the anomalous electron transport is most likely related to the hybrid TEM/KBM modes that result from the gyrokinetic calculations. The particle transport, as inferred from carbon and lithium profile changes, appears to be neoclassical and insensitive to changes in collisionality.

In L-modes, both the ions and electrons are anomalous, although the transport and high-k turbulence levels are highly sensitive to ExB shear (decreasing with increasing rotation shear). Non-linear gyrokinetic calculations indicate that the low-k modes (through the TEM k-range) appear to be driving the high-k turbulence, and they are primarily responsible for both the ion and electron transport. On average, there is NO transport shortfall computed for the outer region of NSTX L-mode plasmas. The impurities, once again however, appear to be neoclassical to zero[th] order. Lastly, dedicated impurity transport experiments using both neon injection and the measurement of the carbon and lithium evolution, indicate that the impurities are near neoclassical levels of transport.

The results of the various NSTX studies point to an apparent decoupling between the particle and energy transport. Impurities appear to be mostly neoclassical, even in situations where both the ion and electron transport is anomalous. However, the agreement with neoclassical transport is not perfect; predicted and measured locations of profile peaking near the edge appear to be somewhat different, and more peaking is predicted in the core than is observed. This may indicate some role by lower-k modes in driving the impurity transport. Non-linear gyrokinetic calculations to explore this possible role are underway.

References

[4.1]   B. Coppi and G. Rewoldt, *Advances in Plasma Physics* vol 6 ed A Simon and W B. Thompson (New York: Wiley) 421 (1976).

[4.2]   W. Horton, Rev. Mod. Phys. 71, 735 (1999).

[4.3]   J.W. Connor and H.R. Wilson, Plasma Phys. Control. Fusion 36, 719 (1994).

[4.4]   B. Coppi, M.N. Rosenbluth, and R.Z. Dagdeev, Phys. Fluids 10, 582 (1967).

[4.5]   Y.C. Lee, J.Q. Dong, P.N. Guzdar, et al, Phys. Fluids 30, 1331 (1987).

[4.6]   W. Horton, B.G. Wong, and W. M. Tang, Phys. Fluids 31, 2971 (1988).

[4.7]   R.E. Waltz, G.M. Staebler, W. Dorland, et al., Phys. Plasmas 4, 2482 (1997).

[4.8]   A.M. Dimits, G. Bateman, M.A. Beer, et al., Phys. Plasmas 7, 969 (2000).

[4.9]   X. Garbet, P. Mantica, C. Angioni, et al., Plasma Phys. Control. Fusion 46, B557 (2004).

[4.10] J. F. Drake, N. T. Gladd, C. S. Liu, et al., Phys. Rev. Lett. 44, 994 (1980).

[4.11] R.J. Fonck, G. Cosby, R.D. Durst, et al., Phys. Rev. Lett. 70, 3736 (1993).

[4.12] E. Mazzucato, S.H. Batha, M. Beer, et al., Phys. Rev. Lett. 77, 3145 (1996).

[4.13] G.R. McKee, R.J. Fonck, D.K. Gupta, et al., Plasma Fusion Res. 2, S1025 (2007).

[4.14] A.E. White, L. Schmitz, G.R. McKee, et al., Phys. Plasmas 15, 056116 (2008).

[4.15] T.L. Rhodes, W.A. Peebles, M.A. Van Zeeland, et al., Phys. Plasmas 14, 056117 (2007).

[4.16] A.D. Gurchenko, E.Z. Gusakov, A.B. Altukhov, et al., Nucl. Fusion 47, 245 (2007).

[4.17] A. Casati, T. Gerbaud, P. Hennequin, et al., Phys. Rev. Lett. 102, 165005 (2009).

[4.18] C. Holland, J. Candy, R.E. Waltz, et al., Journal of Physics: Conference Series 125, 012043 (2008).

[4.19] D.R. Ernst, P.T. Bonoli, P.J. Catto, et al., Phys. Plasmas 11, 2637 (2004).

[4.20] E.J. Doyle, W.A. Houlberg, Y. Kamada et al., Nucl. Fusion 47, S18 (2007).

[4.21] S. M. Kaye, R.E. Bell, D. Gates, et al., Phys. Rev. Lett. 98, 175002 (2007).

[4.22] F. Jenko and W. Dorland, Phys. Rev. Lett. 89, 225001 (2002).

[4.23] E. Mazzucato, Phys. Plasmas 10, 753 (2003).

[4.24] E. Mazzucato, Plasma Phys. Controlled Fusion 48, 1749 (2006).

[4.25] D.R. Smith, E. Mazzucato, W. Lee, et al., Jr., Rev.Sci. Instrum. 79, 123501 (2008).

[4.26] E. Mazzucato, D.R. Smith, R.E. Bell, et al., Phys. Rev.Lett. 101, 075001 (2008).

[4.27] E. Mazzucato, R.E. Bell, S. Ethier, et al., Nucl. Fusion 49, 055001 (2009).

[4.28] H. Yuh, F.M. Levinton, R. E. Bell, et al., Phys. Plasmas 16, 056120 (2009).

[4.29] H. Y. Yuh, S. M. Kaye, F. M. Levinton, et al., Phys. Rev. Lett. 106, 055003 (2011).

[4.30] D.R. Smith, S.M. Kaye, W. Lee, et al., Phys. Rev. Lett. 102, 225005 (2009).

[4.31] Y. Ren, S.M. Kaye, E. Mazzucato, et al., Phys. Rev. Lett. 106, 165005 (2011).

[4.32] S.M. Kaye, F.M. Levinton, D. Stutman, et al., Nucl. Fusion 47, 499 (2007).

[4.33] K. L. Wong, S. Kaye, D. R. Mikkelsen, et al., Phys. Plasmas, 15, 056108 (2008).

[4.34] W. Guttenfelder, et al., Phys. Rev. Lett. 106, 155004 (2011).
[4.35] W. Guttenfelder, et al., Phys. Plasmas 19, 022506 (2012).
[4.36] W. Guttenfelder, et al., Phys. Plasmas 19, 056119 (2012).
[4.37] D. Stutman, L. Delgado-Aparicio, N. Gorelenkov, et al., Phys. Rev. Lett., 102, 115002 (2009).
[4.38] D.R. Smith, R.J. Fonck, G.R. McKee et al., Rev. Sci. Instruments 83, 10D502 (2012).
[4.39] J. Candy and R.M. Waltz, J. Comput. Phys. 186, 545 (2003).
[4.40] M. Valovic, et al., Nucl. Fusion 49, 075016 (2009).
[4.41] M. Valovic, et al., Nucl. Fusion 51, 075045 (2011).
[4.42] H. W. Kugel, , et al., Journ. Nucl. Materials 390, 1000 (2009).
[4.43] M.G. Bell, et al., Plasma Phys. Controlled Fusion 51, 124054 (2009).
[4.44] S. Ding, et al., Plasma Phys. Controlled Fusion 52, 015001 (2010).
[4.45] S.P. Gerhardt, et al., Nucl. Fusion 51, 073031 (2011).
[4.46] S.M. Kaye, S.P. Gerhardt, W. Guttenfelder, et al., IAEA FEC Meeting, Paper EX7-1 (2012).
[4.47] F. Jenko, et al., Phys. Plasmas 8, 4096 (2001)
[4.48] R. Hulse, Nucl. Technol. Fusion 3 (259), (1983).
[4.49] W.A. Houlberg et al., Phys. Plasmas 4 (9), (1997).
[4.50] E.A. Belli et al., Plasma Phys. Control. Fusion, 50, 095010, (2008).
[4.51] R.E. Bell, et al., Rev. Sci. Instrum., 81, 10D724, (2010).
[4.52] M. Podesta, et al., Nucl. Fusion, 52, 033008, (2012).
[4.53] K.H. Burrell, et al., Phys. Plasmas 4, 1499 (1997).
[4.54] T. S. Hahm and K. H. Burrell, Phys. Plasmas 2, 1648 (1995).
[4.55] J. E. Kinsey, R. E. Waltz, and J. Candy, Phys. Plasmas 14, 102306 (2007).
[4.56] R.E. Waltz and R.L. Miller, Phys. Plasmas 6, 4265 (1999).
[4.57] C.P. Ritz et al., Phys. Rev. Lett. 65, 2543 (1990).
[4.58] A.R. Field et al., Proc. 20th IAEA FEC Conference, Vilamoura, Portugal EX/P2-11 (2004).
[4.59] M. Ono et al., Nucl. Fusion 40, (2000) 557.
[4.60] R.E. Bell, Rev. Sci. Instruments 77, 10E902 (2006).
[4.61] F.M. Levinton et al., Phys. Plasmas 14, 056119 (2007).
[4.62] B.P. LeBlanc et al., Rev. Sci. Instruments 74, 1659 (2003).
[4.63] J.E. Menard et al., Phys. Rev. Lett. 97, 095002 (2006).
[4.64] M. Kotschenreuther et al., Comp. Phys. Comm. 88, 128 (1995).
[4.65] R.J. Hawryluk, Physics of Plasmas Close to Thermonuclear Conditions (Pergamon, New York, 1981).
[4.66] K. Tritz, D. J. Clayton, D. Stutman, and M. Finkenthal, Rev. Sci. Instrum. 83, 10E109 (2012).
[4.67] K. Behringer, Description of impurity code 'STRAHL', Technical Report JET-IR(87)08, JET Joint Undertaking, Oxfordshire: Abingdon (1987).
[4.68] H. P. Summers, Atomic Data and Analysis Structure, Technical Report JET-IR(94)06, JET Joint Undertaking, Oxfordshire: Abingdon (1994).
[4.69] S. A. Sabbagh, et al., Nucl. Fusion 41, 1601 (2001).
[4.70] L. Delgado-Aparicio, et al., Nucl. Fusion 49, 085028 (2009).
[4.71] L. Delgado-Aparicio, et al., Nucl. Fusion 51, 083047 (2011).
[4.72] W. A. Houlberg, et al., Phys. Plasmas 4, 3230 (1997).